Biomed Tech 2013; 58 (Suppl. 1) © 2013 by Walter de Gruyter · Berlin · Boston. DOI 10.1515/bmt-2013-4154

TRANSÖSOPHAGEALES INTERVENTRIKULÄRES DELAY BEI VORHOFFLIMMERN UND KARDIALER RESYNCHRONISATION

M. Heinke[1], B. Ismer[1], H. Kühnert[2], T. Heinke[3], G. Dannberg[2], H.R. Figulla[2]

[1]University of Applied Sciences Offenburg, Offenburg, Deutschland
[2]Universitätsklinikum Jena, Klinik für Innere Medizin I, Jena, Deutschland
[3]Siemens AG, Healthcare Sector, Rudolstadt, Deutschland

Matthias.Heinke@hs-offenburg.de

Abstract: *Die transösophageale linksventrikuläre Elektrokardiographie ermöglicht die Evaluierung der elektrischen ventrikulären Desynchronisation im Rahmen der kardialen Resynchronisationstherapie der Herzinsuffizienz. Das Ziel der Untersuchung besteht in der präoperativen Abschätzung des transösophagealen interventrikulären Delays bei Vorhofflimmern und kardialer Resynchronisationstherapie.*
Bei Patienten mit Vorhofflimmern, Herzinsuffizienz New York Heart Association Klasse 3,0 ± 0,2 und QRS-Dauer 159,6 ± 23,9 ms wurde das fokusierte transösophageale linksventrikuläre EKG abgeleitet. Die kardiale Resynchronisationstherapie Responder QRS-Dauer korrelierte mit dem transösophagealen interventrikulären Delay bei Vorhofflimmern.

Keywords: *Kardiale Resynchronisationstherapie, Vorhofflimmern, linksventrikuläres EKG, transösophageales EKG, interventrikuläres Delay*

Einleitung

Bei Patienten mit Herzinsuffizienz (HF), Linksschenkelblock und reduzierter linksventrikulärer Ejektionsfraktion sind das Ausmaß der elektrischen ventrikulären Desynchronisation und die Lage der implantierten linksventrikulären Elektrode von entscheidender Bedeutung für den Erfolg der kardialen Resynchronisationstherapie (CRT) mit biventrikulärer Stimulation bei Sinusrhythmus. Die intrakardiale und transösophageale linksventrikuläre Elektrokardiographie ermöglichen eine Abschätzung des elektrischen interventrikulären Delays.
CRT Responder mit 170 ± 31 ms mittlere QRS-Dauer zeigten ein verlängertes transösophageales elektrisches interventrikuläres Delay größer 40 ms und ein mittleres interventrikuläres Delay von 81± 25 ms. Bei CRT Nonresponder mit 174 ± 10 ms mittlere QRS-Dauer betrug das signifikant verkürzte transösophageale interventrikuläre Delay im Mittel 30 ± 11 ms [1]. Die auf den posterioren linken Ventrikel fokusierte transösophageale linksventrikuläre Elektrokardiographie und temporäre transösophageale linksventrikuläre Stimulation können zur Verbesserung der Patientenauswahl vor CRT beitragen [2].
Das Ziel der Untersuchung besteht in der präoperativen Abschätzung des elektrisc hen interventrikulären Delays bei CRT Responder und CRT Nonresponder mit Vorhofflimmern.

Methoden

Bei 17 Patienten mit Vorhofflimmern (Alter 61,2 ± 11,5 Jahre, 16 Männer und 1 Frau), Herzinsuffizienz New York Heart Association Klasse 3,0 ± 0,2 , linksventrikuläre Ejektionsfraktion 24,9 ± 5,6 % und QRS-Dauer 159,6 ± 23,9 ms wurde das interventrikuläre Delay als Intervall zwischen Beginn des QRS-Komplexes im Oberflächen EKG und Beginn des linksventrikulären Potentials im transösophagealen linksventrikulären EKG bestimmt. Das telemetrische intrakardiale interventrikuläre Delay wurde zwischen Beginn des rechtsventrikulären Potentials im rechtsventrikulären EKG und Beginn des linksventrikulären Potentials im linksventrikulären EKG vermessen. Die präoperative linksventrikuläre Elektrokardiographie erfolgte mit Hilfe des Osypka TO Katheters in Höhe der maximalen linksventrikulären Deflektion (Abb. 1). Das intralinksventrikuläre Delay wurde zwischen Beginn und Ende des linksventrikulären Potentials im transösophagealen linksventrikulären EKG bestimmt.

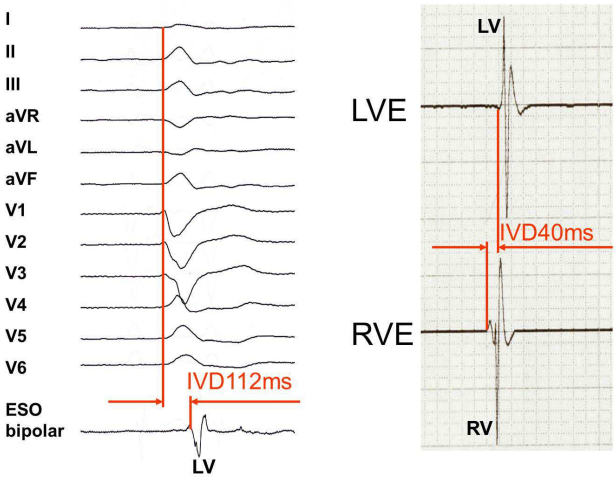

Abbildung 1: Elektrische ventrikuläre Desynchronisation bei Vorhofflimmern und dilatativer Kardiomyopathie. Das transösophageale interventrikuläre Delay (linke Seite) beträgt 112ms und das telemetrische intrakardiale interventrikuläre Delay 40ms (rechte Seite). LV - linksventrikuläres Potential, RV – rechtsventrikulä-

res Potential, I, II, III, aVR, aVl, aVF, V1-V6 - Oberflächen EKG, ESO bipolar – bipolares transösophageales linksventrikuläres EKG, LVE - intrakardiales linksventrikuläres EKG, RVE – intrakardiales rechtsventrikuläres EKG.

Bei 15 Patienten wurde ein CRT-Defibrillator und bei 2 Patienten ein CRT-Herzschrittmacher implantiert. Postoperativ erfolgte die individuelle hämodynamische CRT Optimierung des VV-Delays zwischen rechtsventrikulärer und linksventrikulärer Stimulation mit der Medis Cardiosreen Impedanzkardiographie.

Ergebnisse

Bei 11 CRT Responder mit Vorhofflimmern betrugen das transösophageale interventrikuläre Delay 68,7± 22,9 ms, das transösophageale intralinksventrikuläre Delay 76,5 ± 17,4 ms und die QRS Dauer 161,6 ± 22,2 ms. Die CRT Responder QRS-Dauer korrelierte mit dem transösophagealen interventrikulären Delay (r=0,60, P=0,0499) (Abb. 2).

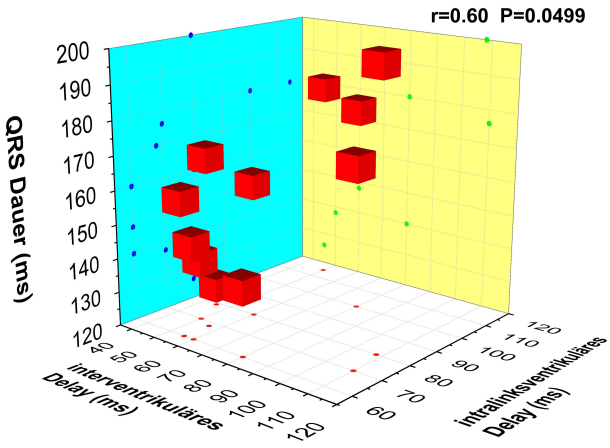

Abbildung 2: Elektrische ventrikuläre Desynchronisation bei kardialen Resynchronisationstherapie Responder mit Vorhofflimmern, r, P – Pearson correlation coefficients

Bei 6 CRT Nonresponder mit Vorhofflimmern betrugen das transösophageale interventrikuläre Delay 50,3± 33,9 ms, das transösophageale intralinksventrikuläre Delay 93,2 ± 31,4 ms und die QRS Dauer 155,8 ± 28,7 ms. Die CRT Nonresponder QRS-Dauer korrelierte nicht mit dem transösophagealen interventrikulären Delay (Abb. 3).
Die CRT Responder verbesserten sich in der New York Heart Association Klasse von 3,1 ± 0,2 auf 2,1 ± 0,3 (P < 0,001) während 16,3 ± 13,7 Monaten CRT mit hämodynamisch VV-Delay optimierter biventrikulärer Stimulation.

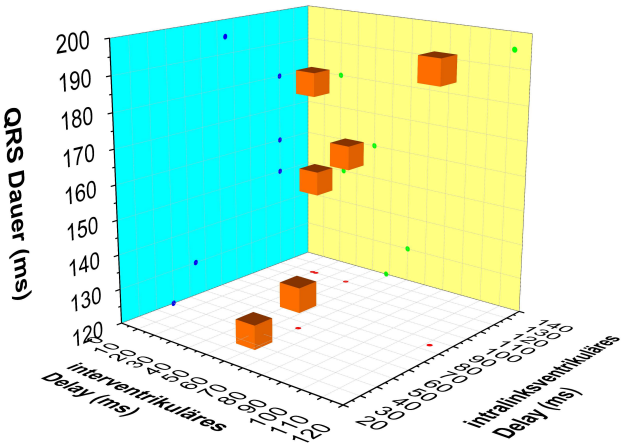

Abbildung 3: Elektrische ventrikuläre Desynchronisation bei kardialen Resynchronisationstherapie Nonresponder mit Vorhofflimmern

Diskussion

Die auf den posterioren linken Ventrikel fokusierte transöophageale linksventrikuläre Elektrokardiographie ermöglicht bei Patienten mit Herzinsuffizienz und Vorhofflimmern die präoperative Messung des elektrischen interventrikulären Delays und intralinksventrikulären Delays.
Das transösophageale interventrikuläre Delay lässt sich möglicherweise intraoperativ als Mindestzielwert zur Positionierung der linksventrikulären Elektrode benutzen und ist ein einfach anwendbarer Parameter zur Abschätzung der elektrischen ventrikulären Desynchronisation bei Vorhofflimmern. Das elektrische interventrikuläre Delay lässt sich möglicherweise zur Vorhersage von CRT Responder und CRT Nonresonder nutzen.

Literatur

[1] Heinke, M., Surber, R. et. al.: Transesophageal left ventricular posterior wall potential in heart failure patients with biventricular pacing, *Biomed Tech,* vol. 52, pp. 173-179, 2007

[2] Heinke, M., Ismer, B. et. al.: Transesophageal left ventricular electrogram-recording and temporary pacing to improve patient selection for cardiac resynchronization, *Med Biol Eng Comput,* vol. 49, pp. 851-858, 2011

Biomed Tech 2013; 58 (Suppl. 1) © 2013 by Walter de Gruyter · Berlin · Boston. DOI 10.1515/bmt-2013-4155

VENTRIKULÄRE DESYNCHRONISATION MIT UND OHNE ISCHÄMISCHE HERZERKRANKUNG BEI RESYNCHRONISATIONSRESPONDERN

M. Heinke[1], B. Ismer[1], G. Dannberg[2], T. Heinke[3], H. Kühnert[2]

[1]University of Applied Sciences Offenburg, Offenburg, Deutschland
[2]Universitätsklinikum Jena, Klinik für Innere Medizin I, Jena, Deutschland
[3]Siemens AG, Healthcare Sector, Rudolstadt, Deutschland

matthias.meinke@hs-offenburg.de

Abstract: *Das Ausmaß der elektrischen ventrikulären Desynchronisation bei reduzierter linksventrikulärer Funktion ist von Bedeutung für den Erfolg der Resynchronisationstherapie der Herzinsuffizienz mit biventrikulärer Stimulation. Das Ziel der Untersuchung besteht in der nichtinvasiven Messung der elektrischen interventrikulären Desynchronisation mit und ohne ischämische Herzerkrankung bei kardialen Resynchronisationstherapie Respondern. Bei Patienten mit 25,3 ± 7,3 % reduzierter linksventrikulärer Ejektionsfraktion und 166,9 ± 38,5 ms QRS-Dauer wurde das transösophageale linksventrikuläre EKG abgeleitet. Die QRS-Dauer korrelierte mit dem interventrikulären und linksventrikulären Delay bei Resynchronisationstherapie Respondern mit nicht-ischämischer Herzerkrankung.*

Keywords: *Biventrikuläre Stimulation, kardiale Resynchronisationstherapie, ischämische Herzerkrankung, linksventrikuläre Desynchronisation, interventrikuläres Delay*

Einleitung

Bei Patienten mit chronischer hochgradiger Herzinsuffizienz und reduzierter linksventrikulärer Ejektionsfraktion kleiner 35 % sind das Ausmaß der elektrischen interventrikulären Desynchronisation, die Lage der implantierten linksventrikulären Stimulationselektrode zum Ort der spätesten linksventrikulären Erregung und die Optimierung des atrioventrikulären Delays bedeutend für den Langzeiterfolg der kardialen Resynchronisationstherapie (CRT) mit biventrikulärer Stimulation [1, 2].
Das Ziel der Untersuchung besteht in der präoperativen nichtinvasiven Bestimmung des transösophagealen elektrischen interventrikulären Delays und linksventrikulären Delays bei CRT Respondern mit ischämischer und nicht-ischämischer Herzerkrankung.

Methoden

Bei 31 Patienten mit ischämischer und nicht-ischämischer Herzerkrankung (Alter 62,5 ± 11,4 Jahre, 27 Männer und 4 Frauen), Herzinsuffizienz New York Heart Association Klasse 3,0 ± 0,2 , linksventrikuläre Ejektionsfraktion 25,3 ± 7,3 %, QRS-Dauer 166,9 ± 38,5 ms und interatrialem Delay 70,7 ± 23,5 ms (n=18) wurden das interventrikuläre Delay als Intervall zwischen Beginn des QRS-Komplexes im Oberflächen EKG und Beginn des linksventrikulären Potentials im transösophagealen linksventrikulären EKG und das linksventrikuläre Delay als Intervall zwischen Beginn und Ende des linksventrikulären Potentials im transösophagealen linksventrikulären EKG bestimmt. Das interatriale Delay wurde als Intervall zwischen Beginn und Ende des linksatrialen Potentials im transösophagealen EKG bestimmt.

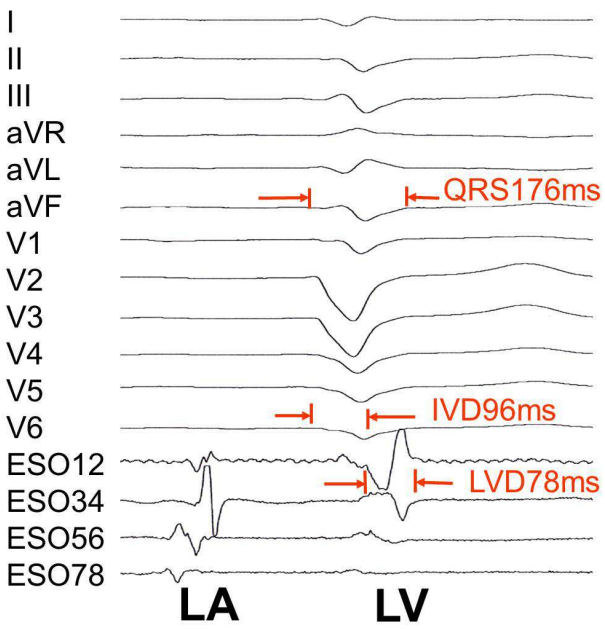

Abbildung 1:Transösophageale elektrische ventrikuläre Desynchronisation mit 96 ms interventrikuläres Delay und 78 ms linksventrikuläres Delay bei Sinusrhythmus, ischämischer Herzerkrankung und Resynchronisationstherapie Responder. IVD – interventrikuläres Delay, LVD – linksventrikuläres Delay, LA – linksatriales Potential, LV – linksventrikuläres Potential, I, II, III, aVR, aVl, aVF, V1-V6 - Oberflächen EKG, ESO12, ESO34 – distales bipolares transösophageales linksventrikuläres EKG, ESO56, ESO78 – proximales bipolares transösophageales linksatriales EKG.

Die bipolare transösophageale Elektrokardiographie erfolgte mit Hilfe des Osypka TO4 Katheters in Höhe der maximalen linksventrikulären Deflektion oder des Osypka TO8 Katheters in Höhe der maximalen linksventrikulären und linksatrialen Deflektion (Abb. 1). Bei 24 Patienten wurde ein Boston CRT-Defibrillator, bei 6 Patienten ein Medtronic CRT-Defibrillator und bei 1 Patient ein St. Jude CRT-Defibrillator implantiert. Postoperativ erfolgte die individuelle hämodynamische CRT Optimierung des atrioventrikulären Delays und des interventrikulären Delays zwischen rechtsventrikulärer und linksventrikulärer Stimulation mit der Medis Cardiosreen Impedanzkardiographie.

Ergebnisse

Bei 19 CRT Responder mit nicht-ischämischer Herzerkrankung betrugen das transösophageale interventrikuläre Delay 78,1± 25,2 ms, das transösophageale linksventrikuläre Delay 77,6 ± 21,7 ms und die QRS-Dauer 175,8 ± 43,5 ms. Die nicht-ischämische Herzerkrankung CRT Responder QRS-Dauer korrelierte mit dem transösophagealen interventrikulären Delay (r=0,75, P<0,001) und transösophagealen linksventrikulären Delay (r=0,51, P=0,02) (Abb. 2).

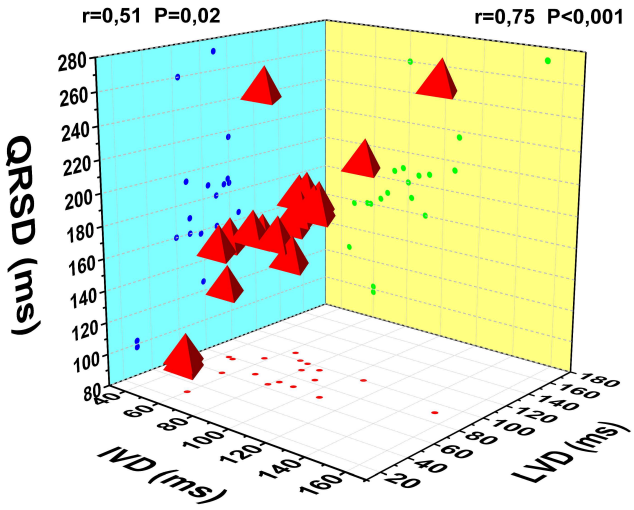

Abbildung 2: Elektrische ventrikuläre Desynchronisation bei kardialen Resynchronisationstherapie Respondern mit nicht-ischämischer Herzerkrankung. IVD – interventrikuläres Delay, LVD – linksventrikuläres Delay, QRSD – QRS-Dauer, r, P – Pearson correlation coefficients

Bei 12 CRT Responder mit ischämischer Herzerkrankung betrugen das transösophageale interventrikuläre Delay 71,8± 18,0 ms, das transösophageale linksventrikuläre Delay 71,3 ± 18,9 ms und die QRS-Dauer 152,8 ± 24,3 ms. Die ischämische Herzerkrankung CRT Responder QRS-Dauer korrelierte mit dem transösophagealen linksventrikulären Delay (r=0,75, P=0,005) (Abb. 3).

Die CRT Responder verbesserten sich in der New York Heart Association Klasse von 3,0 ± 0,2 auf 2,0 ± 0,3 (P < 0,001) während 19,4 ± 17,0 Monaten CRT mit hämodynamisch atrioventrikulär und interventrikulär optimierter biventrikulärer Stimulation.

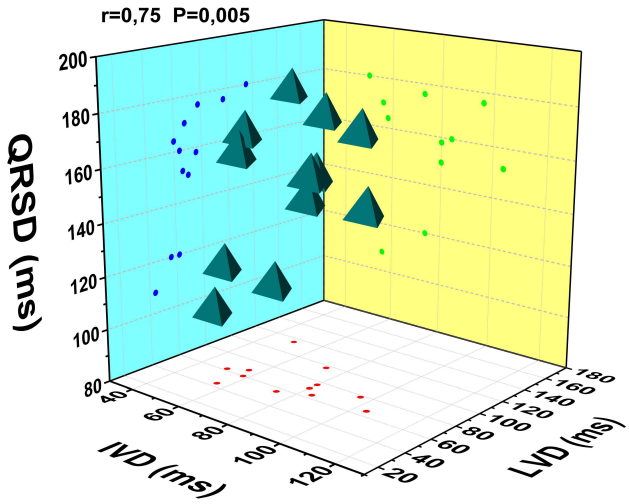

Abbildung 3: Elektrische ventrikuläre Desynchronisation bei kardialen Resynchronisationstherapie Respondern mit ischämischer Herzerkrankung, IVD – interventrikuläres Delay, LVD – linksventrikuläres Delay, QRSD – QRS-Dauer, r, P – Pearson correlation coefficients

Diskussion

Die auf den posterioren linken Vorhof und/oder linken Ventrikel fokusierte transösophageale linksatriale und/oder linksventrikuläre Elektrokardiographie ermöglichen bei Patienten mit Herzinsuffizienz, ischämischer und nicht-ischämischer Herzerkrankung die präoperative Messung des elektrischen interatrialen, interventrikulären und linksventrikulären Delays.
Das transösophageale interventrikuläre und linksventrikuläre Delay sind einfach anwendbarer Parameter zur präoperativen Abschätzung der elektrischen ventrikulären Desynchronisation und lassen sich möglicherweise zur Vorhersage von CRT Responder nutzen.

Literatur

[1] Heinke, M., Surber, R. et. al.: Transesophageal left ventricular pacing in heart failure patients with permanent rigth ventricular pacing, *Europace,* vol. 7, pp. 617-620, 2005

[2] Heinke, M., Ismer, B. et. al.: Transesophageal left ventricular electrogram-recording and temporary pacing to improve patient selection for cardiac resynchronization, *Med Biol Eng Comput,* vol. 49, pp. 851-858, 2011

Biomed Tech 2013; 58 (Suppl. 1) © 2013 by Walter de Gruyter · Berlin · Boston. DOI 10.1515/bmt-2013-4156

ELECTRODE ARRANGEMENTS FOR ECG IMAGING UNDER PRACTICAL CONSTRAINTS OF A CATHETER LAB SETTING

Schulze WHW[1], Schimpf R[2], Papavassiliu T[2], Potyagaylo D[1], Tulumen E[2], Rudic B[2], Liebe V[2], Doesch C[2], Konrad T[2], Veltmann C[2], Borggrefe M[2] and Dössel O[1]

[1]Institute of Biomedical Engineering, Karlsruhe Institute of Technology (KIT), Karlsruhe, Germany
[2]1st Department of Medicine-Cardiology, University Medical Centre Mannheim, Mannheim, Germany

walther.schulze@kit.edu

Abstract: *With ECG imaging it is possible to reconstruct cardiac electrical activity noninvasively from measurements of the electrocardiogram (ECG). To facilitate the reconstruction, an MRI- or CT- based model of the body is required, which is represented as a volume conductor. A mathematically ill-posed problem is solved to reconstruct the cardiac sources from potentials collected on the body surface. To obtain a body surface potential map (BSPM) electrodes are ideally placed allover the entire thorax. In practical applications, however, the number of electrodes is limited and the placing is subject to constraints. We investigate the effect of different electrode setups on the ill-posedness of the inverse problem. In particular, electrode setups are chosen to comply with constraints for female patients in the catheter lab.*

Keywords: *ECG imaging, BSPM, inverse problem*

Introduction

We explore ECG imaging as a method to reconstruct cardiac transmembrane voltages (TMVs) noninvasively from BSPMs [1], with the specific application scenario being the localization, characterization and monitoring of ectopic foci. The imaging of premature ventricular contraction (PVC) has previously been investigated clinically in terms of activation times [2] and epicardial potentials [3].
For ECG imaging BSPMs need to be recorded as an input to the inverse problem algorithm that reconstructs the TMVs in the ventricular myocardium. For a clinical validation study, intracardial signals were recorded simultaneously with the BSPM in a catheter lab.

Methods

While ideally, the BSPM would be acquired on the entire thorax, the following constraints applied in the study:

- **Limited number of electrodes:** BSPM signals were acquired with an 80-channel ECG device by BioSemi B.V. Electrodes are arranged in 4 strips of 12 active electrodes each plus 4 strips of 8 active electrodes each.
- **Requirement to leave space for standard ECG leads:** In the clinical setting, standard Einthoven and Wilson leads had to be derived for patient monitoring. Space for the related electrode patches is required below and around the left breast.
- **Limited flexibility of electrode strips:** Electrode strips cannot always contact the skin with all their electrodes. For female cases, it is assumed that the two electrodes below the breasts are out of touch for vertical placement of the strips. Also, it is assumed that electrodes have bad contact with the skin in the areas above the sternal notch and clavicle.
- **Limited access to the sides:** Access to the sides of the thorax is limited due to the arms, which are not represented in the model of Fig. 1. Also, in general the breasts and the Wilson leads contribute to a limited access to the upper sides.
- **Inaccuracy of the model:** For ECG imaging, the model of the thorax is obtained from pre-interventional imaging. During the intervention, the patient is placed in exactly the same manner and coregistration is performed to map the electrodes on the pre-interventional model. To reduce the modeling error, electrodes are preferably applied on the upper breasts and over the thorax center. A placement of electrodes in peripheral areas is avoided since the geometrical shape is less reproducible here and the model has greater uncertainty.
- **Access to electrodes for localization:** It is assumed that electrodes are localized using a camera system that needs visual access to the area of interest. Electrodes can therefore not be placed on the back of the patient.
- **Limited representation of the lower body:** As models are obtained from thorax scans that are acquired during breathhold, imaging time is limited, and therefore also the imaged thorax volume. For most patients, models end above the navel, and electrodes placed below cannot be considered.

Given the requirements, the following three electrode setups are tested on an MRI-based dataset of a female patient against an ideal setup of 160 equally spaced electrodes (**FULL160**) (see Fig. 1):

- **VERT**: Electrodes are placed vertically, accepting that for most female patients two electrodes are lost in each strip right below the breasts. The more dense 12-lead

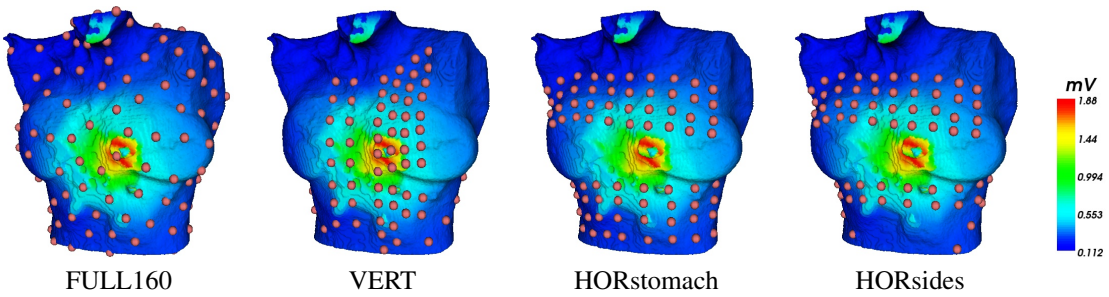

Figure 1: Setups: sum of first 5 singular vectors (each normalized after building the absolute value).

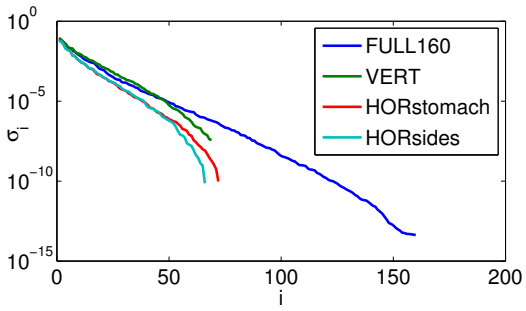

Figure 2: Decay of singular values $sigma_i$ over index i

strips are placed over the heart, two 8-lead strips are placed on the right half of the thorax, two are placed on the left and right sides of the thorax, with three electrodes lost due to the model being cut off at the navel. Altogether, 11 out of 80 channels are lost.

- **HORstomach**: Electrodes are placed horizontally, accepting that a placement on the lowest part of the breasts must be avoided. The 12-lead strips are placed in the upper part of the body, which is assumed to provide the most signal information, with 2 electrodes of each strip being lost since the strips are too inflexible to extend to the sides of the body. This is easier on the stomach, where the 8-lead strips also sample signals from the sides. 8 of the 80 channels are lost.
- **HORsides**: Electrodes are placed as in the HORstomach setup, with the difference being that two 8-lead channels are placed on the sides of the thorax as in the VERT case. 14 of the 80 channels are lost.

For each setup, the singular value decomposition of a lead field matrix A is computed, which represents how single point TMV sources x in the heart are mapped onto the thorax as BSPM b, and the singular values σ_i in S are plotted.

$$Ax = b, \quad svd(A) = USV \tag{1}$$

Results

Singular values for the **VERT** setup decay slowest among the realistic setups (Fig. 2). The **HORstomach** and **HORsides** setups show a decay that is significantly stronger, with that of **HORsides** again cutting off significantly earlier.

Discussion

Given the constraints assumed in this study, the **VERT** setup yields the greatest singular values, which means the inverse problem in ECG imaging is least ill-posed. For best results, this setup should be preferred among the realistic setups. Compared to the ideal case **FULL160**, the **VERT** setup misses singular values from index 55 on. These are all at or below a 10^{-6} order of magnitude. Taking into account that $\sigma_0 \approx 10^{-1}$ these signals can only be identified for a signal-to-noise ratio (SNR) of better than 100 dB. Since this ratio is unrealistically good for a clinical environment, it can be concluded that the **VERT** setup is sufficient to reconstruct all cardiac sources with the same accuracy that would be achieved using the ideal 160-electrodes setup given a specific SNR. Still, there are advantages using the full setup. Given the SNR is worse than 100 dB, even if the singular vectors from index 55 on cannot be measured, it is then more likely that those singular vectors with lower index have components that are statistically dependent. Even if the individual channels' SNR is the same, the inverse solution with the **FULL160** setup is potentially more stable.

Acknowledgements

We thank Uwe Mattler, Kathrin Koziel, Dorothea Schyma and Julia Trächtler for their valueable contributions to the clinical data acquisition and processing. This project was funded by the German Research Foundation under grants DO637/10-1 and DO637/13-1.

Bibliography

[1] W. H. W. Schulze *et al.*, "Activation time imaging in the presence of myocardial ischemia: Choice of initial estimates for iterative solvers," in *Computing in Cardiology*, vol. 39, 9-12 Sept., Krakow, 2012, pp. 961–964.

[2] T. Berger *et al.*, "Single-beat noninvasive imaging of ventricular endocardial and epicardial activation in patients undergoing crt," *PloS one*, vol. 6, p. e16255, 2011.

[3] Y. Wang *et al.*, "Noninvasive electroanatomic mapping of human ventricular arrhythmias with electrocardiographic imaging," *Science Translational Medicine*, vol. 3, p. 98ra84, 2011.

Biomed Tech 2013; 58 (Suppl. 1) © 2013 by Walter de Gruyter · Berlin · Boston. DOI 10.1515/bmt-2013-4157

COMPUTING LEAD-FIELD MATRICES FOR A BODY TISSUE CONDUCTIVITY RANGE

Jones RT[1], Schulze WHW[1], Potyagaylo D[1], Dössel O[1] and Weber FM[1,2]

[1]Institute of Biomedical Engineering, Karlsruhe Institute of Technology, Karlsruhe, Germany
[2]Philips Research Europe, Hamburg, Germany

publications@ibt.kit.edu

Abstract: *A new method to predict changes in a lead-field matrix induced by conductivity variations of a single body tissue is proposed. The approach is based on the principle component analysis (PCA) with three initial lead-field matrices transformed to vectors as input. For each tissue – blood, lungs, muscles and fat – a PCA was carried out. Further, for each tissue the default conductivity value and the conductivity varied by $\pm 50\,\%$ were used to calculate the sample lead-field matrices. The results of the PCAs indicate that for every tissue the first principle component suffices to predict the conductivity-induced changes in the samples. With an interpolation of the scores we additionally show that the prediction is not bound to the sample matrices but moreover every matrix within each conductivity range is possibly estimated and conclusively predicted.*

Keywords: *inverse problem of electrocardiography, lead-field matrix, tissue conductivities, PCA*

Introduction

Overcoming the inverse problem of ECG imaging promises better non-invasive cardiac diagnosis and real-time monitoring of the electrical activities of the heart. An early step of the problem is to accurately determine the lead-field matrix, which is part of the forward problem in ECG imaging. It linearly connects the cardiac electrical activity to the body surface potentials. The so-called forward calculation of a lead-field matrix is time consuming with high computational costs. Further, its initial requirements are a human body segmentation and accurate body tissue conductivities. However, the literature values of these conductivities are not consistent [1]. Changes in lead-field matrices due to conductivity changes must be taken into account by repeating the time-consuming forward calculations.

In this work we used the principal component analysis (PCA) to bypass these inefficiencies. The method discussed in this paper is adopted from Weber et al. [2] in which the influences of the conductivities have been studied in the context of ECG forward calculations. The PCA method reduces the dimensionality of a dataset without significant loss of information.

As initial input for the PCA we generated three sample matrices with a wide range of conductivities for one single tissue. The result of the PCA allows us to simplify the reconstruction by only using the first principal component. With an interpolation of the conductivity-dependent PCA scores all lead-field matrices within the chosen conductivity range are easily reconstructed.

Methods

The computer simulations in this study use the Visible Man dataset as model. In these simulations 64 electrodes are used for measuring the body surface potential and a tetrahedron model with 2143 nodes is fitted into the ventricular myocardium. Thus, each lead-field matrix is made up of 2143 columns and 64 rows. We varied the conductivity of blood B, lungs L, muscles M and fat F which are all referred to as tissues. As initial conductivities for these tissues the values from Gabriel et al. [3] (GG) were used. Further, $+50\,\%$ and $-50\,\%$ of the respective GG value are used for each tissue.

The so-called forward calculation calculates the body surface potentials from the electrical sources in the heart created using the bidomain model [4]. In order to determine a lead-field matrix, one single forward calculation is executed for every single myocardial node. In other words, every node is subsequently turned on with all the others turned off. The results of every node are overlaid and thus a lead-field matrix is obtained. For a new set of conductivities the whole procedure has to be repeated.

For each of the four tissues a PCA was applied separately. We passed three lead-field matrices to every PCA as input data. One of them was reused in every PCA. Thus, a total of nine lead-field matrices with different conductivity compositions were calculated, so that every tissue has three corresponding matrices with its conductivity set to $\pm 50\,\%$ and GG. In order to perform a PCA those three matrices are transformed into long row vectors by putting every row in-line. The PCA input matrix is made up of the transpose of these three vectors as columns.

As the input data of the PCA only yields a minor degree of freedom it is executed with a method based on the singular value decomposition. This more efficient method results in the first $n-1$ principal components $\overrightarrow{p}_j$ where n is the number of input columns of the PCA. Additionally, the PCA returns a mean vector $\overline{x}$ of the input matrix, variance values λ_j for every principal component and a score matrix S with score values $s_{j,i}$ for every principle component j and input point i. For the three input points ($\sigma_i = \pm 50\,\%$, GG; $n = 3$) this method returns two principle components. The reconstruction of the sample vectors $\overrightarrow{x}_{\sigma_i}$ is as follows:

$$\overrightarrow{x}_{\sigma_i} \approx \overline{x} + s_{1,i} \cdot \overrightarrow{p}_1 + s_{2,i} \cdot \overrightarrow{p}_2 \qquad (1)$$

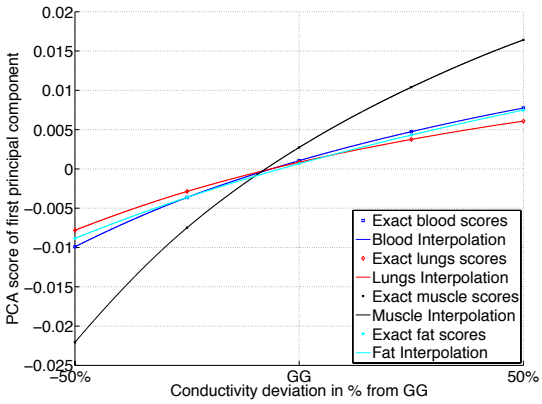

Figure 1: Scores of the first principle component and their interpolation.

Due to $\lambda_1 \gg \lambda_2$ as shown in the results only the first principal component $\overrightarrow{p}_1$ is considered from now on. Moreover the true score values are replaced by a function of their interpolation $s(\sigma_i)$. Now the reconstruction not only allows to calculate the sample vectors but any vector with the tissue conductivity set in between $\pm 50\,\%$.

$$\overrightarrow{x}_{\sigma_i} \approx \overline{x} + s(\sigma_i) \cdot \overrightarrow{p}_1 \tag{2}$$

Finally, the reconstructed vectors $\overrightarrow{x}$ are compared to their real counterpart $\overrightarrow{x}_{ref}$ with the relative error formula 3. As the sample data, every $\overrightarrow{x}_{ref}$ is calculated in a long-term forward calculation.

$$error_{matrix} = \frac{\|\overrightarrow{x} - \overrightarrow{x}_{ref}\|_2}{\|\overrightarrow{x}_{ref}\|_2} \tag{3}$$

Furthermore, the angles of the first principle components of the different PCAs are compared to estimate whether an approach combining the conductivity interactions is reasonable.

Results

The rate between the first and second principle component variances $\frac{\lambda_1}{\lambda_2}$ of the respective PCA is 167, 760, 592 and 754 for blood, the lungs, muscle and fat.
Table 1 shows the relative errors of reconstructions within a single tissue. These reconstructions use equation 2 with the previously forward-calculated true scores or interpolated scores according to the conductivity value.
The angles between the first principle components of all tissues range from $57°$ to $114°$.

Discussion

This paper proposes a method to determine lead-field matrices without the prior knowledge of the body tissue conductivities. It leads to a closed form formula with solely these conductivities as variables. A corresponding lead-field matrix can be obtained immediately with knowledge of real conductivities.

Table 1: Relative errors of the PCA generated matrices with single conductivity variation. The reconstructions used interpolated (i) scores or true (t) scores.

	-50 %	**-25 %**	**GG**	**+25 %**	**+50 %**
Blood	$0.36\,\%_t$	$0.98\,\%_i$	$0.90\,\%_t$	$0.33\,\%_i$	$0.54\,\%_t$
Lungs	$0.13\,\%_t$	$0.35\,\%_i$	$0.33\,\%_t$	$0.16\,\%_i$	$0.21\,\%_t$
Muscle	$0.30\,\%_t$	$1.19\,\%_i$	$1.04\,\%_t$	$0.57\,\%_i$	$0.78\,\%_t$
Fat	$0.15\,\%_t$	$0.37\,\%_i$	$0.39\,\%_t$	$0.19\,\%_i$	$0.24\,\%_t$

Table 1 shows the reconstruction errors of every tissue with the true scores in the columns -50 %, GG and +50 %. This small error is introduced by the negligence of all principle components except the first. The errors of the lungs reconstruction are the lowest which is reasonable because its rate between the first and second principle component is the highest. The errors in column -25 % and +25 % of table 1 cover an additional error which is caused by the interpolation of the scores shown in figure 1. The heretofore maximum error is 1.19 %. Thus, for one single tissue the assumption is valid that any lead-field matrix within the sample range is reconstructed sufficiently with the first principle component and interpolated score values.
The angles between the particular first principle components are all larger than $56.91°$. Although these principle components are not strictly orthogonal, an approach of combining the conductivity influences ought to be possible. However, more profound investigations would exceed the scope of this paper.
In conclusion, this method calculates lead-field matrices more efficiently and is a promising approach to overcome the large computational costs for conductivity adjustments in clinical practice.

Acknowledgement

This project was funded by the German Research Foundation under grants DO637/10-1 and DO637/13-1.

Bibliography

[1] D. U. J. Keller *et al.*, "Ranking the influence of tissue conductivities on forward-calculated ecgs," *IEEE Trans. Biomed. Eng.*, vol. 57, pp. 1568–1576, 2010.

[2] F. M. Weber *et al.*, "Predicting tissue conductivity influences on body surface potentials-an efficient approach based on principal component analysis," *IEEE Trans. Biomed. Eng.*, vol. 58, pp. 265–273, 2011.

[3] S. Gabriel *et al.*, "The dielectric properties of biological tissues: Ii. measurements in the frequency range 10 hz to 20 ghz," *Physics in Medicine and Biology*, vol. 41, pp. 2251–2269, 1996.

[4] D. B. Geselowitz and T. W. Miller, "A bidomain model for anisotropic cardiac muscle," *Annals of Biomedical Engineering*, vol. 11, pp. 191–206, 1983.

Biomed Tech 2013; 58 (Suppl. 1) © 2013 by Walter de Gruyter · Berlin · Boston. DOI 10.1515/bmt-2013-4158

EVALUATING CHANGES IN ELECTROGRAM MORPHOLOGY DURING RADIOFREQUENCY ABLATION OF CARDIAC ARRHYTHMIAS

Keller MW[1], Schuler S[1], Luik A[2], Schmitt C[2] and Dössel O[1]

[1]Institute of Biomedical Engineering, Karlsruhe Institute of Technology (KIT), Germany
[2]Städtisches Klinikum Karlsruhe, Germany

matthias.w.keller@kit.edu

Abstract: *Creating transmural ablation scars in a reliable way is a key issue in improvement of therapeutical procedures for cardiac arrhythmias. About one third of the patients has to undergo several procedures till arrhythmic episodes are successfully treated. Morphological features of intracardiac electrograms might contribute to evaluate scar transmurality during the ablation procedure. We analyzed intracardiac signals before, during and after pointwise ablation in patients with atrial flutter. Unipolar electrograms of the distal electrode showed a relative decrease in amplitude of the second extremum of up to 99 % with a mean of 84±20.6 % after the endpoint of ablation.*

Keywords: *Intracardiac electrograms, catheter ablation, cardiac arrhythmias*

Introduction

Curing cardiac arrhythmias by catheter ablation of myocardial tissue is a frequently used and reliable method. However, about 30 % of the patients have to be treated more than once [1], as created scar tissue partially regains its physiological conductivity during the healing process. Holes in ablation scars occur due to healing of the scar borderzone and small undamaged areas within the scar area. These are frequently seen if scars are not completely transmural. Tissue impedance across the scar as well as signal changes have been investigated aiming at a robust criterion to predict transmurality of radio frequency (RF) ablation scars during procedures. Otomo et. al have found relevant electrogram parameters from intracardiac electrograms (IEGM) recorded in pig atria before and after ablation [2].
Up to date clinical recording systems allow for a recording of IEGM during the ablation process. In this work unipolar and bipolar electrograms have been recorded during clinical ablation procedures. Signal morphology was studied during ablation in order to gain a better knowledge of morphological changes in human remodeled atria.

Methods

Aquisition of clinical signals: In two patients who underwent a routine RF-ablation procedure IEGMs were measured using a four electrode 7F ablation catheter (Blazer, Boston Scientific, USA). Bipolar and unipolar EGM were annotated during the procedure and afterwards one minute segments were exported from the clinical recording system (LabSystem PRO EP, Bard, USA). In our case the Wilson-Central-Terminal lead (WCT) was used as a reference for unipolar EGM. For bipolar EGM the distal electrode signal was subtracted from the corresponding proximal one. Recordings were taken before, during and after point to point RF-ablation for different catheter orientations. Atria were paced from the coronary sinus catheter (CS 7-8) with a cycle length of 600 ms. For each location up to three ablation sequences of 20 s were applied. Intermitted ablation was chosen to receive stable recordings for different stages of scar creation. Signals were filtered with a clinical standard setting using a bandpass between 30-250 Hz.
Preprocessing: Recordings from seven catheter positions (4 parallel, 3 non-parallel) were analyzed by an automatic segmentation workflow. From each recording, a 20 s segment was extracted. For signals during ablation this coincided with the ablation period. For signals before and after ablation the annotation time stamp was used as a starting point. In a first step signals were segmented into active and

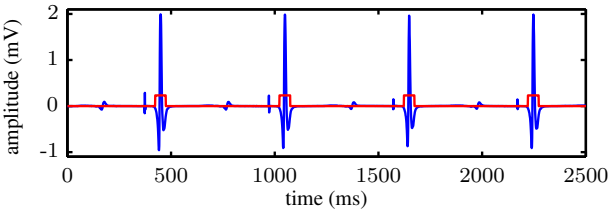

Figure 1: Active segments are automatically detected in a bipolar signal before ablation (blue). Segmentation is indicated by a step function (red), outlining the active segments.

inactive segments using an adaptive thresholding based on the non-linear energy operator (see figure 1) [3].
Extraction of representative templates: For the two distal leads (MAP 1 and 2) of the ablation catheter unipolar and bipolar EGM were studied. Representative templates were created in a stepwise approach. First activations were extracted, denoted by the active segments in the pacing electrode signals. From the activation point the corresponding active segment for the bipolar (MAP 1/2) EGM was marked. Also the unipolar electrograms for both electrodes were extracted by cutting out segments of a length of 125 ms around the activation time of the bipolar signal. For further alignment segments were correlated with an adaptive reference signal, which was initialized by the median of all active segments and stepwise corrected with the mean of all aligned segments. Changes over time were investigated

by creating representative electrogram templates for 5 s sections as mean of corresponding aligned electrograms.

Evaluation of characteristic parameters: For a quantification of signal changes during ablation, amplitudes in local extrema were studied. Local extrema were marked using the *findpeaks* function from Mathworks Matlab ([4]) with a detection threshold of 75 % of the maximum positive and negative amplitude. For each recording location electrogram templates were analyzed in a chronologic order.

Results

Bipolar electrograms: Recording bipolar signals is the standard for clinical procedures. Before ablation these signals showed a biphasic morphology for parallel catheter orientation relative to the tissue surface and a triphasic one for the orthogonal case. For orthogonal signals a drop in amplitude for the second extremum occurred during ablation (Figure 2). Polarity of the extrema depends on the catheter orientation relative to the propagation direction. Taking a closer look at the parallel example signal, also a change in amplitude can be seen (Figure 3). Although, the morphologic pattern changes while ablating. In order to explain this behavior of the bipolar signal, its two components, the two unipolar signals have to be regarded.

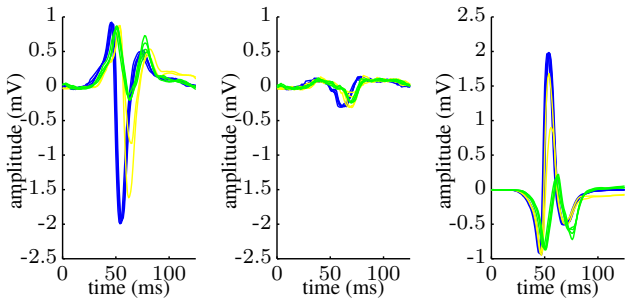

Figure 2: Representative templates of catheter signals for orthogonal catheter orientation: Unipolar distal (left), unipolar proximal (middle), and bipolar (right). Colors indicate time of recording: Before ablation (blue), during ablation (yellow), after ablation (green)

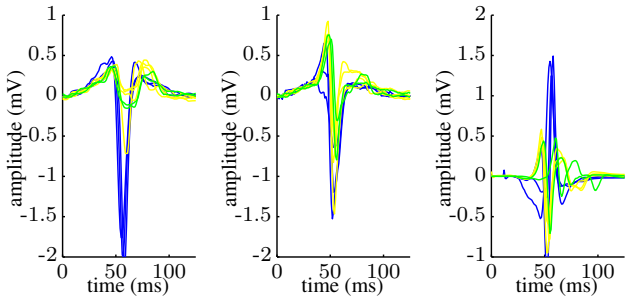

Figure 3: Representative templates of catheter signals for parallel catheter orientation: Unipolar distal (left), unipolar proximal (middle), and bipolar (right). Colors indicate time of recording: Before ablation (blue), during ablation (yellow), after ablation (green)

Unipolar electrograms: Unipolar distal EGM showed similar changes for all catheter orientations, because the distal electrode directly contacts the tissue for all cases. Proximal EGM are strongly changing with orientation, which also influences bipolar EGM morphology. Table 1 displayes amplitude changes in unipolar distal EGM for the first two local extrema occurring over time (polarities are dependent of catheter orientation). Amplitude changes for the second extremum reach up to 99 %, which results in a complete absence of the positive deflection. Five of the seven cases showed a drop greater than 93 %.

Table 1: Amplitudes (mV) for unipolar signals recorded by the distal electrode: **E1:** First extremum, **E2:** Second extremum, **B:** Before ablation, **P:** Post ablation, **RC:** Relative change, **S:** Recording location

	S1	S2	S3	S4	S5	S6	S7
E1 B	0.92	0.43	0.89	0.54	0.42	1.29	0.40
E1 P	0.80	0.21	0.63	0.19	0.11	0.69	0.31
RC	0.12	0.49	0.29	0.65	0.74	0.47	0.23
E2 B	2.00	2.08	0.58	2.00	1.80	2.89	0.88
E2 P	0.15	0.02	0.23	0.03	0.01	0.23	0.45
RC	0.93	0.98	0.60	0.98	0.99	0.92	0.49

Discussion

Unipolar EGM showed reproducible changes in amplitude during the ablation process. Amplitude of the second peak of unipolar EGM might hold as criterion for scar transmurality. It has to be investigated if this feature correlates with the thickness of active myocardium directly underneath the catheter. Also filter settings have to be evaluated, as the commonly used 30 Hz highpass significantly alters signal morphology. Adding metrics for signal morphology to clinical recording systems may lead to improved outcome or ablation procedures.

Bibliography

[1] H. Calkins et al., “Hrs/ehra/ecas expert consensus statement on catheter and surgical ablation of atrial fibrillation,” 2007.

[2] K. Otomo, K. Uno, H. Fujiwara, M. Isobe, and Y. Iesaka, “Local unipolar and bipolar electrogram criteria for evaluating the transmurality of atrial ablation lesions at different catheter orientations relative to the endocardial surface,” *Heart Rhythm : the Official Journal of the Heart Rhythm Society*, vol. 7, pp. 1291–1300, 2010.

[3] M. P. Nguyen, C. Schilling, and O. Dössel, “A new approach for automated location of active segments in intracardiac electrograms,” in *IFMBE Proceedings World Congress on Medical Physics and Biomedical Engineering*, vol. 25/4, pp. 763–766, 2009.

[4] MATLAB, *version 8.0 (R2012b)*. Natick, Massachusetts: The MathWorks Inc., 2012.

Biomed Tech 2013; 58 (Suppl. 1) © 2013 by Walter de Gruyter · Berlin · Boston. DOI 10.1515/bmt-2013-4159

LOCAL REGULARIZATION IN THE INVERSE PROBLEM OF ELECTROCARDIOGRAPHY

Potyagaylo D, Schulze WHW, Dössel O

Institute of Biomedical Engineering, Karlsruhe Institute of Technology (KIT), Karlsruhe, Germany

danila.potyagaylo@ibt.uni-karlsruhe.de

Abstract: *The inverse problem of ECG is the task of cardiac source reconstruction from the measured body surface potential maps (BSPM). It is ill-posed and therefore requires regularization, which is usually applied uniformly to the whole heart geometry. In order to improve the solution quality and localize potentials extrema we propose a local regularization method: the weighting is done iteratively according to the solution spatial content. The performed test showed the ability of the new method to overcome oversmoothing and to better reconstruct strong solution gradients.*

Keywords: *Inverse problem of ECG, Tikhonov local regularization.*

Introduction

The assumption of quasistaticity in the body volume conductor leads to the Cauchy problem for Laplace equation. Our values of interest, the transmembrane voltages (TMV), build the source term for the Poisson equation valid in the cardiac muscle tissue [1]. The problem of finding electrical potentials in the heart is ill-posed, i.e. it is unstable with respect to the measurement and modeling errors. Several mathematical techniques exist to overcome this obstacle, among them the most famous one is Tikhonov regularization [2].

Methods

The idea of Tikhonov regularization is to introduce a stabilizing parametric functional enforcing desired properties of the sought solution:

$$x = \underset{x}{\operatorname{argmin}}\{\|Ax - y\|^2 + \lambda^2 \|Lx\|^2\}, \qquad (1)$$

where $A \in \mathbb{R}^{m\times n}$ is the lead-field matrix, an operator connecting the cardiac sources to the measurement points, $y \in \mathbb{R}^{m\times 1}$ - BSPM, $x \in \mathbb{R}^{n\times 1}$ - TMV, λ - regularization parameter, $L \in \mathbb{R}^{p\times n}$ - regularization operator. In practice the most common types of the matrix L are identity or the matrices of spatial derivatives. In this work we used a finite element discretized version of the Laplace operator ($p = n$), thus requiring smoothness of our solution.

When using L_2 norm in the regularization functional (1), this minimization problem has a closed form solution:

$$x = (A^T A + \lambda^2 L^T L)^{-1} A^T y \qquad (2)$$

The invertion in (2) can be efficiently done with use of SVD (in case of L being an identity matrix) or GSVD in general case [3]:

$$A = U\ [0,\ \Sigma]\ X^{-1}, \qquad L = V\ [M,\ 0]\ X^{-1} \qquad (3)$$

where $U \in \mathbb{R}^{m\times m}$, $V \in \mathbb{R}^{n\times n}$ - orthonormal matrices, $X \in \mathbb{R}^{n\times n}$ is a nonsingular matrix, $\Sigma = diag\{\sigma_k\}$, $M = diag\{\mu_k\}$, $k = 1, ..., m$. The singular values σ, μ are ordered in non-decreasing and non-increasing order respectively and are normalized such that $\sigma_i^2 + \mu_i^2 = 1$. The generalized singular values of the pair $[A, L]$ are defined as $\gamma_i = \sigma_i/\mu_i$, $i = 1, ..., n$.

Having performed this decomposition (must be done only once), the solution can be represented by the following formula:

$$x = \sum_{i=1}^{m} f_i \frac{u_i^T y}{\sigma_i} x_i \qquad (4)$$

where f_i are filter factors. Their choice is the key difference between various regularization techniques and should be done in such a way that the contribution from smaller singular values σ_i in $(u_i^T y/\sigma_i)x_i$ is effectively filtered out [3]. For the Tikhonov second order regularization given by functional (1) the filter factors are:

$$f_i = \frac{\sigma_i^2}{\sigma_i^2 + \lambda^2 \mu_i^2} = \frac{\gamma_i^2}{\gamma_i^2 + \lambda^2}. \qquad (5)$$

From this formula it follows that the same amount of regularization is applied for all solution components which leads in general to the partial (geometrically) oversmoothing. The method could be however improved by local regularization. Instead of a single parameter λ we introduce a vector of regularization parameters $\lambda = \{\lambda_1 ... \lambda_n\}$ that would allow for a different amount of weighting for each source point.

The initial estimate of the solution is obtained by (4) with L-curve criterion for choosing an optimal regularization parameter [4]. Then based on the solution spatial derivatives we iteratively update the regularization vector:

$$\lambda_i^{k+1} = \lambda_i^k \cdot \frac{max(|Lx_k|)}{|Lx_k|_i}, \quad i = 1, ..., n;\ k = 1, ... \qquad (6)$$

with i, k being vector components and iteration numbers respectively. The problem (2) is solved for each iteration to obtain the next estimate of x. The formula (6) implies increasing the parameter λ for regions with small spatial derivatives hence forcing the Laplacian to take smaller values, i.e. equalizing the respective solution components.

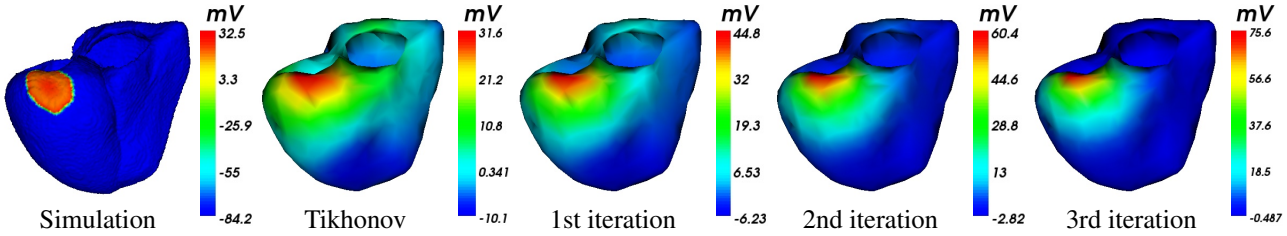

Figure 1: The transmembrane voltages for one time instance of an extrasystole simulation

The areas possessing the strongest gradients are slightly changed, since the corresponding parameters experience only minor modifications.

Results

A result of such iterative procedure is given by Fig. 1. For a simulated left ventricular extrasystole the reconstruction was made for the time instance $t = 20\,ms$ after its initiation. As it can be seen, the Tikhonov reconstruction provides a good initial estimate of the true solution. Despite the fact that the area with highest TMV values is well recovered, regularization in L_2 sense smoothes equally the whole domain, which can result in small derivatives over the heart and, as a consequence, the correlation coefficient of only 5%. After performing several times iterative local reweighting these effects are flattened out and only the region of interest is remained. The correlation coefficients for the first three iterations of the proposed method are 54%, 62% and 68% respectively.

Discussion

In this work we considered a local regularization for the inverse problem of ECG where all solution components could have different weights.

Oster and Rudy proposed in [5] a regional regularization which is based on the decomposition of BSPM into a set of submaps for a spherical geometry using Legendre polynomials, i.e. their method is operating in the space of measurements. Johnson and MacLeod ([6]) investigated a local GSVD based regularization varying the amount of smoothness for sub-matrices of a global transfer matrix, these submatrices represent different geometry regions. The most similar to our method approach was implemented by Ahmad and Brooks in [7]. But in contrast to the present work they weight the regularization matrix with the Laplacian of the true solution taken from simulation.

For the case treated in this work the solution delivered by Tikhonov regularization was of good quality and the iterative procedure improved its main features. In our future work we will analyze the behavior of the algorithm with worse initial solution estimates; the question would be, how to do weighting in a softer way, without overemphasizing initial false extrema.

Another interesting aspect could be to investigate the necessary number of iterations and find the connection between the optimal number of iterations and optimal local weights on the one hand and the amount of noise on the other. As the noise is not commonly known in practice and there are always some modeling errors present, it would be interesting to evaluate the performance of the algorithm with respect to lower and upper bounds noise estimates.

Acknowledgement

This work was funded by German Research Association under grant DO 637/13-1.

Bibliography

[1] D. B. Geselowitz and T. W. Miller, “A bidomain model for anisotropic cardiac muscle,” *Ann Biomed Eng*, vol. 11, pp. 191–206, 1983.

[2] A. N. Tikhonov and V. Y. Arsenin, *Solutions of ill-posed problem*. Winston&Sons, New York, 1977.

[3] P. C. Hansen, *Rank-deficient and discrete ill-posed problems: Numerical aspects of linear inversion*. Siam, 1999.

[4] C. Hansen, “Analysis of discrete ill-posed problems by means of the l-curve,” *SIAM Review*, vol. 34, pp. 561–580, 1992.

[5] H. S. Oster and Y. Rudy, “Regional regularization of the electrocardiographic inverse problem: a model study using spherical geometry,” *IEEE Trans. Biomed. Eng.*, vol. 44, pp. 188–199, 1997.

[6] C. R. Johnson and R. S. MacLeod, “Adaptive local regularization methods for the inverse ecg problem,” *Progress in Biophysics & Molocular Biology*, vol. 69, pp. 405–423, 1998.

[7] G. F. Ahmad, D. H. Brooks, and R. S. MacLeod, “An admissible solution approach to inverse electrocardiography,” *Ann Biomed Eng*, vol. 26, pp. 278–292, 1998.

Biomed Tech 2013; 58 (Suppl. 1) © 2013 by Walter de Gruyter · Berlin · Boston. DOI 10.1515/bmt-2013-4160

HIGH-LEVEL FEATURE EXTRACTION FROM ELECTROPHYSIOLOGICAL BRAIN SIGNALS IN THE TIME-FREQUENCY DOMAIN

René Heideklang and Galina Ivanova

Institut für Informatik, Humboldt-Universität zu Berlin, Deutschland

heidekla@informatik.hu-berlin.de

Abstract: *In this study, an application of modeling smooth patterns of signal power in the time-frequency domain is presented. This novel technique called SnaGe was recently developed and is applied to real EEG data here. In particular, its benefits for single trial analysis are highlighted. Models of varying degrees of freedom are fitted to the chosen data set, emphasizing the trade-off between goodness of fit and interpretability.*

Keywords: *Time-frequency analysis, Feature extraction, Model fitting, Signal analysis*

Introduction

The electroencephalogram (EEG) is the longest-studied noninvasive technique to measure brain signals. In the last decades, elaborate signal processing tools have been developed to automatically extract relevant information from the data. This task is quite challenging, owing to the complexity of the human brain. Indeed, each EEG measurement represents merely a snapshot of brain signals, but which are in fact varying: Even in a fixed experimental setting, the obtained signals exhibit considerable intra-individual and inter-individual biological variability. Yet, standard analysis techniques, such as time-frequency decompositions, do not appropriately account for this effect. For example, while they allow to study the signals at different time/frequency points, such precise information about regions of interest is often not available, e.g. because of the inherent variability. Usually, information from many neighboring time-frequency locations is therefore averaged, or the issue is simply ignored and the locations are treated as being independent. Both strategies, however, are not satisfactory: Either precise localization is lost, or the full potential of the data is not used. Thus, there is a need for adaptive signal representations which explicitly quantify the data *patterns* generated by the underlying biological processes.

In a previous paper, the authors published such an abstract representation called *Smooth Natural Gaussian Extension* (SnaGe) model [1]. Similarly to the well-known bivariate Gaussian function, this parametric model can be fitted to power distributions in the time-frequency domain, which are interpreted as images. Thereby obtained model parameters form high-level descriptors (*features*) about the data patterns. As these patterns may be too complex to be captured by a Gaussian peak, SnaGe is designed to represent whole paths of prominent signal power in the time-frequency domain. This path is essentially a smooth interpolating curve, and a surface is defined by exponential decay w.r.t. increasing distance from the path.

In this study, the previously developed and published technique is applied to a data set of real EEG measurements. The promising ability to analyze single trial recordings is demonstrated. To this end, an induced oscillation in the alpha band is investigated and the obtained high-level signal characteristics are presented.

Methods

An exemplary data analysis by means of the SnaGe method is carried out. The data set in this study stems from a motor experiment. Participants were asked to press a button with their index finger in reaction to a visual stimulus. EEG was measured at a sampling rate of 500 Hz from 128 channels according to the 10-20 system. Linked mastoids formed the reference channel. Response-locked trials were extracted, and after standard pre-processing, the signals are transformed to the time-frequency domain by the Short-Time Fourier Transform. The focus is on the investigation of induced neural activity in a region of interest around the alpha band (8–13 Hz), during the first four seconds after the response. A relevant channel localized near the motor and sensory-motor cortical area was selected for this demonstration. An example for a single trial signal is plotted in Fig. 1. A prominent pattern of event-related synchronization of neuronal activity is apparent in the visualization. In order to analyze the oscillation in the alpha band, different bivariate SnaGe models are fitted to the dynamic power spectrum image.

One fundamental decision to be made is the model order. While low-order models are robust to small perturbations of the signal, they might not be able to represent increasingly complex patterns. Higher-order models, on the other hand, are more prone to over-fitting, but offer greater flexibility. Therefore, in this study SnaGe models of order 5,6,7 and 8 are fitted. Also, as proposed in [1], the strategy of iteratively refining models of low order to yield more and more complex pattern representations can be useful for robust parameter extraction. Thus, in another experiment, an initial 5th order model is refined multiple times, which results in an additional 8th order representation. Lastly, the effects of taking into account a-priori knowledge about the data are studied. Because it is known that the neural excitement displays as a horizontal path of increased signal power

in the time-frequency representation, paths going backward in time should be punished. This behavior can be prevented by adding a penalty term to the optimized cost function.

Results

Six SnaGe models are computed, whose predictions are shown in Fig. 1. To objectively compare these results, the goodness of fit is computed as the root mean squared error (RMSE) between the preprocessed time-frequency data and the models' predicted images, see Table 1.

All six models are able to approximate the pattern in the data, which is reflected by the overall low RMSE values. In general, higher-order models produce better matches, especially concerning values of signal power. Although the overall time-frequency distribution of signal power is almost always represented well, there are significant differences regarding the course of the modeled path (represented by white lines in Fig. 1). In particular, the 7th-order model and the refined model without regularization both exhibit loops in the SnaGe path. While such results impair interpretability as a path of instantaneous frequency, it is also clear that the obtained models are optimal in terms of goodness of fit. Among the other solutions which are free of loops, the 8th-order model is most accurate, followed by the refined regularized 8-th order result.

After meaningful parameters are extracted, they can form the basis for further analyses. As a simple demonstration, the mean frequency value along the modeled path is computed here. To this end, the most accurate loop-free model's curve is densely sampled, resulting in a mean value of 10.4 Hz. These observations are discussed in detail in the following section.

Table 1: Goodness of fit (gof) according to root mean squared error.

experiment	**gof**
order 5	67.18
order 6	59.20
order 7	**56.84**
order 8	56.94
order 8 (refined)	**55.59**
order 8 (refined, regularized)	57.59

Discussion

The most accurate solutions were obtained by models of higher order, owing to the pattern's complexity. However, the more flexible models tend do develop loops in their paths, which shows that there usually is a trade-off between interpretability and goodness of fit.

The SnaGe is built on several model assumptions, most importantly it is designed for mono-component signals. This assumption can often be justified by filtering or masking other components, as it was done here by the application of a region of interest. However, the target pattern will never

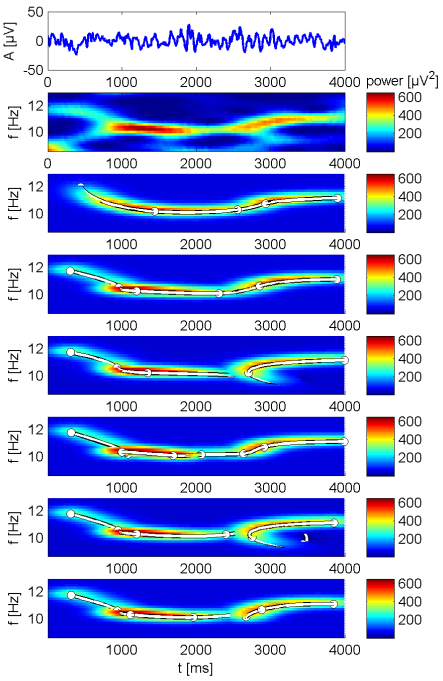

Figure 1: EEG single trial (top), time-frequency representation (2nd row) and several fitted SnaGe models (3rd to 8th row: order 5,6,7,8,8(refined),8(refined and regularized).

be ideal in this sense, for example there seems to be a peak off the main path of activation at 3000 ms / 9 Hz. Loops are the only means to compensate for such violated model assumptions and may be sources of over-fitting. In fact, this shows the optimization algorithm's strength to travel long distances in parameter search space to obtain very different, but in fact more optimal (w.r.t. the cost function, i.e. RMSE) solutions.

It was shown that the SnaGe model is able to accurately extract high-level features in the form of a time-frequency-power path of neural oscillatory activity. The stated trade-off can be controlled by adding penalty terms to the cost function. SnaGe is an appropriate tool for single trial analysis, since it is able to automatically adapt to the distribution of signal power and thus takes into account the biological variability. This suggests the method's potential as a measure of event related synchronization / desynchronization (ERS / ERD). Also, derived high-level features such as mean pattern frequency may be useful, for instance for the objective discrimination of groups of subjects in applied studies.

Bibliography

[1] R. Heideklang and G. Ivanova, "A novel flexible model for the extraction of features from brain signals in the time-frequency domain," *International Journal of Biomedical Imaging*, vol. 2013, pp. 1–12, 2013.

Biomed Tech 2013; 58 (Suppl. 1) © 2013 by Walter de Gruyter · Berlin · Boston. DOI 10.1515/bmt-2013-4161

EEG CONTROLLED NI LEGO ROBOT: FEASIBILITY STUDY OF SENSORIMOTOR ALPHA RHYTHM NEUROFEEDBACK IN CHILDREN

B. Mirković[1], M. Stevanović[1], A. Savić[1]

[1]School of Electrical Engineering, University of Belgrade, Serbia

bojanamirkovic88@yahoo.com

Abstract: *We present a feasibility study of the novel system for EEG based neurofeedback. The proposed system can provide both continuous visual feedback on the computer screen and discrete reinforcement (movement of the NI LEGO Mindstorms robot) when the task is executed. We have tested the NF system on 31 children subjects (6-15 years). The subjects' task was to increase their alpha band power by using the continuous feedback. When the power level reached the predefined threshold, the command was sent to the robot to make a step which was considered a successful task execution. The preliminary results showed an overall increase of robot-activations during the course of the trials.*

Keywords: *EEG, alpha rhythm, neurofeedback.*

Introduction

Neurofeedback (NF) is a form of biofeedback during which the subjects train to voluntarily modulate their brain activity in terms of frequency, location or amplitude [1]. Slow cortical potentials (SCP) such as contingent negative variation or specific frequency band-power (BP) can be used in design of NF paradigms [2]. Previous studies have showed that increase of upper alpha BP by NF training resulted in enhanced cognitive control in healthy subjects [3]. Theta/beta training and SCP were found to be effective in treating attention-deficit/hyperactivity disorder (ADHD) in children [4]. Alpha NF was proven to be effective in treatment of depressive symptoms [5]. Sensory motor rhythm NF was used for improvement of motor skills or for enhancement of the lost/impaired motor function after stroke or brain injury [6]. Alpha rhythm NF could be used for training of relaxation or stress level reduction [7]. The goal of this study was to explore the alpha rhythm in the beginning stages of idle state when person is highly focused on the task of resting. For this purpose we have designed a novel system for NF consisting of commercial EEG device, custom made NI LabView based NF software and NI LEGO Mindstorms robot which we have tested in children subjects.

Methods

A. Experiments and data acquisition

1) *Subjects:* Thirty six subjects, all between 6 and 15 years of age, took part in this study. Experiments were conducted at the *Festival of robotics 2012* held in Belgrade, where children participated as volunteers in the tests.

2) *Instrumentation and setting:* Subjects were seated on a chair and a NI LEGO Mindstorms robot was placed on a table in front of them. EEG was recorded in bipolar configuration, C3 referenced to C4, with two Ag/AgCl electrodes placed according to International 10-20 standard. Ground electrode was located on the subject's forehead. Acquisition system used for EEG recording was PSYLAB EEG8 electrophysiology signal amplifier combined with PSYLAB SAM unit (Contact Precision Instruments, London, UK). During the measurements the impedance was less than 5 kΩ. Gain was set on 20000, while the signals were hardware filtered in a range 0.1-40 Hz. All signals were sampled at 500 Hz using NI USB-6212 (National Instruments, Austin TX) A/D card. System is operating on-line using custom made NI LabView 2009 (National Instruments, Austin, Texas) software for EEG acquisition and processing, with algorithm for frequency BP calculation.

B. Neurofeedback

In this study alpha band ranging 8-13 Hz was used for NF. EEG is first band-pass filtered with 5th order Butterworth filter to extract the alpha activity. EEG band-power time course was estimated by squaring and averaging the band-pass filtered signal in a time window of 1 second with a 90% overlap between the two consecutive windows. Subjects were provided with continuous visual feedback on the computer screen projection on the wall in front of them, in the form of a sliding bar whose size corresponded to the current alpha BP, refreshed for each time window. Second type of feedback, the control of NI LEGO robot, was implemented through operand conditioning paradigm using discrete reinforcement. For each subject the reference power was determined before the trial, as the mean alpha power during the 10s of rest and the detection threshold (TH) was the reference value multiplied by 2. Whenever the EEG BP remained above the TH for at least 5 consecutive windows (corresponding to the dwell time of 500 ms), this was accounted as one detection. After the detection, the command was sent via bluetooth connection to the robot to make a step. Therefore the number of steps that the robot made was directly proportional to the detection count i.e. to the retention time of EEG alpha power above the threshold. Subjects were instructed to relax while sitting still and try to move the robot. They were also informed that the continuous visual feedback in the form of a sliding bar can help them to achieve a result by trying to increase the bar value until

the robot starts moving. One trial per subject was recorded with duration of 45 seconds.

Results

The EEG signals were visually inspected for noise/artefacts and the noisy power-signals were omitted from further analyses, leaving signals from 31 subjects. Raw EEG was processed offline for obtaining the same BP time courses that were used for delivering the feedback online. These BP time courses were normalized from 0 to 1 and averaged over subjects, shown on figure 1. This average shows higher amplitude bursts of alpha activity in the second half of the trial, possibly due to the presented feedback.

For analyzing overall distribution of detections in time we have divided the single trial duration on three consecutive non-overlapping 15 second time intervals (TI_n, n=1-3). The detection rate per each time interval ($DR(TI_n)$, n=1-3) was calculated using the following equation:

$$DR(TIn)[\%] = D(TIn)/D, n = 1-3 \quad (1)$$

where $D(TI_n)$ was sum of all subjects' detections in interval TI_n, and D was the total number of detections for all subjects. Obtained values for detection rates were: $DR(TI_1)$=16,3%, $DR(TI_2)$=29.8% and $DR(TI_3)$=53.9%. These values indicate an increase of detection count during the course of the trial.

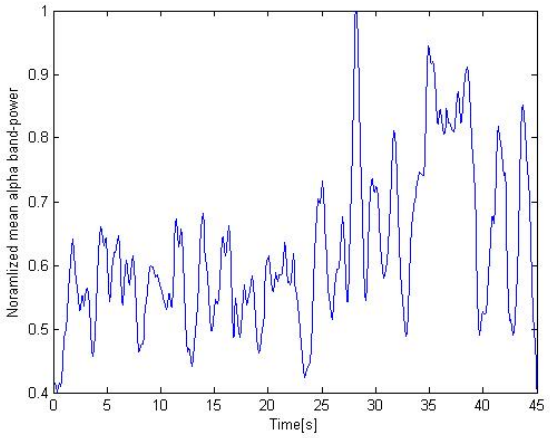

Figure 1. Grand average over 31 subjects of EEG alpha-band power time courses for C3-C4 channel.

Discussion

In this study we have tested a feasibility of using NF software that we have developed in combination with a NI LEGO Mindstorms robot that we used as a means for providing interesting feedback for participants. Subjects' motivation i.e. will to apply and effort to perform a task plays an important role especially in children.

From the collected data we can conclude that the power fluctuations, possibly partly as a result of the both types of presented feedback, are in the form of alpha activity bursts rather than a steady increase of alpha BP. These bursts might have originated from attention shifts resulting in power drops, occurring when the discrete feedback, the robot movement, was presented. That could be explained by subjects' eagerness to see the robot walk or distractions by the sound that the robot movements produced. The main advantage of the proposed system for NF in children is the robot-movement feedback, which was conceived to be interesting and motivating for the potential users to undergo the NF treatment. Additionally, the developed software can be used for providing feedback on other frequency bands of interest such as theta, upper alpha or beta, commonly used for NF.

Acknowledgement

We would like to acknowledge the BMIT group (Group for Biomedical Instrumentation and Technologies, http://bmit.etf.rs/) for providing all the necessary instrumentation for this experiment. Our gratitude also extends to the Centre for Promotion of Science, as the organizers of *Festival of robotics 2012*, without which these experiments wouldn't be possible in this extent.

Bibliography

[1] Congedo M.,Lubar J.F., and Joffe D. : Low-resolution electromagnetic tomography neurofeedback, IEEE Trans. on Neuronal Systems & Rehabilitation Engineering, vol. 12, pp. 387-397, 2004

[2] Gevensleben H., Holl B., et. al.: Is neurofeedback an efficacious treatment for ADHD? A randomised controlled clinical trial, *J Child Psychol Psychiatry*, vol. 50, pp.780-789, 2009

[3] Benedikt Z., Huster J.R., and Herrmann C.S.: "Neurofeedback training of the upper alpha frequency band in EEG improves cognitive performance." *Neuroimage*, vol.54.2, pp. 1427-1431, 2011

[4] Drechsler R., Strau M., Doehnert M.,et.al: Controlled evaluation of a neurofeedback training of slow cortical potentials in children with Attention Deficit/Hyperactivity Disorder (ADHD). *Behavioral and Brain Functions*",pp. 3-35, 2007

[5] Choi, S.W., Chi, S.E., et. al. :Is alpha wave neurofeedback effective with randomized clinical trials in depression? A pilot study". *Neuropsychobiology*, vol. 63, pp. 43-51, 2011

[6] Kai Keng Ang *K.K*, Cuntai Guan C.: Brain-Computer Interface in Stroke Rehabilitation", *Journal of Computing Science and Engineering*, vol. 7, No. 2, , pp. 139-146, June 2013

[7] Boxtel, G.J., et al. "A novel self-guided approach to alpha activity training." *International Journal of Psychophysiology*, vol. 83, no.3, pp. 282-294, 2012

Biomed Tech 2013; 58 (Suppl. 1) © 2013 by Walter de Gruyter · Berlin · Boston. DOI 10.1515/bmt-2013-4162

CIRCULAR CORRELATION COEFFICIENTS VERSUS THE PHASE-LOCKING-VALUE

Katrin Pauen and Galina Ivanova

Departement of Computer Science, Humboldt-Universität zu Berlin, Germany

katrin.pauen@informatik.hu-berlin.de

Abstract: *The phase-locking-value is one of the most popular measures to quantify bivariate phase coupling. Recently, the use of more complex circular statistical methods for the quantification of synchronization has been discussed. Motivated by these new developments, the PLV is compared with a simple and a multiple circular-circular correlation coefficient. In the process, the reliability of the three measurements is tested using simulated signals and their applicability to real EEG data is demonstrated. Finally, advantages and disadvantages of the methods are discussed.*

Keywords: *Circular-circular correlation, EEG, synchronization, phase coupling, phase-locking-value*

Introduction

The synchronization of different physiological processes represents an important issue in many biomedical research fields. Coupling may not only occur within one physiological system, as for instance the brain, but also between distinct systems, as heartbeat and respiration show [6]. Thus, the quantification of such coupling is a crucial objective in biomedical signal analyses and a lot of coupling measures have already been introduced [1]. However, many of these measurements mix amplitude and phase information and cannot quantify phase synchronization regardless of existing amplitude dependencies. To capture pure phase relationships, the instantaneous phases of the signals have to be considered. The most popular measurement using this approach is certainly given by the phase-locking-value PLV [3]. This measure calculates bivariate phase differences and quantifies rotations and reflexions of the circular phase variables. Recently, the benefit of more complex circular statistical methods for the quantification of phase associations has been discussed and two multiple circular-circular correlation coefficients have been presented [4]. But can these more complex coefficients keep pace with the old-established phase-locking-value? This question will be addressed in the present paper.

Methods

In the following, the PLV will be compared with the most promising multiple circular-circular correlation coefficient, namely the coefficient according to Jupp and Mardia $r^2_{m,JM}$ [4], and its simple counterpart $r^2_{s,JM}$ [2]. In the process, the two most important properties of a reliable coupling measure will be investigated. Firstly, it should take values close to one if synchronous or phase-coupled signals are considered. Secondly, the values should draw near zero if asynchronous signals are examined. To study these characteristics in detail, a comparable set of synchronous and asynchronous signals is required. To this end, 100 asynchronous oscillators s_k are simulated each consisting of 15 added cosines with integer frequencies $f_i \sim U(1, 30)$ and belonging amplitudes $A_i \sim N(20/f_i, 2^2)$. Subsequently, various phase-coupled signals $s_k^{(l)}$ are obtained to each oscillator s_k by inserting a pseudorandom phase shift $\alpha_l \sim U(-\pi, \pi)$. An example for two such coupled oscillators $s_1^{(1)}$ and $s_1^{(2)}$ and an according asynchronous signal $s_2^{(1)}$ is illustrated in fig. 1. To simulate various realizations of the same process,

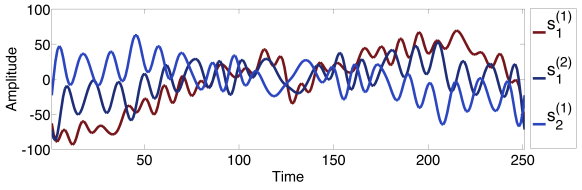

Figure 1: Exemplary illustration of the simulated signals.

it is assumed that the amplitudes and frequencies of an oscillator remain stable, while its zero phases vary slightly from trial to trial following a von Mises distribution with $\varphi_0 \sim M(\mu, 1)$ and $\mu \sim U(-\pi, \pi)$. Finally, a normally distributed phase noise $w(j) \sim N(0, 0.12)$ is added to the zero phases of the oscillators and they are superimposed with some gaussian noise $n(j, t) \sim N(0, 52)$ since real biomedical signals are commonly noisy. To estimate the instantaneous phases of the signals, the Hilbert transform is utilized.

Results

Obviously, a comparison of simple and multiple synchronization measures is only partly possible. Whereas the PLV and the simple coefficient can only take into account two signals, the multiple coefficient requires at least three oscillators of which two function as predictors. To assure maximal comparability, this additional second predictor is always chosen to be phase-locked to the first one. Unlike the circular correlation coefficients, the PLV may only be utilized in multi trial analyses. Thus, the performance of all measures can only be compared in this kind of examination in which the extent of synchronization is estimated for every point in time. As the synchrony, or asynchrony, between the oscillators remains stable over time, these estimates can then be averaged. Tab. 1 shows the mean results for 100 ex-

aminations as well as the belonging percentages of significant tests. These tests are chosen according to the different measurements and are performed with a significance level of 0.01. Obviously, the PLV exhibits the highest values

Table 1: Results for simulated data.

measure	**synchronous**		**asynchronous**	
	value	sig. tests	value	sig. tests
PLV	0.8985	98.71 %	0.1848	33.33 %
$r^2_{s,JM}$	0.8082	98.16 %	0.0205	01.46 %
$r^2_{m,JM}$	0.8436	98.45 %	0.0413	01.26 %

together with the greatest proportion of significant tests in both conditions. Furthermore, the multiple correlations are higher than their simple counterparts. Regardless of these minor differences, all measurements provide good results for truly phase-coupled signals: at least 98.16% of the tests carried out indicate a dependency. Thus, the first quality criteria, values close to one for synchronous signals, is fulfilled by all measures. Unfortunately, these good outcomes cannot be replicated for asynchronous signals. Although all values remain below 0.1848, 33.33% of the phase-locking-tests become falsely positive. In contrast, the percentage of wrongly significant tests for the circular coefficients does not exceed 1.46% and is even lower for the multiple coefficient. Hence, the extent of phase-coupling may be overestimated with the phase-locking-value. The same pattern,

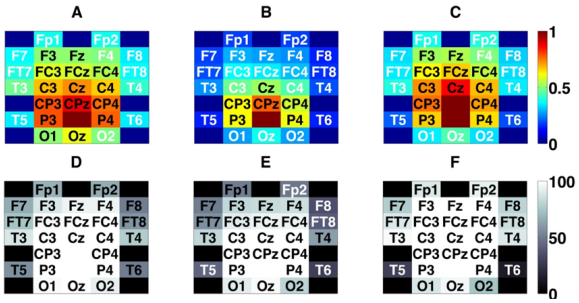

Figure 2: Estimated theta couplings (**A**-**C**) and according percentages of significant tests (**D**-**F**). **A**: PLV, **B**: $r^2_{JM,s}$, **C**: $r^2_{JM,m}$, **D**: PLV-tests, **E**: $r^2_{JM,s}$-tests, **F**: $r^2_{JM,m}$-tests.

comparable high overall values for the PLV, is observable in an exemplary analysis of real EEG data. Here, a randomly selected data set of an acoustic oddball experiment is chosen that consists of 40 trials and 28 electrodes with mastoids as reference. In accordance with current research, induced theta oscillations following a P300 are examined and fronto-central couplings are expected [5]. To this end, signals are initially preprocessed in an appropriate manner and theta is filtered out using a butterwort filter of passband 4-8 hertz. Subsequently, the instantaneous signal phases are extracted using the Hilbert transform. As midline couplings are expected, electrode Pz, and for the multiple coefficient additionally CPz, is chosen as predictive variable and the extent of synchronization with every other electrode is estimated. This is done within a time segment from 500 to 3000 ms after target presentation in multi trial analyses. Fig. 2 **A** shows the time-averaged results for the PLV, while picture **B** illustrates the outcomes for the simple circular-circular correlation coefficient and picture **C** the according values for the multiple one. In addition, illustration **D** - **F** depict the corresponding percentages of significant tests that all capture the suspected fronto-central couplings. In contrast, only little up to low correlations with electrodes FCz (0.3461) and Fz (0.2764) can be achieved with the simple coefficient. However, the multiple correlations with these electrodes (FCz: 0.6657; Fz: 0.5460) are even higher than the corresponding PLVs (FCz: 0.5749; Fz: 0.5060) along with more significant test results (FCz: 100%; Fz: 100% versus FCz: 94.72%; Fz: 98.56%).

Discussion

In total, circular-circular correlation coefficients are well suited to estimate phase-coupling in a reliable manner. Although they take slightly lower values than the PLV together with less significant test results for simulated data, they can keep pace with this traditional measure. Unlike the PLV, they are even able to distinguish between truly phase-coupled and just individually phase-locked signals. Furthermore, they are not restricted to bivariate analyses and can include an arbitrary number of predictive variables. As the circular coefficients may also be utilized in single trial analyses, a further evaluation of this new circular approach seems worthwhile. In the process, particular attention should be paid to the multiple coefficient since this measure exhibited even higher midline coupling estimates than the PLV.

Bibliography

[1] K. J. Blinowska, "Review of the methods of determination of directed connectivity from multichannel data," *Med. Biol. Eng. Comput.*, vol. 49, pp. 521-529, 2011.

[2] P. E. Jupp and K. V. Mardia, "A general correlation coefficient for directional data and related regression problems", *Biometrika*, vol. 67, pp. 163-173, 1980.

[3] J.-P. Lachaux, E. Rodriguez, J. Martinerie and F. J. Varela, "Measuring Phase Synchrony in Brain Signals," *Human Brain Mapping*, vol. 8, pp. 194-208, 1999.

[4] K. Pauen and G. Ivanova, "Multiple Circular-Circular Correlation Coefficients for the Quantification of Phase Synchronization Processes in the Brain," *Biomedical Engineering*, vol. 0, pp. 1-15, 2013.

[5] J. Yordanova and V. Kolev, "Single-sweep analysis of the theta frequency band during an auditory oddball task," *Psychophysiology*, vol. 35, pp. 116-126, 1998.

[6] C. Schäfer, M. G. Rosenblum, H.-H. Abel and J. Kurths, "Synchronization in the human cardiorespiratory system," *Physical Review E.*, vol. 60, pp. 857-870, July 1999.

Biomed Tech 2013; 58 (Suppl. 1) © 2013 by Walter de Gruyter · Berlin · Boston. DOI 10.1515/bmt-2013-4163

CORRECTION OF EYE-MOVEMENT ARTIFACTS OF DC-EEG SIGNALS

A. Kerekes[1], T. Wartzek[1], S. Leonhardt[1]

[1]Chair for Medical Information Technology, RWTH Aachen University, Germany

kerekes@hia.rwth-aachen.de

Abstract: *For neurofeedback applications EEG frequencies below 0.5 Hz including DC-offset are essential. Since artifacts from eye movement can be found in the same frequency band of the so-called DC-EEG, these artifacts must be removed for proper DC-EEG analysis. To remove artifacts from eye movement, simultaneous electrooculograms (EOG) are recorded as an indicator. The clean EEG is then found by subtracting the EOG from the measured EEG. However, most approaches also remove the DC-part of the EEG in the process. We propose an adaptive algorithm to eliminate eye movement artifacts from an EEG in real-time while maintaining the DC-offset utilizing a recursive least squares approach.*

Keywords: *DC-EEG, neurofeedback, EEG signal processing*

Introduction

The method "slow cortical potentials" (SCP) is often applied for EEG-neurofeedback sessions. The principle is to detect slow changes of the EEG signal's baseline. Before analysis, pre-processing of the signal has to be conducted, especially to remove artifacts caused by eye movements. Most algorithms remove the DC-offset before signal processing. For example, methods for source separation like principal component analysis (PCA) or independent component analysis (ICA) need to subtract the mean of the signal.

Until now, as seen in [1], only the least squares (LS) approach has proven to sustain the offset if, during calibration, the ratio of EOG to EEG is high [4]. The obtained parameters β_1, β_2, β_3 (Eq. 1) are used for EOG elimination for the rest of the signal.

A measured EEG signal consists of the following components (see Eq. 1) [2].

$$s_m(n) = s_t(n) + \beta_1 \cdot r_v(n) + \beta_2 \cdot r_h(n) + \beta_0 \quad (1)$$

In this context, n is the current sample, $s_m(n)$ is the measured EEG for one channel, $s_t(n)$ is the true EEG without noise or offset, $r_v(n)$ is the vertically measured EOG and $r_h(n)$ is the horizontal EOG. These values can be measured directly, but β_1, β_2 as well as $s_t(n)$ and the DC-offset β_0 are unknown. A simple model for EOG and EEG interaction is as follows, with $s(n)$ the sought clean EEG with DC-offset (Eq. 2):

$$s(n) = s_t(n) + \beta_0 \quad (2)$$

The most common approach is to apply least squares estimation to the measured EEG in Eq. 1. Yet, the calculation of least squares has numerical problems due to several matrix inversions and cannot adapt after calculation.

Our idea is to implement a recursive least squares (RLS) methodology oriented on the approach in [2] in order to achieve real-time processing and adaptation.

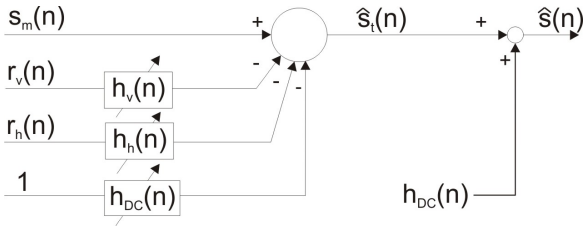

Figure 1: Adaptive filter structure

Methods

In [2] an RLS algorithm is introduced, which eliminates the influence of eye movements. The filters h_v and h_h of length M replace the parameters β_i. The described filter method is modified as can be seen in Fig. 1. The original filter structure is combined with an additional filter h_{DC}. In order to obtain the EEG with DC-offset, h_{DC} is later added to the true EEG.

For further analysis an EOG vector $r(n)$ and its filter vector $h(n)$ are introduced (see Eq. 3).

$$r(n) = \begin{pmatrix} r_v(n) \\ r_h(n) \\ 1 \end{pmatrix} \qquad h(n) = \begin{pmatrix} h_v(n) \\ h_h(n) \\ h_{DC}(n) \end{pmatrix} \quad (3)$$

The update is as follows (Eq. 4 - 7): $k(n)$ is the correction vector, $s_t(n)$ is the estimated true EEG, $R(n)^{-1}$ is the inverse of the correlation matrix.

$$k(n) = \frac{R(n-1)^{-1} \cdot r(n)}{1 + r(n)^T \cdot R(n-1)^{-1} \cdot r(n)} \quad (4)$$

$$\hat{s}_t(n) = s_m(n) - r(n)^T h(n-1) \quad (5)$$

$$h(n) = h(n-1) + k(n) \cdot \hat{s}_t(n) \quad (6)$$

$$R(n)^{-1} = R(n-1)^{-1} - k(n) r(n) R(n-1)^{-1} \quad (7)$$

The estimated EEG $\hat{s}(n)$ with DC-level (Eq. 8) is:

$$\hat{s}(n) = \hat{s}_t(n) + h_{DC}(n) \quad (8)$$

Initial values are $h(0) = 0$ and $R(0)^{-1} = \frac{1}{\sigma} I$.

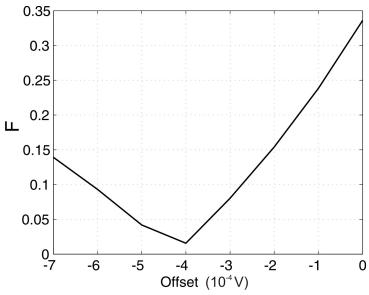

Figure 2: Estimation error for different initial DC-offsets using RLS (actual baseline $\beta_0 = -4$ x 10^{-4})

Correct parameterization of this RLS problem is crucial. In [2] a filter length of $M = 3$ and initial value $\sigma = 0.01$ are used. For our case, new parameterization was necessary. We assumed $\sigma = 10^{-5}$ with filter length $M >= 3$. This method is not sensitive to the size of M, unless M is smaller than 3 [2]. Since the estimation of the baseline showed an oscillating behaviour, a moving weighted average filter with fading memory was applied with $\epsilon = 10^{-3}$ as a forgetting factor (Eq. 9).

$$\hat{s}(n) = \hat{s}_t(n) + \epsilon \cdot h_{DC}(n) + (1 - \epsilon) \cdot h_{DC}(n-1) \quad (9)$$

In order to determine an initial baseline, a combined approach was introduced. First, the initial value for the baseline was determined with LS (calibration) and then the EEG was estimated with RLS (see Fig. 1).
A relative error (F) measurement was conducted (see Eq. 10). Lower absolute values account for better estimation.

$$F = \frac{\sum_{n=1}^{N} |\hat{s}(n) - s(n)|}{\sum_{n=1}^{N} |s(n)|} \quad (10)$$

Results

The dataset was comprised of synthetic data. The dataset consisted of a sine wave with $f = 0.01$ Hz, superimposed with Gaussian noise and simulated EOG data with values from [1].
For the use of the RLS method the initial offset had to be estimated; without calibration the offset can only be guessed. The quality of estimation depends on this initial value as can be seen in Fig. 2.
In a subsequent test, RLS and LS were applied with a previous calibration (C) period. Three minutes were taken for calibration as at least 40 eye movements are necessary [3]. It is obvious that RLS with previous calibration through LS performs better than the LS method on its own (see Tab. 1). The RLS method with calibration estimates the DC-offset more correctly than the LS method (see Fig. 3). Artifacts from eye movements are removed by both approaches.

Table 1: Values for datasets with LS approximation and RLS with calibration (3 min.)

Method	F
C+LS	0.2303
C+RLS	0.0509

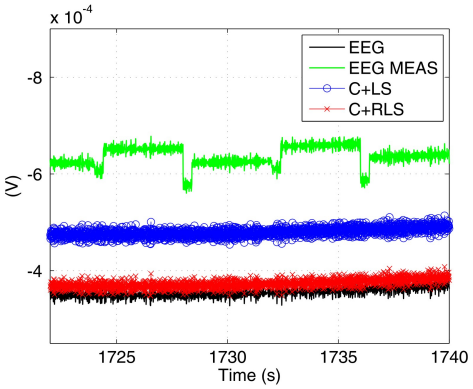

Figure 3: Comparison of LS and RLS with previous calibration (3 min.)

Discussion

The algorithm proposed in this paper offers real-time computation of eye-movement corrections sustaining the DC-offset. The RLS method performed better than LS in our simulation, but without the moving average filter it converges too slowly for practical use. Filtering of the baseline is therefore necessary. The approach with previous calibration is also promising because it can provide a more accurate initial value for the baseline.
As a result, this method can be applied for SCP recordings for neurofeedback in the future.
However, due to the limited data, further investigations have to be performed to prove this approach.

Acknowledgement

This research was funded by BMWI ZIM grant KF2561904.

Bibliography

[1] S. Berkes and K. Schellhorn, “Online ocular artefact removal for dc-eeg-signals: estimation of dc-level,” *DGBMT*, 2004.

[2] P. He, G. Wilson, and C. Russell, “Removal of ocular artifacts from electro-encephalogram by adaptive filtering.” *Medical & biological engineering & computing*, vol. 42, no. 3, pp. 407–12, 2004.

[3] R. J. Croft and R. J. Barry, “Removal of ocular artifact from the EEG: a review.” *Neurophysiologie clinique*, vol. 30, no. 1, pp. 5–19, 2000.

Biomed Tech 2013; 58 (Suppl. 1) © 2013 by Walter de Gruyter · Berlin · Boston. DOI 10.1515/bmt-2013-4164

AUTOMATIC VALIDATION AND QUALITY BASED READJUSTMENT OF MANUALLY SCORED EEG AROUSAL

Dennis Lerch[1], Thomas Penzel[2] and Reinhold Orglmeister[1]

[1]Electronics and Medical Signal Processing, TU Berlin, Germany

[2]Interdisciplinary Sleep Medicine Center, Charité - Universitätsmedizin, Germany

dennis_lerch@gmx.de

Abstract: *A knowledge of arousals during sleep is important to attain a deeper understanding regarding cardiovascular diseases. Manual scoring is time consuming and not always accurate. Automatic approaches are even worse inter alia due to inaccurate learning data. This paper presents an algorithm to improve the accuracy of manually scored data. Also a measure of quality is introduced to judge the automatically estimated results.*

Keywords: *Arousal detection, validation, quality estimation*

Introduction

An arousal is characterized by an abrupt frequency shift in the EEG for from 3 s up to 15 s ([1]). Different studies (see [2]) have shown that manually scored events differ not only among scorers, but also between analyses of one scorer of the same data. Reliable data is required to set up an algorithm which determines the arousal as closely as possible.
This paper shows an algorithm to readjust the manually scored starting time and to give a measure of its quality.

Methods

In this work, overnight polysomnographic recordings from the Daphnet-Project[1] are used. Different medical technicians scored the records, but each record was only scored once. Therefore, the following assumptions can be made:

1. The starting time of an arousal may differ from the true beginning, in some cases several seconds are possible.

2. Misclassification of non-existent arousals can occur.

$S = 446$ segments with manually scored arousals, extracted from 33 patients, are used. Each segment takes $L = 40\,\mathrm{s}$ and starts 20 s before and ends 20 s after the beginning of an arousal. According to [3], arousals are well visible in the frequency bands β_1 (16 to 24 Hz), β_2 (24 to 32 Hz) and γ (32 to 48 Hz). In total, instantaneous power of $B = 2{\cdot}3 = 6$ EEG bands (from derivation C3-A2 and C4-A1) are used.
The beginnings of arousals are detected by a threshold based algorithm. The thresholds are derived from the statistical properties of all segments.

[1]Daphnet-Project: Dynamical Analysis of Physiological Networks, EU-Project 2006-2009, Ref. 018474-2, examination of patients suffering from sleep apnoea, periodic leg movement and insomnia.

Determination of thresholds

Thresholds of power bands are used to ensure a qualitatively good data basis. The following procedure is performed for each power band b, where $1 \leq b \leq B$.
The 0.7-quantiles of the segments are determined and visualised in a histogram. A threshold $\tau_{band}\,(b)$ will be chosen to separate the two essentially visible intervals at lower and higher power. A 0.7-quantile implies that at least 70 % of all power values are less or equal than the given quantile value. Hence, no more than 30 %, or 12 s of the values of a 40 s segment, exceed the quantile value which can be caused by an arousal. Power bands for which the 0.7-quantile lies above their associated threshold will be classified as bad, meaning they are too much affected by artifacts.
Thresholds for arousal detection are empirically chosen from the histograms of the corresponding values of good power bands. The procedure is similar to the previous one. $\tau_{ar}\,(b)$ represents the found thresholds of the arousals in the power band b.

Arousal detection

The thresholds $\tau_{ar}\,(b)$ are applied to every segment in order to detect possible arousals. Unfortunately, the actual power during true arousals does not consistently exceed the threshold $\tau_{ar}\,(b)$. Therefore, threshold exceeding sections are combined to one interval if the temporal gaps are less than 2 s. Afterwards, all intervals with a duration of less than 3 s or more than 15 s are discarded. Remaining intervals, or so called blocks, must be tested if an arousal exists.
NON AROUSAL: If in all good bands of a segment no blocks exist, the segment will be marked as "No arousal occurred". $\mathbb{M}_0$ is the set of all concerning segments.
AROUSAL: An arousal in a segment will be found if at least one block in at least one good power band exists. These segments form the set $\mathbb{M}_1$. To estimate the beginning of the arousal, the median of all beginnings of blocks from all good power bands with exactly one block is determined. If only good power bands with more than one block exist, all existing blocks will be taken into consideration. But, in this case the quality of estimation is set to zero.

Quality of estimation

For a better evaluation of the estimated arousals, different quality measures will be introduced.
Quality of segments are expressed by Eq. 1

$$q_{seg.}(s) = \frac{n\_good\_band(s)}{B}, \quad (1)$$

where $1 \leq s \leq S$ and $n\_good\_band(s)$ equals the number of good power bands in segment s.

Quality of estimation as NON AROUSAL: The quality is described with $q_{non\,ar.}(s^*) = q_{seg.}(s^*)$, with $s^* \in \mathbb{M}_0$.

Quality of estimation as AROUSAL: The quality of a found arousal is the product of different quality measures (see Eq. 2).

$$q_{ar.}(s^{**}) = q_{seg.}(s^{**}) \cdot q_1(s^{**}) \cdot accuracy(s^{**}), \quad (2)$$

where $s^{**} \in \mathbb{M}_1$. $q_1(s^{**})$ is the ratio between the number of good power bands with exactly one block and the number of all good power bands within the segment s^{**}.
The $accuracy$ weighs variations of possible beginnings of arousals in different power bands. It uses the standard deviation according to Eq. 3.

$$accuracy(s^{**}) = 1 - \frac{std(block\_begin(s^{**}))}{S}. \quad (3)$$

$block\_begin$ is a vector containing all beginnings of blocks from power bands with exactly one block.

Results

The thresholds used are listed in Tab. 1. Tab. 2 shows the absolute frequencies of the qualities of the segments and of the not arousals detected. Two segments are completely unusable, and not all power bands in all segments are good enough for using. No arousals are found in 100 segments. The quality of the classification is very high. The other 364 segments contain arousals. Whereas the quality of 29 segments is $0\,\%$, that of 117 segments is $16.67\,\%$ and of 218 segments above $16.67\,\%$. A lot of segments contain only one power band with one block. The other power bands of the segments concerned contain more than one block in many cases. Therefore, these are currently not used to estimate the beginning of an arousal. This is the reason for a peak at $16.67\,\% \approx 1/6$. But a detailed investigation shows that very often blocks in different power bands exist which are located temporally close to each other. These blocks must be identified and should also be taken into consideration for estimating the beginning of an arousal. The quality $q_{is\,ar.}(s^{**})$ will rise and the peak at $16.67\,\%$ will be shifted to a higher value.

In Fig. 1, the histogram of the differences between the manually scored and the automatically detected beginnings of the arousals are visualised. A large number of automatically detected arousals are located close by the manually scored arousals. Most of the estimated beginnings lie in the interval $[-5, \ldots, 5]\,s$ and correspond very well to the expected differences, determined from earlier spot tests. This allows the conclusion that the algorithm performs well.

Table 1: Thresholds for power band quality estimation and arousal detection of used bands β_1, β_2 and γ.

threshold	$\beta_1/(\mu V)^2$	$\beta_2/(\mu V)^2$	$\gamma/(\mu V)^2$
τ_{band}	35	30	50
τ_{ar}	11	40	50

Table 2: Number of segments with qualities for segment evaluation and the detection of NON AROUSAL.

quality / %	absolute freq. of $q_{seg.}(s)$	absolute freq. of $q_{non\,ar.}(s^*)$
0.00	2	0
50.00	9	2
66.50	3	1
83.00	6	1
100. 00	445	96

Discussion

The algorithm used is well suited to estimate the beginning of arousals of manually inaccurately scored EEG data. Furthermore, a quality measure exists to judge the results. In future work, the threshold decision will be replaced by a probability based approach. Moreover, an algorithm will be developed to accurately handle power bands with multiple blocks in order to identify the most likely blocks for estimating the beginning of an arousal.

Bibliography

[1] R. B. Berry and et al., "Rules for scoring respiratory events in sleep: Update of the 2007 AASM manual," *Clinical sleep medicine*, vol. 8(5), pp. 597–619, 2012.

[2] M. H. Bonnet and et al., "The scoring of arousal in sleep: Reliability, validity and alternatives," *Journal of Clinical Sleep Medicine*, vol. 3, pp. 133 – 151, 2007.

[3] H. P. Collin, *Detection of Cortical Arousals in Sleep EEG*. PhD thesis, University of Hawaii, 2010.

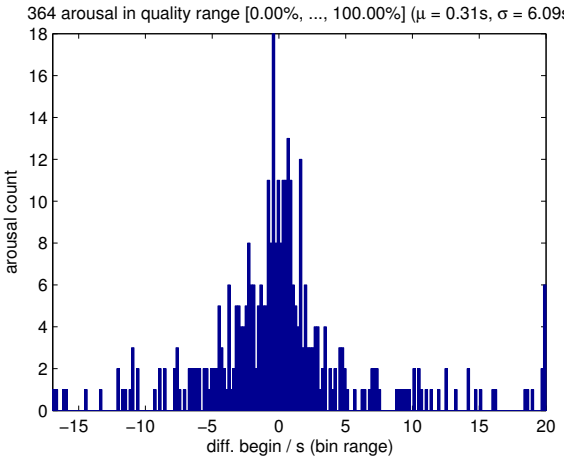

Figure 1: Differences of beginnings of arousals.

Biomed Tech 2013; 58 (Suppl. 1) © 2013 by Walter de Gruyter · Berlin · Boston. DOI 10.1515/bmt-2013-4165

Motion artefact detection in capacitively coupled EEG recording

Christof Wehrmann[1], Marlene Langer[1] and Meinhard Schilling[1]

[1]Institut für Elektrische Messtechnik und Grundlagen der Elektrotechnik, Technische Universität Braunschweig, Germany

c.wehrmann@tu-bs.de

Abstract: *An EEG helmet system is developed for mobile application of brain-computer interface (BCI). Capacitively coupled electrodes provide easy EEG measurement, with minimal preparation time. Replacing cables into a wireless connection improves mobility of the subject but leads to distorted and interrupted EEG signal by motion artefacts. Here we show the first approach to separate EEG signals and motion artefacts by use of a triaxial accelerometer and a triaxial gyroscope. The recorded data from the sensors will now be provided a basis for improvement of the EEG signal distorted by motion artefacts.*

Keywords: *capacitive eeg, capacitive electrode,* wireless interface, *motion artefacts*

Introduction

Electroencephalography (EEG) is a standard measurement application for brain activity measurement. Through an EEG measurement system a BCI can be realised, which interprets the measured brain signals and converts them into control commands [1]. Instead of resistive electrodes the capacitive electroencephalography (cEEG) uses capacitive electrodes and allows to record brain signals with very short preparation time. We developed novel helmet systems for BCI with capacitive electrodes for steering a remote controlled car [2]. Motion artefacts are the most significant contribution to be corrected measuring biosignals and BCI applications.

Methods

For measuring the EEG biosignals we use capacitive electrodes, which can be used also for capacitive electrocardiography (ECG) [3][4].

We built a helmet system with wireless connection to be able to move during EEG recording and to enable long recording sessions with maximum proband comfort.

Our capacitive electrodes are integrated in an 8 channel cEEG helmet as depicted in Fig. 1. In this configuration, we measure 7 signal electrodes against one capacitive reference electrode at the forehead [5]. The sampling rate equates 500 samples per second.

When measuring cEEG for BCI applications we often experience low signal quality due to motion artefacts. To characterize these interfering signals we integrated a triaxial-acceleration sensor and a triaxial-gyroscope in the top of the helmet.

Figure 1: Wireless 8 channel cEEG helmet system

As an example, we show an undisturbed signal of the O_Z electrode (a) and two signals with motion artefacts, by nodding and shaking the head, of O_Z (b) and O_2 (c) electrode in Fig. 2. All EEG signals are filtered by a digital 15 Hz low pass filter, for BCI applications with steady-state visual evoked potentials (SSVEP) and alpha measurements.

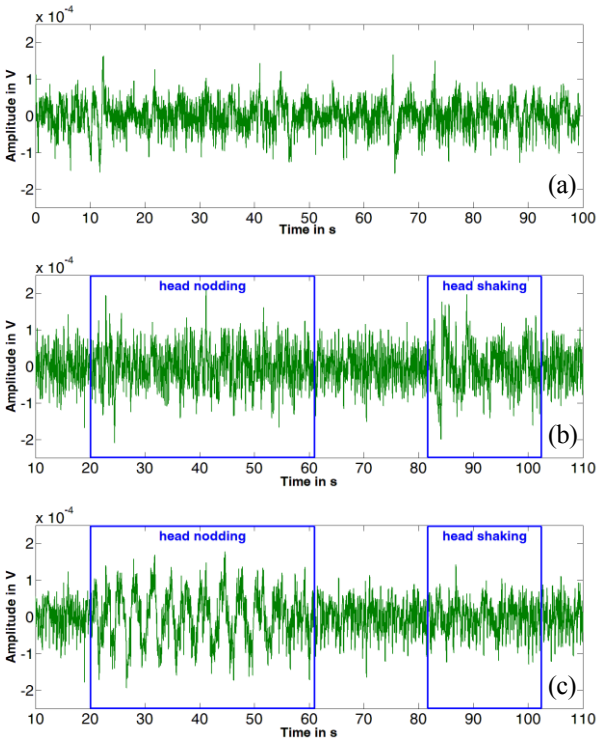

Figure 2: Comparison of undisturbed EEG signal (a) and the signal influenced by motion artefacts (b, c) for electrodes situated at the visual cortex.

Simultaneously to recording the cEEG we measured the signals of the triaxial-accelerometer and triaxial-gyroscope to analyze the sources of motion artefacts in cEEG. In Fig. 3(a) we show the x- and z-axes of the gyroscope and in Fig. 3b the x- and y-axes of acceleration sensor, during nodding and shaking the head. The signals from Fig. 2(b), 2(c) and Fig. 3 were recorded in same measurement and can be considered in direct comparison.

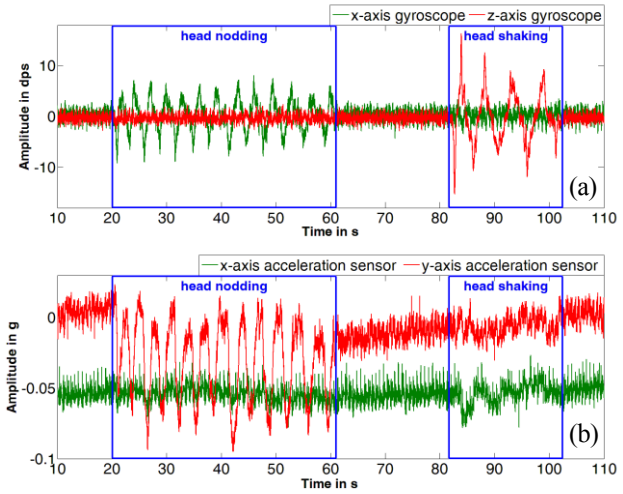

Figure 3: Signals of triaxial-gyroscope (a) and triaxial-acceleration sensor (b), while nodding and shaking the head.

The signals from the additional motion sensors can be used to detect motion artefacts. The simplest reaction on detecting motion would be to warn the user. But a cancellation of the disturbing signals from the cEEG signals would be more desirable.

Regardless, by using a digital bandpass filter we can measure an alpha wave signal, which is generated by closing the eyes. In Fig. 4 the signal of the O_1 electrode are bandpass filtered from 9 – 10,5 Hz. During 40 s – 60 s and 82 – 102 s the eyes there closed. In this time span higher signal amplitudes can be detected.

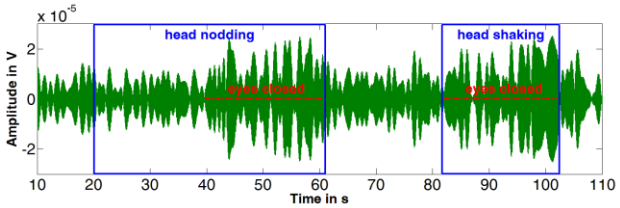

Figure 4: Bandpass filtered signal for alpha wave detection.

Results

The disturbing signals in the EEG signal are directly correlated to the motion artefacts recorded by the motion sensors. As we have shown in Fig. 2 a direct relation of motion signals to cEEG signals is not always of same signal strength in different electrodes. Depending on position and connection of the electrode and kind of movement the correlated signals show up in different capacitive electrodes with different strength. Compensation of the correlated time signals requires a more elaborate analysis which is not correctly completed.

By transfer from time domain to frequency domain by Fourier transformation, we can see that a lot of low frequency contributions are registered. Unfortunately these distortions are in the same frequency band, as the used frequencies for BCI. Therefore the appropriable compensation is required and will further improve the BCI analysis during movement. Nevertheless, as shown in Fig. 4, an alpha wave can be measured in this setup with a bandpass filter.

Due to the different information given by accelerometer and gyroscope, both sensors are required to improve the signal.

Discussion

Since we measure in a bipolar configuration, a correlated movement of the measuring electrode and the reference electrode would result in compensation. The movement of the electrodes in the helmet configure are not the same, but rather different.

A simple subtraction of the motion signals is not sufficient for the task to reduce the motion artefacts in EEG signal. The source of the electrically disturbing signal presumably is a variation in capacitance due to the motion of the head.

Bibliography

[1] J.R. Wolpaw, N. Birbaumer, D.J. McFarland, G. Pfurtscheller and T.M. Vaughan: Brain-Computer Interfaces for communication and control, *Clin. Neurophysiol.*, vol. 113, pp. 767-791, 2002

[2] Oehler M, Neumann P, Becker M, Curio G, Schilling M.: Extraction of SSVEP signals of a capacitive EEG helmet for human machine interface, *Conf Proc IEEE Eng Med Biol Soc.*,pp. 4495-4498, 2008

[3] M. Oehler, Kapazitive Elektroden zur Messung bioelektrischer Signale, *Dissertation TU Braunschweig 2009*. ISBN: 3 86664 777 8.

[4] M. Oehler, V. Ling, K. Mehlhorn and M. Schilling: A multichannel portable ECG system with capacitive sensors, *Physiol. Meas.*, vol 29, pp. 783-793, 2008

[5] M. Gerloff, M. Oehler, S. Mitschke, M. Schilling: Lightweight Capacitive 8 Channel-EEG-Helmet, *Biomed Tech Proceedings*, Volume 55, Oct. 2010

Biomed Tech 2013; 58 (Suppl. 1) © 2013 by Walter de Gruyter · Berlin · Boston. DOI 10.1515/bmt-2013-4166

SHORT-TERM EEG PATTERNS OF DRIVER DROWSINESS AND THEIR RELATION TO CRASHES

Martin Golz, David Sommer

Faculty of Computer Science, University of Applied Sciences Schmalkalden, Germany

m.golz@fh-sm.de

Abstract: *Microsleep (MS) and alpha burst (AB) patterns in the EEG of ten young drivers were detected. Their percentage within 1 min intervals was compared with independent variables of drowsiness: 1) lane tracking performance, 2) self-rating of sleepiness. In addition, the occurrence of both patterns immediately before crashes was investigated. Results offer remarkable differences. AB displays no time-since-sleep as well as no time-on-task effect. AB failed in predicting crashes. MS displays both effects and always occurred immediately before crashes.*

Keywords: *EEG, pattern recognition, drowsiness, fatigue, microsleep, driving simulation, support-vector machines*

Introduction

EEG is the most promising signal for reliable estimation of driver drowsiness due to the more or less direct assessment to the origin, the driver's brain. Various authors investigated this topic; mostly, EEG features were extracted followed by correlation analysis or analysis of variance [1 and references therein]. Up to now investigations utilizing short-term pattern recognition account to a minority. Two decades ago, Kecklund and Åkerstedt proposed AB as a marker of drowsiness [2]; recently, this concept was taken up again [3]. Alternatively, recognition of MS utilizing spectral domain, state space features, and kernel classifiers was proposed to quantify drowsiness [4]. We compare both pattern recognition methods based on the same data set and relate their output variables to two independent and broadly accepted variables in drowsiness research.

Methods

Study: was designed to investigate driving performance and subjects' behaviour under high level of monotony and sleepiness. Monotony was supported by selecting very low traffic density (no car in lane, 1 car every 3 minutes in the opponent lane; road configuration: winding two-lane road, undulating landscape). Subjects were instructed to keep in lane as best as possible and to avoid falling asleep. After returning from MS subjects were reminded that if driving performance becomes too bad the experiment would be terminated. Experiments started at 1:00 and ended at 7:40 AM, with time-since-sleep of at least 16 h and 22:40 h, respectively. Within this time 7 driving sessions (length 40 min long) were carried out.

Driving simulation: were conducted at our lab. Crashes have been defined as intervals where all 4 wheels were out of lane, no matter if the car went to the left or to the right. Incidents with 1 - 3 wheels out of lane were not included in further analysis. Lane tracking performance was measured by the standard deviation of the lateral position in lane (SdLat).

When crashes appeared an extensive soundscape as well as video scene was played to increase the emotional importance of these events. In addition drivers were warned by the observers.

Subjects: 14 healthy young volunteers (age 22.4 ± 4.1 years, range 18 - 34) with driving experience for at least 1 year participated. 1 male and 2 female quitted because of simulator sickness, 1 male quitted because of back pain.

Data acquisition: 11 biosignals (EEG: F1, F2, C3, Cz, C4, O1, O2, A1, A2, com. av. ref.; EOG: vertical, horizontal), 3 videos (driver's head & pose, driver's eyes, driving scene), 2 car related time series (steering angle, lateral position in lane) were recorded. Subjectively experienced sleepiness was rated every 4 min during driving following suggestions of [5]. Subject's response was given orally using the Karolinska Sleepiness Scale (KSS) [6].

Visual Ratings: Two operators who watched the videos performed a first judgment of ongoing MS immediately during the experiments. Typical signs of MS are prolonged eyelid closures, slow roving eye movements, head noddings, slow drifting head movements, and major driving incidents. They were often followed by abrupt reactions. Several other signs were observed, but it has been decided not to solely rely on them. In all, we have found 2,290 MS (per subject: 229 ± 67, range 138 - 363). During off-line scoring an independent and trained rater refined the time of MS occurrence. Visual ratings were only utilized to select examples of MS and Non-MS out of the continuum of the recordings.

MS detection: From EEG / EOG segments (length 6 s) of MS and Non-MS log spectral power densities (PSD) were estimated (modified periodogram) and summed in spectral bands (0.5 - 23 Hz, width 1 Hz) [4]. In addition delay-vector variances were estimated [7]. Support-Vector Machines (SVM, Gaussian kernel) were trained on these data in order to discriminate MS and Non-MS. After empirical parameter optimizations an MS detector was constructed (accuracy 97.7 ± 2.1 %). Next, the MS detector was applied consecutively to all data to detect EEG/EOG patterns which are similar to MS [8].

AB detection: 1 EEG signal (O1) was divided in overlapping segments (1 s length, 75 % overlap) [3]. If PSD culminated within extended alpha range (7 - 13 Hz) then the full width at half maximum (FWHM) was checked to be lower than two times the bandwidth of the Hamming window applied for spectral estimation. A polynomial model was fitted to the actual and to the mean PSD spectrum. Signal energy as the area above and noise energy as the

area below the fitted curve can be separated which is needed for amplitude normalization to compensate varying noise levels. Only EEG segments having signal energy within the FWHM of at least twice as large as the noise energy and having a relative peak frequency shift lower than 10 % were considered as AB [3] (Tab. 1).

Table 1: Comparison of both pattern recognition methods.

	AB detection	**MS detection**
processed signals	1 (EEG)	9 (EEG) + 2 (EOG)
temporal resolution	high (0.25 s)	high (0.1 s)
pattern duration	0.5 – 3.0 s	1.0 – 12.0 s
pattern characterization	in spectral domain	in spectral domain
pattern definition	fixed	adaptive
pattern recognition method	fixed decision rules with thresholds	nonlinear discriminant functions
signal/noise separation	exponential fit	none
output variable	pattern percentage per interval	

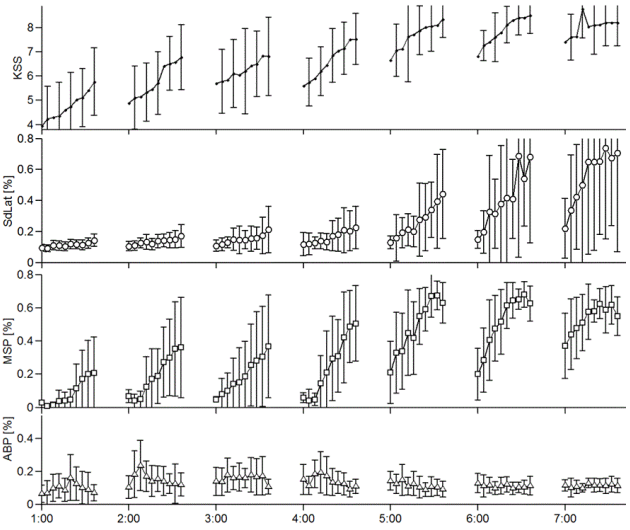

Figure 1: Mean and standard deviation of self-ratings of sleepiness on KSS, lane tracking performance SdLat, MS, and AB percentage versus time of day

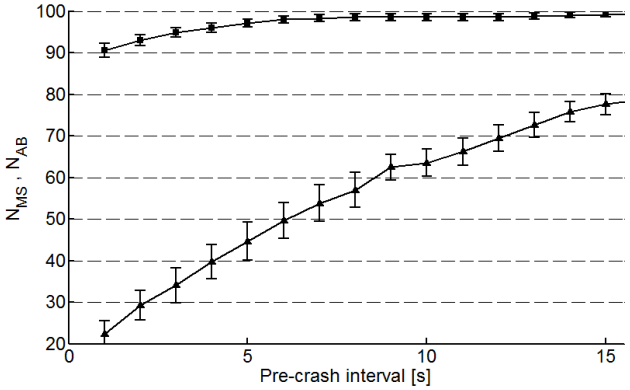

Figure 2: Mean and standard errors of pre-crash intervals containing detections of MS and AB (lower curve)

Results

Mean values of KSS, SdLat, and MS percentage correlate with time-since-sleep as well as with time-on-task, whereas AB percentage remained unchanged across the night and within driving sessions (Fig. 1). AB percentage displays larger standard deviation during the first 4 driving sessions and lower variability during the last sessions where subjects report on high self-experienced sleepiness and perform worse with regard to the lane tracking performance *SdLat*.

For each crash it was investigated if at least one MS and one AB pattern was detected within pre-crash intervals of varying length (Fig. 2). The relative number of pre-crash intervals containing MS patterns N_{MS} was always above 90 %, but not so with AB patterns. There were many crashes where no AB was detected immediately before.

Discussion

This comparative investigation of two EEG pattern recognition methodologies found remarkable differences. AB pattern appeared relatively often and with low duration. They had no significant time on task as well as no time since sleep effect. This is in contrast to the temporal development of behavioral signs of drowsiness as well as with both independent variables of drowsiness. The increase of AB percentage within the first half of the night might be interpreted as early indications of sleepiness. During the second half of the night where driver's performance dramatically deteriorated AB remained insensitive. Moreover, the results of crash analysis showed that AB seemed to arise spontaneously and not strictly related to degradations due to drowsiness. This is in contrast to [3] where an increase of AB rate from 7 min^{-1} up to 12.8 min^{-1} between the first and the last 20 min of driving was registered. An increase of AB duration from 0.62 s up to 0.665 s was reported which we could not verify.

In contrast, MS patterns turned out to be reliable forerunners of crashes. In more than 95 % of all crashes MS were found immediately before. The MS concept has the potential to establish a gold standard of drowsiness evaluation.

Bibliography

[1] Khushaba, R. et al.: Driver drowsiness classification using fuzzy-wavelet-based feature extraction, *IEEE Trans. Biomed. Eng.*, vol. 58, pp. 121–131, 2011

[2] Kecklund, G., Åkerstedt, T.: Sleepiness in long distance truck driving, *Ergonomics*, vol. 36, pp. 1007-1017, 1993

[3] Simon, M., Schmidt, E. et al.: EEG alpha spindle measures as indicators of driver fatigue under real traffic, *J Clin. Neurophysiol.*, vol. 122, pp. 1168-1178, 2011

[4] Golz, M., Sommer, D. et al.: Feature fusion for the detection of microsleep events, *J VLSI Signal Proc. Syst.*, vol. 49, pp. 329-342, 2007

[5] Ingre, M., Åkerstedt, T. et al.: Subjective sleepiness, simulated driving performance and blink duration. *J. Sleep Res.*, vol. 15, pp. 47-53, 2006

[6] Åkerstedt, T.: Subjective & objective sleepiness in the active individual. *Int J Neurosci*, vol. 52, pp. 29-37, 1990

[7] Gautama, T., Mandic, D., Van Hulle, M.: Novel method for determining the nature of time series, *IEEE Trans. Biomed. Eng.*, vol. 51, pp. 728–736, 2004

[8] Golz, M., Sommer, D. et al.: Microsleep episodes and related crashes during overnight driving simulations. *Proc. 6th Int. Sympos. Driver Assess.*, pp. 39-45, 2009

Biomed Tech 2013; 58 (Suppl. 1) © 2013 by Walter de Gruyter · Berlin · Boston. DOI 10.1515/bmt-2013-4167

A NEW NORMALISED SHORT TIME PDC FOR DYNAMIC COUPLING ANALYSES

Adochiei F[1], Schulz S[2], Edu I[2], Costin H[3], Voss A[2]

[1] The Faculty of Electronics, Telecommunications and Information Technology, Gheorghe Asachi Technical University Iasi, Romania
[2] Department of Medical Engineering and Biotechnology, University of Applied Sciences, Jena, Germany
[3] Faculty of Medical Bioengineering, University of Medicine and Pharmacy, Iasi, Romania

andreas.voss@fh-jena.de

Abstract: *Partial Directed Coherence (PDC) method and its extensions proved to be useful tools in analysing couplings in multivariate dynamic systems. We introduced the normalised short time PDC method (NST-PDC), to investigate the dynamic behaviour of couplings. First simulated signals obtained from coupled oscillators were analysed and information about the dynamical behaviour of the virtual system achieved. Then, as a first preliminary test applying the NST-PDC method, we observed significant ($p<0.05$) coupling dynamics differences in pregnant woman with hypertensive disorders, by comparing patients with preeclampsia and chronic hypertension. The NST-PDC is applicable for nonstationary time series, detects dynamical changes of coupling and might be usable for the analysis of time dependent cardiovascular couplings.*

Keywords: *Short Time Partial Directed Coherence, coupling analyses, cardiovascular coupling*

Introduction

In complex physiological systems linear and nonlinear time series analysis approaches are of increasing interest. In addition there is more and more evidence about the importance of investigating the dynamics of the couplings. Linear methods favour the frequency domain representation of biological signals (characterization of connectivity between specific oscillatory components) while nonlinear methods study complex signal interactions. Partial directed coherence (PDC) method [1] is among the most applied linear approaches in the frequency domain. PDC is used to acquire and evaluate couplings, due to its capability to detect direct and indirect causal information transfers between signals in multivariate dynamic systems. Taking into consideration that PDC method presupposes the stationarity of signals in the time interval nonstationary signal analysis applications cannot be performed. Further on, we cannot achieve information about the systems' coupling dynamics. A number of solutions have been suggested for the problem of time-varying directional interactions analysis. Milde et al. [2] introduced a time-variant version of PDC that avoids misinterpretations in heart rate variability analyses and quantifies the partial correlative interaction properties between respiratory movements and respiratory sinus arrhythmia. The objective of this study was to introduce a new time frequency approach, the Normalized Short Time PDC (NSTPDC), in order to assess significant coupling dynamics information. First we carried out different tests with simulated signals from an ideal system of coupled oscillators. Then, as a first and preliminary medical approach we investigated the coupling dynamics between pulse intervals (PI) and systolic blood pressure time series in pregnant women with different hypertensive disorders.

Methods

The PDC based on an *m*-dimensional multichannel autoregressive model (MAR) is capable to detect couplings in multivariate dynamic systems. Based on the Fourier transformation of the coefficient matrix *A(f)*, the PDC is calculated from the two processes X_j and X_i [3].
The absolute value of the *tv*PDC was defined by Baccala et al. [1] (Eq. 1).

$$\pi_{ij}(z) \overset{\Delta}{=} \frac{A_{ij}(n,f)}{\sqrt{a_j^H(n,f)a_j(n,f)}} \qquad (1)$$

where $A_j(n,f)$ is the j^{th} column of the matrix A(n,f) with n as window number and f as frequency. The normalization parameters achieved after applying the PDC normalization are shown in Eq. 2.

$$0 \le \left|\pi_{ij}(f)\right|^2 \le 1, \quad \sum_{i=1}^{m}\left|\pi_{ij}(f)\right|^2 = 1 \qquad (2)$$

for all $1 \le j \le m$. Values between 0 and 1 provide information about the presence and strength of causal coupling between the two time series X_i and X_j as a function of frequency f [1, 4]. We implemented the new method NSTPDC in order to assess the coupling direction and strength between the two processes. A coupling factor CF is calculated as the mean value of X_j coupled with X_i divided by the mean value of X_i coupled with X_j. We normalized our results to a specific set of values leading to the normalized factor NF={-2,-1,0,1,2} (Eq. 3). The values {-2} and {2} represent a strong unidirectional coupling (increased absolute values means increased coupling strength) while {-1} and {1} denotes a bidirectional coupling and the master signal. Finally a value {0} means that there is either an equal influence for both directions or no coupling at all. The NSTPDC was achieved by means of a short time implementation with a Hamming window of 300 samples length and 50 samples overlap.
For simulations of time series we used the Wolfram Demonstrations Project, "Coupled Oscillators" [5]. We

considered two simulated signals (Fig. 1a) from an idealized system with two oscillators coupled together by a third one. After applying the NSTPDC method we observed that the first signal is the driving one (Fig. 1b). In the second simulation (Fig. 1c), we used the same signals, but the coupling was changed after 800 samples. After this change the second signal became the master signal and the first signal the slave signal (Fig. 1d).

$$a = mean \quad PDC(X_i - X_j)$$
$$b = mean \quad PDC(X_j - X_i)$$
$$Max(a,b)$$

$$NF = \begin{cases} 2, & if\,(Max = a \quad and \quad a/b > 5) \\ 1, & if\,(Max = a \quad and \quad 2 < a/b \le 5) \\ 0 & if\,(Max = a \quad and \quad 0 \le a/b \le 2) \end{cases} \qquad (3)$$

$$NF = \begin{cases} -2, & if\,(Max = b \quad and \quad b/a > 5) \\ -1, & if\,(Max = b \quad and \quad 2 < b/a \le 5) \\ 0 & if\,(Max = b \quad and \quad 0 \le b/a \le 2) \end{cases}$$

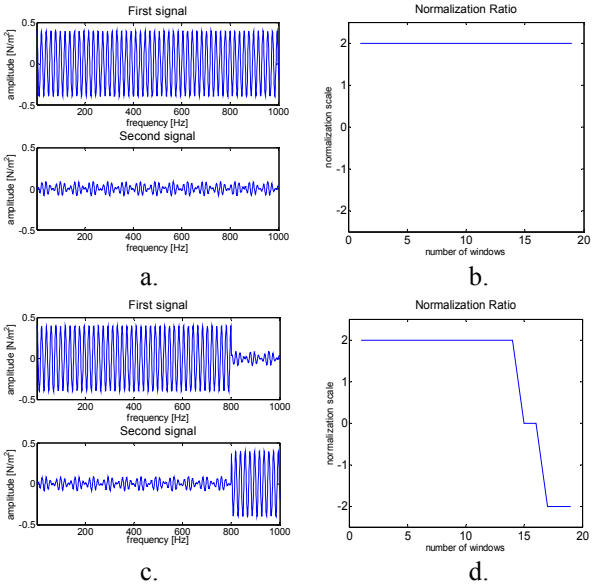

Figure 1: Simulation of different couplings (left side: input signals; right side: coupling level diagrams)

Next we generated couplings between the same signals but with different levels of superimposed noise (1%-10% of the signal's amplitude). If the noise amplitude was greater than 10% the couplings were no longer visible.
After these simulations we proved if NSTPDC would be able to find changes of couplings within cardiovascular systems. Here, we investigated the dynamic coupling between time series of beat-to-beat intervals (BBI) and systolic blood pressure (SBP) from 10 pregnant women with hypertensive disorders (5 with chronic hypertension - CH, mean age 31.2 years and 5 with preeclampsia – PE, mean age 26.8 years). The investigation conforms to the principles outlined in the Declaration of Helsinki. Local ethics committee approval and the informed consent of all subjects were provided. We calculated the mean value and dynamics standard deviation (DSD) of the NF from NSTPDC. For discrimination between the two groups we used the Mann-Whitney-U-test with $p<0.05$ as significance level.

Results

The simulation study showed that changes in coupling could be clearly detected by NSTPDC. However, if the noise level exceeds 10% of the input signals a coupling cannot be observed. In the preliminary medical application more dynamic changes of coupling BBI -> SBP were observed in CH (higher DSD, $p<0.039$) than in PE while the SBP->BBI coupling was not significant but a trend towards a higher dynamics in PE is noticeable.

Discussion

The NSTPDC method is an improvement of the standard PDC. It enables us to investigate signals with nonstationary properties and allows the detailed investigation of coupling changes. In a simulation study that was only briefly described the change of coupling could be clearly demonstrated. However, the precision is a compromise of window length and coupling strength. This is part of an ongoing study. In the preliminary medical study we could show for the first time that the dynamics of coupling changes BBI -> SBP is much higher in CH than in PE. That means that in PE there is a much more constant drive from BBI to SBP. We speculate that this could be caused by a higher mental stress. However, this has to be validated by enrolling a much higher number of patients.
In conclusion, the new proposed method NSTPDC is able to estimate couplings and their directions in nonstationary time series, it performs dynamic coupling analysis and might be useful in characterizing cardiovascular couplings.

Acknowledgement

This paper was realised with the support of POSDRU CUANTUMDOC ID79407 project funded by the European Social Found and Romanian Government.

Bibliography

[1] L. A. Baccala and K. Sameshima, "Partial directed coherence: a new concept in neural structure determination.," *Biol. Cybern., 84, 463-474.*

[2] T. Milde, K. Schwab, M. Walther, M. Eiselt, C. Schelenz, A. Voss, and H. Witte, "Time-variant partial directed coherence in analysis of the cardiovascular system. A methodological study," *Physiol Meas,* vol. 32, pp. 1787-805, Nov 2011.

[3] S. Schulz, F.-C. Adochiei, I.-R. Edu, P. C. S. Rico, C. Hariton, K.-J. Bär, and V. Andreas, "Cardiovascular and cardiorespiratory non-linear coupling analyses – a review," *Philos Transact A Math Phys Eng Sci. (in press),* 2013.

[4] L. Faes and G. Nollo, "Extended causal modeling to assess Partial Directed Coherence in multiple time series with significant instantaneous interactions," *Biol Cybern,* vol. 103, pp. 387-400, Nov 2010.

[5] H.-J. Domke. (2011). *http://demonstrations.wolfram.com/DynamicsOfCoupledPendulums/.*

Biomed Tech 2013; 58 (Suppl. 1) © 2013 by Walter de Gruyter · Berlin · Boston. DOI 10.1515/bmt-2013-4168

GENERATING BIATRIAL LOCAL ACTIVATION TIME MAPS USING THE NON-LINEAR ENERGY OPERATOR REVEALS ARRHYTHMIA

Oesterlein, T G[1], Luik, A[2], Schmitt, C[2], Dössel, O[1]

[1]Institute of Biomedical Engineering, Karlsruhe Institute of Technology (KIT), Germany
[2]Städtisches Klinikum Karlsruhe, Karlsruhe, Germany

tobias.oesterlein@kit.edu

Abstract: *Simultaneous biatrial electroanatomical mapping was performed in a 54 year old woman using two 64-electrode basket catheters. Local activation time (LAT) maps were extracted retrospectively for single atrial excitations during sinus rhythm using the non-linear energy operator (NLEO). Considering both ampltiude and frequency information, the NLEO has shown to be a reliable estimator for the LAT. This paper presents an approach for creating biatrial LAT maps using the NLEO for single atrial excitations. The varying propagation pattern of individual beats reveals the presence and location of supraventricular extrasystoles.*

Keywords: *local activation time map, intracardiac signal processing, nonlinear energy operator, supraventricular extra systole*

Introduction

Electroanatomical mapping is an important tool in interventional therapy of atrial arrhythmia. The LAT provides information about the propagation of the electrical excitation during the arrhythmia. Mapping can be performed sequentially on a point-by-point basis, but only if rhythm and propagation pattern are stable. Multielectrode basket catheters, however, allow parallel mapping of a complete atrium for individual beats.
Biatrial basket mapping has been demonstrated to be feasible for mapping premature atrial complexes [1]. More recent work has drawn attention to studies which aim at identifying rotors and focal sources that might be responsible for atrial fibrillation [2].
Since these catheters record up to 128 signals in biatrial mapping, computer aided analysis and visualization provides an essential tool for the physician. In this paper the non-linear energy operator (NLEO) is applied as a new method to generate LAT maps for single atrial excitations. The NLEO has already been demonstrated as a useful tool in analysis of complex fractionated atrial electrograms [3] and for wavefront analysis for circular catheters [4].

Methods

Clinical data from a 54 year old female suffering from paroxysmal atrial fibrillation was analyzed retrospectively. A standard 12-lead ECG was recorded. Using an impedance based electroanatomical mapping system (Ensite Velocity, St. Jude Medical), 126 intracardiac electrograms were acquired simultaneously from two 64-electrode basket catheters (Constellation, Boston Scientific) in each atrium and a coronary sinus (CS) catheter. The electrophysiological mapping system was used to generate a 3D surface of the heart geometry.

Unipolar electrograms from 126 basket catheter electrodes were exported for offline analysis. Bipolar electrograms were computed for all neighboring electrodes on a spline. The signals were filtered using second order butterworth filters (highpass f_c=30 Hz, lowpass f_c=150 Hz). The geometrical center point between both electordes was projected onto the map surface and defined as point of measurement. The nonlinear energy E_j at each timestep j from signal x was computed as

$$E_j = x_j^2 - x_{j+1}x_{j-1}, \tag{1}$$

and the resulting NLEO signal was lowpass filtered at 24 Hz [3]. The filtered signal was interpolated on the whole atrium and the time of its maximum value used as LAT. Areas more than 10 mm away from a measurement point were excluded from visualization. Since each single beat is analyzed, no referencing to the CS signal was necessary.
Signals from two atrial activations during sinus rhythm (SR) were selected for demonstration, the corresponding activations are numbered Fig. 1. For each activation, the signal ±250 ms around the activation was analyzed automatically.

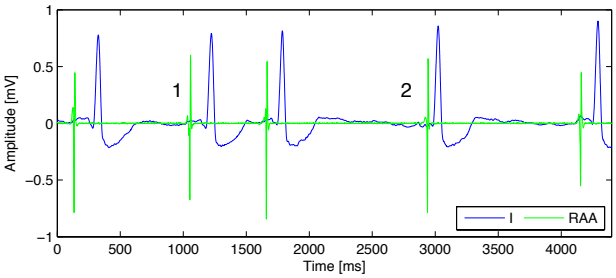

Figure 1: Continuous electrograms of lead I and an intracardial electrogram from the lateral RA appandage. The two numbered beats were chosen for demonstration.

Results

Two intracardiac signals from the right atrium (RA) and left atrium (LA) are depicted in Fig. 2. The electrogram RA was

recorded at the lateral RA appendage, signal LA at the high anterior wall. The LAT detected by the NLEO is marked with a red line. The LAT of signal RA was earlier than the LAT of signal LA during beat 1 and later in beat 2. All times were referenced to the first detected activation.

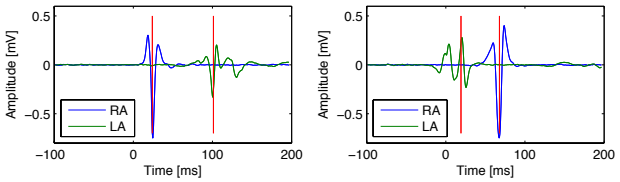

Figure 2: Representative electrograms for beat 1 (left) and beat 2 (right). Intracardiac signals were measured at the lateral RA appendage and the high anterior wall in the LA.

Reconstructed LAT maps can be found in Fig. 3. The excitation for beat 1 started close to the sinus node and propagated down the RA. The earliest activation on the left atrium was close to Bachmann's bundle. Activation for beat 2 spread from the high anterior wall of the LA. Activation of the RA progressed downwards.

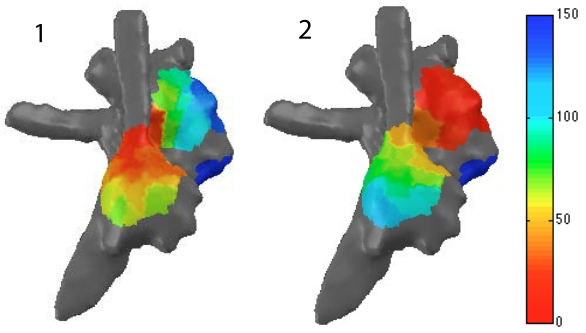

Figure 3: LAT maps determined by the NLEO-based method for beats 1 and 2 in RAO view. Early activations are colored red and late activations blue, time given in ms. Earliest point of activation was near the sinus node / superior vena cava for beat 1 and near high anterior wall in beat 2.

Discussion

Both maps show consistent activation patterns without visible artifacts or prominent zones of slow conduction. The activation pattern of beat 1 was consistent with SR, whereas the activation for beat 2 corresponded with a supraventricular extra systole located near the LA roof.
The total depolarization time was approximatelly 125 ms for both beats, which was slightly higher than the literature value of <100 ms [5]. The latest LAT close to the mitral valve was found to be a ventricular artifact in both beats.
Previous work has demonstrated the feasibility of algorithms to detect the location of atrial ectopic foci based on P-wave morphology [6]. However, existing ablation lines in the atria might alter the path of excitation, lead to unexpected activation patterns and thus present a drawback of these methods. Direct measurement of LAT maps provides a fast and reliable way in these situations.
The excitation pattern in SR could clearly be distinguished from a SVES. However, detailed localization of the SVES was not possible since the electrode positioning was not optimized for this purpose.
Since this map could be generated for every single beat, the excitation wavefront could be monitored for every beat individually and continuously. This could help to automatically localize and statistically evaluate ectopic foci which are known to be located also outside pulmonary veins [1]. A reliable high detail LAT map also allows to determine local conduction velocity. Differences depending on wave direction or stimulation parameters can thus be computed and visualized during intervention.

Acknowledgement

The work of Tobias Oesterlein is sponsored by the German Research Foundation (DO637/14-1).

Bibliography

[1] C. Schmitt *et al.*, "Biatrial multisite mapping of atrial premature complexes triggering onset of atrial fibrillation," *Am J Cardiol*, vol. 89, no. 12, pp. 1381–1387, 2002.

[2] S. M. Narayan *et al.*, "Treatment of atrial fibrillation by the ablation of localized sources: Confirm (conventional ablation for atrial fibrillation with or without focal impulse and rotor modulation) trial," *J Am Coll Cardiol*, vol. 60, no. 7, pp. 628–36, 2012.

[3] C. Schilling *et al.*, "Non-linear energy operator for the analysis of intracardial electrograms," *IFMBE Proceedings*, vol. 25, no. 4, pp. 872–875, 2009.

[4] F. M. Weber *et al.*, "Wave-direction and conduction-velocity analysis from intracardiac electrograms–a single-shot technique." *IEEE TBME*, vol. 57, no. 10, pp. 2397–2401, 2010.

[5] C. Schneider, *Das EPU-Labor*, 1st ed. Steinkopf Verlag, 2005.

[6] P. Kistler *et al.*, "P-wave morphology in focal atrial tachycardia: development of an algorithm to predict the anatomic site of origin," *J Am Coll Cardiol*, vol. 48, no. 5, pp. 1010–1017, 2006.

Biomed Tech 2013; 58 (Suppl. 1) © 2013 by Walter de Gruyter · Berlin · Boston. DOI 10.1515/bmt-2013-4169

A GENERAL APPROACH FOR DYNAMIC MODELING OF PHYSIOLOGICAL TIME SERIES

Pfeifer M, Lenis G, Dössel O

Institute of Biomedical Engineering, Karlsruhe Institute of Technology (KIT), Germany

publications@ibt.kit.edu

Abstract: *Dynamic modeling of physiological time series represents an auspicious approach in the arena of biomedical signal processing. This study illustrates a new methodology for identifying dynamic models that is based on stationary stochastic processes. The method is applied to time series extracted from the ECG. Simulations of the gained models yield physiologically plausible results .*

Keywords: *Time Series, Modeling, State Space, Heart Rate, ARMA*

Introduction

Time series (TS) analysis represents a fundamental discipline of scientific and clinical practice in biomedical signal processing. A very sophisticated subarea is the investigation of TS including cardio-electric information such as heart rate dynamics and ventricular repolarization [1].

The majority of methods analyzing electrophysiological information have been primarily directed towards static parameters or dynamic models considering only brief TS extracts (<500 elements). In contrast, this study presents a holistic dynamic approach of modeling physiological TS. Thereby, the methods can be applied to a wide context of biomedical applications.

Methods

Autoregressive-moving average (ARMA) processes are capable of modeling any stationary TS at arbitrary accuracy. However, regarding physiological TS, the hypothesis of stationarity usually has to be rejected by means of statistical tests. Applying a finite number of suitable filter operations provides modified TS which reasonably can be expected to be stationary. The filtered TS are modeled using ARMA processes which are subsequently transferred into a state space representation. A subtle extension of the space state model enables an elimination of the filtering influence and therefore provides a dynamic model for the original TS.

Stationarity and Filtering: Evaluating stationarity for measured TS is no trivial procedure. However, in many cases a visual analysis of the TS plot permits initial tendencies towards stationarity properties. As an example, a linear trend provides clear evidence on instationarity. A more tangible approach is based on the analysis of the sample autocorrelation function (ACF), denoted $r(k)$ [2]. A necessary condition for stationarity is $r(k) \rightarrow 0$ for $k \rightarrow N$ where N represents the number of elements of the TS. In physiological TS the decay of $r(k)$ is typically performed very slowly with respect to k, which is a distinct indication for instationarity. A differencing filter embodies an appropriate approach for eliminating this type of instationarity. Each two consecutive elements are subtracted yielding a filtered TS with improved stationarity properties. Differentiating d times consequently supplies a TS that is sufficiently stationary to be modeled by an ARMA process.

ARMA-Modeling: ARMA(p,q) models provide a parsimonious description of a stationary stochastic process. They are characterized by a Gaussian white noise process $\epsilon_k \sim N(0, \sigma_\epsilon^2)$ and two summations, one for the AR and the second for the MA part:

$$Y_k = \sum_{m=1}^{p} a_m Y_{k-m} + \epsilon_k + \sum_{n=1}^{q} b_n \epsilon_{k-n}. \qquad (1)$$

In order to identify a model for a given TS the orders (p, q), the parameters (a_m, b_n) and the noise variance (σ_ϵ^2) must be investigated.

Determining the model orders faces a trade off between a strong adaption to statistical properties of the TS and the principle of parsimony. For an initial appraisal the ACF and the partial ACF (PACF) are evaluated and maximal orders p_{max} and q_{max} are estimated. Conciliating the above mentioned trade off, a minimization of the Akaike Information Criterion (AIC) then yields the orders p and q [2]:

$$\mathrm{AIC} = \log \sigma_r^2 + \frac{2(p+q)}{N}. \qquad (2)$$

σ_r^2 is the residual variance between TS and an estimated ARMA(p,q) model and therefore a measure of adaption. The second addend penalizes high model orders.

Deploying the specified orders, the parameters a_m and b_n are estimated based on the prediction-error method. In a last step, the noise variance σ_ϵ^2 must be determined. During a literature research, no quantitative relation between σ_ϵ^2 and the variance of Y_k, denoted σ_Y^2, could be found. However, empirical tests suggested a linear dependence between the two variances. Based on system-theoretical fundamentals, a formula was derived quantifying the linear dependence:

$$\sigma_Y^2 = \int_{-f/2}^{f/2} \left| \frac{1 + \sum_{n=1}^{q} b_n \mathrm{e}^{-j2\pi fn}}{1 - \sum_{m=1}^{p} a_m \mathrm{e}^{-j2\pi fm}} \right|^2 \mathrm{d}f \cdot \sigma_\epsilon^2. \qquad (3)$$

ARMA Model Diagnostics: Diagnostics represent a crucial step of TS modeling [2]. The quality of adaption of a model is assessed based on a comparison between statistical properties of the TS and the model:

- Visual comparison between the theoretical ACF of the ARMA model and the empirical ACF of the TS
- Assessing whether the residuals represent a realization of a white noise process

If the adaption is appraised to be not sufficient, a new model with increased orders has to be identified.

ARMA and ARIMA Models in State Space: By introducing r=max(p, q) and setting a_m and c_n to zero for m=p+1,...,r and n=q+1,...,r a transformation into a companion state space realization is viable. Applying a slight extension eliminates the differencing influence of the initial filtering by contributing d integrating operations. For d=1 the model is given by:

$$\vec{x}_{k+1} = \begin{bmatrix} 0 & 0 & \dots & 0 & -a_r & 0 \\ 1 & 0 & \dots & 0 & -a_{r-1} & 0 \\ 0 & 1 & \dots & 0 & -a_{r-2} & 0 \\ \vdots & \vdots & & \vdots & \vdots & \vdots \\ 0 & 0 & \dots & 1 & -a_1 & 0 \\ 0 & 0 & \dots & 0 & 1 & 1 \end{bmatrix} \vec{x}_k + \begin{bmatrix} b_r - a_r \\ b_{r-1} - a_{r-1} \\ b_{r-2} - a_{r-2} \\ \vdots \\ b_1 - a_1 \\ 0 \end{bmatrix} \epsilon_k \tag{4}$$

$$Y_k = \begin{bmatrix} 0 & 0 & 0 & \dots & 0 & 1 & 1 \end{bmatrix} \vec{x}_k + \epsilon_k. \tag{5}$$

Formulas (4) and (5) represent a so-called autoregressive integrated moving average (ARIMA) process.

Results

Based on a measured ECG, a RR interval TS containing 2954 elements was constructed. Using this TS the presented methodology is now illustrated. Since the ACF of the TS shows a slow decay, the TS needs to be filtered. The resultant TS represents values of ΔRR and is sufficiently stationary to be modeled with an ARMA process (d=1). Analyzing the ACF and PACF yields the maximum orders $(p_{max}, q_{max}) = (5, 5)$. Applying this, the AIC is minimized for $(p, q) = (1, 4)$ which yields the model:

$$Y_k = 0.9Y_{k-1} + \epsilon_k - 1.1\epsilon_{k-1} + 0.2\epsilon_{k-2} - 0.1\epsilon_{k-4}. \tag{6}$$

For descriptive representation, parameter values are rounded to the first decimal place. Inverse application of (3) yields an input noise variance of $\sigma_\epsilon^2 = 433.5(\text{ms})^2$. Conducting diagnostics raises no doubts on the validity of the model. By using r=4 and d=1 the ARMA process is transformed into ARIMA state space representation. For validating the gained model, the subsequent illustrations depict model simulation results (red). A simulation is accomplished by simply applying a realization of the input noise process to the model. For comparison, the measured TS (blue) and the simulation results of an identified (p, q, d)=$(20, 20, 1)$ model (green) are also presented. It is important to note that the objective is not to approximate the measured TS, but to share its dynamics as exact as possible. Fig. 1 suggests that both models provide a suitable reproduction of the original ΔRR dynamics. Recalling formula (3), a correct reproduction of the ΔRR variance by the models is ensured. Fig. 2 confirms the ARIMA(1,4,1) model to represent a suitable description for the RR interval dynamics. However, the ARIMA(20,20,1) model tries to assimilate inaccuracies originating from the empirical ACF/PACF during the modeling procedure. Due to the integrating behavior of the ARIMA models these minor deficiencies will lead to physiologically implausible results.

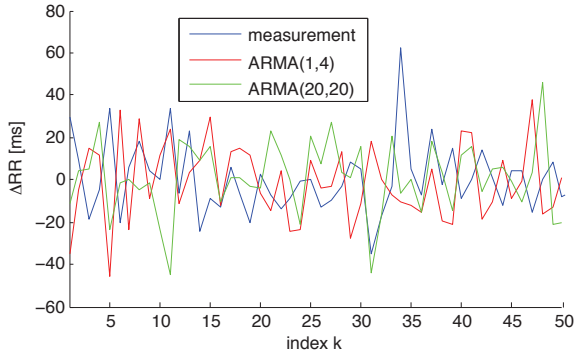

Figure 1: TS of 50 measured and simulated ΔRR intervals.

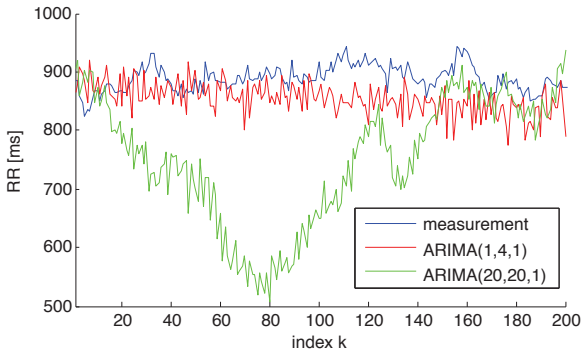

Figure 2: TS of 200 measured and simulated RR intervals.

Discussion

The presented methodology allows a versatile dynamic modeling of physiological TS only under the restriction of inaccuracies when regarding finite TS. Simulations yielded plausible results for parsimonious models. However, it is necessary to be cautious when simulating extensive models or long periods of time. Due to the integration of a power signal, the ARIMA models generate TS with variances increasing over time. The introduced models provide an enormous amount of system characteristics to be analyzed. As an example, the eigenvalues of the system matrix in formula (4) involve direct significance to dynamic properties of the generating physiological process. This information could be applied on medical classification studies concerning cardiac disease or drug safety.

Bibliography

[1] K. Kotani *et al.*, "Model for complex heart rate dynamics in health and diseases," *Physical Review E*, vol. 72, no. 4, 2005.

[2] J. D. Hamilton, *Time Series Analysis*, vol. 2. Cambridge University Press, 1994.

Biomed Tech 2013; 58 (Suppl. 1) © 2013 by Walter de Gruyter · Berlin · Boston. DOI 10.1515/bmt-2013-4170

Quantification of heart beat nonstationarities by nonparametric segmentation

Maik Riedl[1], Sabrina Camargo[1], Celia Anteneodo[2,3], Jürgen Kurths[1,4,5], Niels Wessel[1]

[1]Department of Physics, Humboldt-Universität zu Berlin, Germany

[2]Department of Physics, PUC-Rio, Brazil
[3]National Institute of Science and Technology for Complex Systems, Rio de Janeiro, Brazil

[4]Potsdam Institute for Climate Impact Research, Germany
[3]Institute for Complex Systems and Mathematical Biology, University of Aberdeen, United Kingdom

Maik.riedl@physik.hu-berlin.de

Abstract: *The standard parameter of heart rate variability (HRV) requires weak stationarity. We perform a nonparametric segmentation to HRV data of congestive heart failure patients as well as young and elderly healthy subjects where the signal is split into stationary epochs. By finding stationary segments we are able to quantify the nonstationarity by means of statistical values of segment length and jump size. We found high correlations between the measures of nonstationarity and standard values of HRV and a connection to results of detrended fluctuation analysis. The segmentation applied to heart rate time series detects aging and pathological conditions effects on the nonstationary behaviour of the analyzed groups, promising to contribute in complexity analysis and providing risk stratification measures.*

Keywords: *Heart rate variability, nonstationarity, segmentation*

Introduction

It has been a long time since studies on heart rate variability (HRV) have become as popular as the many devices available to record the cardiac activity [1]. As reported in literature, several diseases, as myocardial infarction, and diabetic neuropathy, point to a connection between healthiness and heart rate complexity. Also, the effects of aging are known to present higher HRV in younger individuals, compared to elderly ones [1]. As a standard tool of HRV analysis, the spectral analysis relies on the assumption of weak stationarity, where the mean value is constant and the covariance is only dependent on a time shift, but even in controlled environments, it is questionable whether the efficiency of such control ensures these conditions. The idea of the segmentation applied to time series is to provide patches of the signal where stationarity is verified. Instead of testing only the difference for the mean [2], we perform a nonparametric segmentation [3], taking into account the whole distribution, with all moments, especially mean and variance. We also use the known amplitude-frequency coupling of the dominant short-term oscillation [4], the respiratory sinus-arrhythmia, which connects the changes in the variance with the time-dependent covariance, implying nonstationarity.

Methods

For analysis, we consider 24 hours measurements of the electrocardiogram of three groups consisting of 15 young (YH; 11 females, 4 males, age 31±6 years) and 18 elderly subjects (EH; 11 males, 7 females, age 50±7 years), and 15 patients suffering from congestive heart failure (CHF; 11 males, 4 females, age 56±11 years) [5,6]. The series of time intervals between consecutive heart beats, the beat-to-beat intervals, are extracted from the electrocardiograms. All resultant signals were filtered in order to avoid ectopic beats [7].

After that these time series are segmented as follows: given a segment of a time series, a sliding pointer is moved in order to compare the two fragments, on the left (L) and the right (R) side of the pointer i. Then one selects the position i_{max} that maximizes the normalized Kolmogorov-Smirnov (KS) statistics:

$$D_i = D_{KS}\left(1/n_L + 1/n_R\right)^{-1/2} \qquad (1)$$

where D_{KS} is the distance between the cumulative distributions of the samples in the left and the right fragment. After determining the position i_{max}, one checks the statistical significance (at a chosen significance level α=0.05) of a potentially relevant cut at i_{max} by comparison with the result that would be obtained for a random sequence. The critical value is given by

$$D_{crit}^{\max}(n) = a(\ln n - b)^c \qquad (2)$$

where (a, b, c) is (1.52, 1.80, 0.14) in our case. The potential cut ticks the first stage if D^{max} exceeds its critical value for the selected significance level. If each resulting segment is greater than a defined minimum L_0, then the pointer is set and the procedure is recursively applied starting from the left patches until no patch is segmented. See Ref.[3] for further details. We performed the KS-segmentation with L_0=30 sample points in correspondence to the defined higher edge frequency of the very low frequency (VLF) band of heart rate with 0.03 Hz [1] providing at least a half period of this frequency in each segment.

Results

To quantify the nonstationarity, we obtain statistical values of the segmentation, which include not only segment length and jump size but also more sophisticated ones like

the number of segments greater than 300, $L_{>300}$, and $\%\mu_{50}$ (Fig. 1). $L_{>300}$ corresponds to approximately 5 min, the shortest required segment length of HRV analysis and $\%\mu_{50}$ reflects the percentage of differences of the mean of two consecutive segments $|\mu_{i+1}- \mu_i|>50$ms in an analogy to the standard HRV measure pNN50, the percentage of consecutive RR intervals differing by more than 50ms [1].

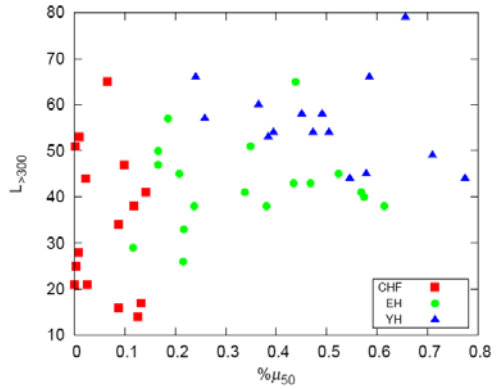

Figure 1: $L_{>300}$ and $\%\mu_{50}$ in the three groups

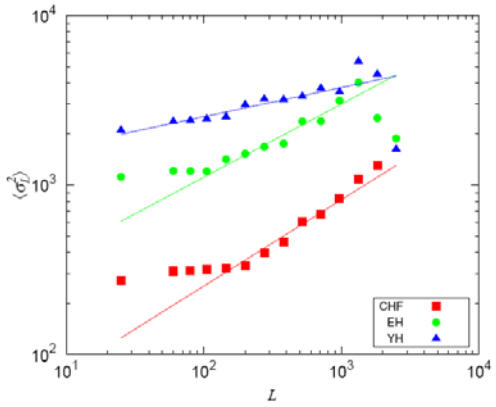

Figure 2 Mean variance of the segments of given segments length. The scaling exponents are indicated by solid lines (CHF:0.6, EH:0.4, and YH:0.2).

We found high positive correlations of about 0.9 between %μ50 and the overall standard deviation as well as a negative correlation around 0.8 between $L_{>300}$ and the normalized very low frequency power, VLF/P, linking the segmentation outcomes to standard measures.
In order to understand the scaling behaviour of the extracted trends in the time series, we compute the mean variance of the segments given a segment length (Fig. 2) which indicates a power function.

Discussion

In this paper we present the analysis of nonstationarities in heart rate by means of a nonparametric segmentation algorithm, being able to display differences between CHF and age-matched EH, as well as CHF and YH (Fig. 1). Also, differences between YH and EH can be detected, showing the aging effect in the loss of complexity of the heart rate (Fig.1).

The high positive correlation between $\%\mu_{50}$ and sdNN shows that the latter one is dominated by the large jumps. A negative correlation between $L_{>300}$ and VLF/P could reflects the reduction of longer segments by means of respiratory disorders which are prevalent in 30% to 50% of patients with CHF.
It is worth to mention here the similarity of Fig. 2 with plots given by detrended fluctuation analysis (DFA) [8]. In comparison to these results scaling exponent 0.6 in CHF indicates that random walk fluctuations dominate the dynamics of this group. For the EH and YH groups, the both exponents, 0.4 and 0.2, indicate power law correlations associated to the interchange of large and small RR intervals.
Through the outcomes of segmentation we have access to time characteristics of the signal that were no longer available, making possible a different approach to quantify nonstationarities in HRV analysis. Results are in agreement with previous knowledge and do not require arbitrary thresholds or excludes fragments of the time series. The individual risk stratification ability of this method relies in further applications to cardiological data bases.

Acknowledgement

We acknowledge Prof. Schirdewan for providing data. SC and CA acknowledge CNPq (Brazilian agency) for financial support. MR, NW and JK acknowledge the Deutsche Forschungsgemeinschaft, grant numbers DFG RI2016/2-1, WE 2834/5-1, KU837/29-2, and KU837/35-1.

Bibliography

[1] Task Force: Guidelines - heart rate variability, European Heart Journal vol. 17, pp. 354, 1996.
[2] Bernaola-Galvan, P., Ivanov, P. Ch. et al.: Scale invariance in the nonstationary of human heart rate, Phys. Rev. Lett. vol. 87, pp. 168105, 2001.
[3] Camargo, S., Queiros S. M. D. et al.: Nonparametric segmentation of nonstationary time series, Phys. Rev. E vol. 84, pp. 046702, (2011).
[4] Hirsch, J., B. Bishop: Respiratory sinus arrhythmia in humans: how breathing pattern modulates heart rate, American Journal of Physiology-Heart and Circulatory Physiology vol. 241, pp. H620, (1981).
[5] Goldberger, A. L., Amaral, L. A. N. et al.: http://circ.ahajournals.org/cgi/content/full/101/23/e215
[6] Wessel, N., Schirdewan, A. et al.: Intermittently decreased beat-to-beat variability in congestive heart failure, Phys. Rev. Lett. vol. 91, pp. 119801, 2003.
[7] Wessel, N., Malberg, H. et al.: Nonlinear methods of cardiovascular physics and their clinical applicability. International Journal of Bifurcation and Chaos vol. 17, pp. l3325, 2007.
[8] Peng, C. K., Havlin S. et al.: Quantification of scaling exponents and crossover phenomena in nonstationary heartbeat time series, Chaos vol. 5, pp. 82, 1995.

Biomed Tech 2013; 58 (Suppl. 1) © 2013 by Walter de Gruyter · Berlin · Boston. DOI 10.1515/bmt-2013-4171

T WAVE MORPHOLOGY DURING HEART RATE TURBULENCE IN PATIENTS WITH CHRONIC HEART FAILURE

Lenis G, Dössel O

Institute of Biomedizdical Engineering, Karlsruhe Institute of Technology (KIT), Germany

Gustavo.Lenis@kit.edu

Abstract: *Heart Rate Turbulence (HRT) is the distinctive response of the sinus rhythm of the heart to an isolated ventricular ectopic beat (VEB). The quantification of this process can be used to stratify the risk of sudden cardiac death in patients with a history of acute myocardial infarction. A sensitivity of around 30% has been achieved in different studies. However, the large number of misleading results of the method suggests that new and better risk stratifiers could be developed. In this work, Holter ECG recordings were used to analyze the morphology of the T wave during the HRT in patients with chronic heart failure. The HRT was characterized by newly introduced parameters. In addition, the comparison between normal T waves before and after the VEB showed small but significant changes in morphology. The morphological changes of the T wave could be used for diagnostic purposes.*

Keywords: Electrocardiogram, T Wave, Heart Rate Turbulence, Morphology

Introduction

During a normal HRT, a sinus acceleration follows the compensatory pause after the VEB. The initial acceleration is then succeeded by a deceleration that finally stabilizes at the original RR cycle length. The acceleration and deceleration processes are quantified by the parameters Turbulence Onset (TO) and Turbulence Slope (TS) [1]. Normal values for these parameters are TO<0% and TS>2.5 $ms/beat$. The risk stratification class of a subject is 0 if both parameters are normal. The stratification classes 1 or 2 are chosen depending on the number of abnormal HRT parameters of the patient. A variety of studies has been carried out to evaluate the HRT parameters as risk stratifiers. In general, this procedure delivers a sensitivity of 30%, a specificity of 90% and positive predictive value of 32% [1]. Thus, the amount of false positives and false negatives is high and remains of great concern.

In a previous work [2], a new interpretation of the HRT was given. The HRT was characterized by a second order linear time invariant system. In analogy to the theory of vibrations, a damping coefficient d, together with a resonance angular frequency ω_0, were introduced to quantify HRT. It was stated that these two new parameters should deliver a more global description of the HRT process.

Furthermore, the morphology of the first normal T wave after the VEB was compared to the last normal T wave before it. A significant reduction in its amplitude could be observed after the VEB. Furthermore, the amplitude of the T wave did not return to the original value instantaneously, but rather following an exponential trend. This phenomenon was called Morphological Heart Rate Turbulence (MHRT). New parameters were also defined to quantify MHRT. However, the diagnostic value of MHRT still remains unknown. In this work, we studied MHRT in patients suffering from chronic heart failure. Standard risk stratification parameters gained from HRT were compared to the new parameters presented in the previous and current studies [2].

Methods

Long term ECG monitoring was obtained from a specially designed Holter device. The device records 3 channels at a sample frequency of 256 Hz.

Signal processing: A complex signal processing work flow is needed to carefully investigate ECG wave morphology. First, the R peaks are detected in the ECG signal and their corresponding QRS complexes are extracted and classified. The VEBs suitable for HRT analysis are identified. According to HRT rules, 5 normal beats before the VEB and 15 after it are needed for a reliable analysis. Second, RR intervals are measured for the QRS complexes in the vicinity of each VEB. The HRT is then constructed and the parameters TO and TS are calculated. Subsequently, the estimation of the damping coefficient d and the resonance angular frequency ω_0 is carried out.

Third, the T waves in the vicinity of each VEB are segmented. A mean T wave is built for each beat and compared to a template of the normal T waves. In this work, two morphological features (MF) are introduced to measure how the T wave changes in time and specially after the VEB. The first feature (MF_1) is related to the normalized energy of the difference signal between T wave and template:

$$MF_1(i) = \frac{2 \cdot \int_{-\infty}^{\infty} T_i(t) \cdot Template(t) dt}{\int_{-\infty}^{\infty} (T_i(t))^2 + (Template(t))^2 dt} \cdot 100\% \quad (1)$$

where $T_i(t)$ represents the ith T wave during the HRT and $i \in \{-5, -4, .., 15\}$. The second parameter (MF_2) is the correlation coefficient between the template and each of the T waves:

$$MF_2(i) = \frac{cov\{T_i(t), Template(t)\}}{\sqrt{var\{T_i(t)\}} \cdot \sqrt{var\{Template(t)\}}} \cdot 100\% \quad (2)$$

Patient Nr.	TO $[\%]$; TS $[\frac{ms}{beat}]$	d ; ω_0 $[s^{-1}]$	MTO_1 $[\%]$; MTS_1 $[\frac{\%}{s}]$	MTO_2 $[\%]$; MTS_2 $[\frac{\%}{s}]$
1	0.91 ; 0.18	1.03 ; 1.12	-0.32 ; 0.22	-0.29 ; 0.21
2	-0.01 ; 1.54	2.84 ; 0.36	-0.18 ; 0.05	-0.17 ; 0.11

Table 1: Exemplary MHRT analysis for two patients suffering from chronic heart failure

Notice that if the template and the ith T wave are exactly equal, the parameters MF_1 and MF_2 are equal to 1.

MHRT processing: MHRT is quantified in an analogous way to the HRT. Two MHRT parameters were introduced for this purpose [2]. This definition can be applied for both MF_1 and MF_2.

$$MTO_k = \frac{MF_k(1) - \frac{1}{4}\sum_{i=-5}^{-1} MF_k(i)}{\frac{1}{4}\sum_{i=-5}^{-1} MF_k(i)} \cdot 100\% \quad (3)$$

$$MTS_k = \frac{MF_k(2) - MF_k(1)}{RR(7)} \quad (4)$$

where $k \in \{1, 2\}$ and $RR(7)$ denotes the RR interval length (in seconds) of the beat number 7. MTO represents the initial perturbation in T wave morphology. MTS reflects the speed at which the morphological perturbation returns to its original value.

Figure 1(a) shows the HRT obtained for patient number 1. The MHRT constructed for MF_1 can be seen in figure 1(b). The T wave obtained from beat number 7 and the T wave template can be seen in figure 1(c). Even though the shape of the displayed T waves is very similar, their morphology is indeed different with a statistical significance of $p < 1\%$.

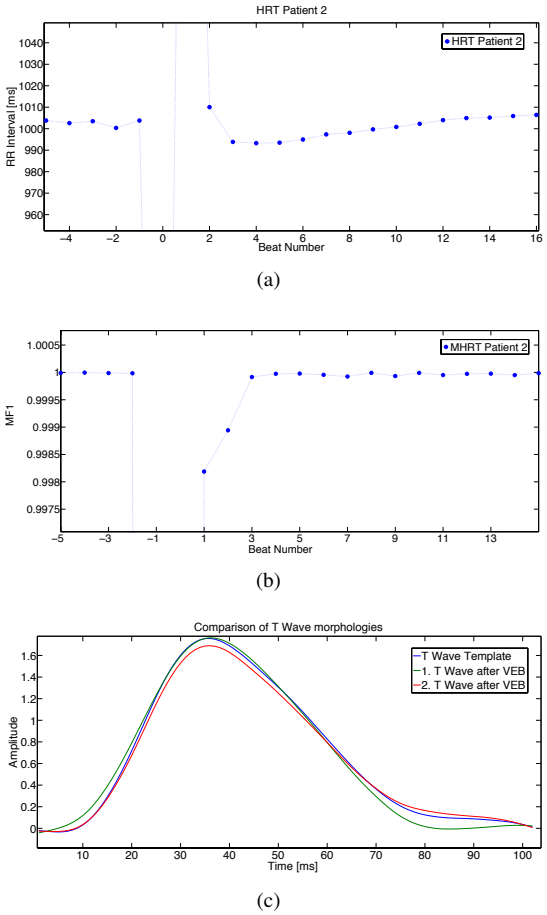

Figure 1: Analysis for patient 1. (a): HRT. (b): MHRT displayed for MF_1. (c): T waves after VEB and template.

Results

Table 1 shows the results for the MHRT analysis run in exemplary manner for 2 patients. Using only the standard HRT parameters TO and TS, patient 1 would be stratified with the highest risk class 2. However, the damping coefficient d of his HRT response is slightly greater than one. This means, the HRT is slightly over damped. The MHRT coefficients show an evident initial perturbation in T wave morphology after the VEB but a fast restitution of original shape. In contrast, patient number 2 is stratified with HRT risk class 1. However, his damping coefficient d is noticeable higher, what describes a far less responsive turbulence. Furthermore, the MHRT coefficients show a mild initial perturbation of the T wave morphology but a slower restitution of original shape.

Discussion

The newly introduced HRT parameters d and ω_0 present partially incompatible values with the ones delivered from the standard HRT parameters. This could lead to new information about the health status of the patient. The MHRT analysis contains also new and interesting information and has to be studied in further detail to make definite conclusions. It appears to the authors that the initial perturbation in morphology (MTO) and the speed how it goes back to its original value (MTS) a has some diagnostic value.

Acknowledgements

The authors would also like to thank Prof. Dr. rer. nat. Wilhelm Stork and his research group for providing the Holter ECGs.

Bibliography

[1] A. Bauer *et al.*, "Heart rate turbulence: Standards of measurement, physiological interpretation, and clinical use," *Journal of the American College of Cardiology*, vol. 52, pp. 1352–1366, 10 2008.

[2] G. Lenis *et al.*, "Ectopic beats and their influence on the morphology of subsequent waves in the electrocardiogram.," *Biomed Tech (Berl)*, pp. 1–11, 02 2013.

Biomed Tech 2013; 58 (Suppl. 1) © 2013 by Walter de Gruyter · Berlin · Boston. DOI 10.1515/bmt-2013-4172

EXPLORING EFFECTIVE CONNECTIVITY BY A GRANGER CAUSALITY APPROACH WITH EMBEDDED DIMENSION REDUCTION

Britta Pester[1], Lutz Leistritz[1], Herbert Witte[1] and Axel Wismueller[2]

[1]Bernstein Group for Computational Neuroscience Jena, Institute of Medical Statistics, Computer Sciences and Documentation, Jena University Hospital, Friedrich Schiller University Jena, Germany

[2]Department of Imaging Sciences, Department of Biomedical Engineering, University of Rochester Medical Center, Rochester, New York, USA

Britta.Pester@mti.uni-jena.de

Abstract: *We propose applying the linear Granger Causality concept to very high-dimensional time series. The approach is based on integrating dimensionality reduction into a multivariate time series model. If residuals of dimensionality reduced models can be transformed back into the original space, prediction errors in the high–dimensional space may be computed, and a Granger Causality Index (GCI) is properly defined. We provide a proof–of–principle, and compare the results with the classical GCI.*

Keywords: *Granger Causality Index, Dimension reduction*

Introduction

A basic problem in quantifying directed information transfer is the consideration of effective connectivity in very high–dimensional (HD) systems. Currently, HD systems are transformed into a lower dimensional system, e.g. by Principal or Independent Component Analysis (PCA, ICA), and the connectivity structure of derived components is studied. Here the drawback is that a revealed interaction cannot be readily transferred back into the original HD space. Thus, directed interactions between the original network nodes are not revealed, which limits the interpretation of identified interaction patterns. Granger Causality (GC) is a suitable concept for assessing connectivity structures between time series. One popular approach uses principles of prediction [1], whereby application of a straightforward generalization to general time series models is enabled, providing an appropriate definition of prediction errors. Instead of analyzing interactions between derived components, a large scale GC (lsGC) approach preserves the interpretability of the original network nodes. The idea of that approach is the integration of a dimension reduction into a multivariate time series model, which allows computation of prediction errors in the original HD space.

Methods

A D–dimensional, p–th order MVAR process is given by $\mathbf{Y}(n) = \sum_{r=1}^{p} \mathbf{A}^r \mathbf{Y}(n-r) + \mathbf{E}(n),\ n = 1, \ldots, N$, with AR–parameters $\mathbf{A}^r \in \mathbb{R}^{D\times D}$ and a zero mean, uncorrelated noise process $\mathbf{E}$. In the case of HD data, a simple AR estimation is not possible as computational capacity rapidly meets its limits. Thus, in a first stage PCA serves as a preprocessing step for dimension reduction: $\mathbf{X} = \mathbf{W}\mathbf{Y}$, with $\mathbf{Y} = \big(\mathbf{Y}(1), \ldots, \mathbf{Y}(N)\big)$, the principal component (PC) matrix $\mathbf{X} \in \mathbb{R}^{D\times N}$, and the mixing matrix $\mathbf{W} \in \mathbb{R}^{D\times D}$. Let $\mathbf{X}^C$ and $\mathbf{W}^C$ be the reduced PC and mixing matrices consisting of the first C rows of $\mathbf{X}$ and $\mathbf{W}$, respectively. $\mathbf{X}^C(n)$ is now MVAR–modeled, and the modeled time series $\hat{\mathbf{X}}^C(n)$ is afterwards transformed back into the original HD space via left multiplication of the pseudo inverse $\mathbf{W}^{C+}$ of $\mathbf{W}^C$. The residuals of the whole model are then gained by $\hat{\mathbf{E}} = \mathbf{W}^{C+}\hat{\mathbf{X}}^C - \mathbf{Y}$. For GCI computations, the processing of the reduced data $\mathbf{Y}^{d-}$, where the d-th row of $\mathbf{Y}$ is deleted, can be performed in two different ways:

(a) *Multi PCA* (mPCA): for every $\mathbf{Y}^{d-}$ a separate PCA is performed, i.e. $\mathbf{X}_m^{d-} = \mathbf{W}_m^{d-}\mathbf{Y}^{d-}$, where $\mathbf{X}_m^{d-}$ and $\mathbf{W}_m^{d-}$ are calculated anew by PCA for each d. After reducing $\mathbf{W}_m^{d-}$ to dimension C and estimating the corresponding AR model, the modeled series $\hat{\mathbf{X}}_m^{d-}(n)$ can be calculated.

(b) *Single PCA* (sPCA): only one PCA is applied before eliminating rows of $\mathbf{Y}$, and modifications of the mixing matrix $\mathbf{W}$ are used for the dimension reduction of $\mathbf{Y}^{d-}$, i.e. $\mathbf{W}$ is reduced to $\mathbf{W}_s^{d-} \in \mathbb{R}^{C\times D-1}$ by eliminating the last $D-C$ rows and the d-th column. Now $\mathbf{X}_s^{d-} = \mathbf{W}_s^{d-}\mathbf{Y}^{d-}$ serves for the AR parameter estimation resulting in the modeled series $\hat{\mathbf{X}}_s^{d-}(n)$.

The residuals amount to $\hat{\mathbf{E}}_{m/s}^{d-} = \mathbf{W}_{m/s}^{d-\ +} \cdot \hat{\mathbf{X}}^{d-} - \mathbf{Y}^{d-}$. The lsGCI from d_1 to d_2 is then defined by $\gamma_{d_2\leftarrow d_1} = \ln\left(\hat{\Sigma}_{d_2}^{d_1-}/\hat{\Sigma}_{d_2}\right)$, where $\hat{\Sigma}_{d_2}$ and $\hat{\Sigma}_{d_2}^{d_1-}$ are the d_2-th diagonal entries of the covariance matrices of $\hat{\mathbf{E}}$ and $\hat{\mathbf{E}}^{d_1-}$.

Data

To compare the lsGCI with the conventional GCI, we considered a time series dimensionality that functions with both approaches. We realized 50–dimensional stationary MVAR processes of order two and various N between 125 and 1000. Thereby, the entire network structure was given by five pairwise different internal networks $\boldsymbol{N}_1, \ldots \boldsymbol{N}_5$ with ten nodes each (Fig. 1). The corresponding AR-parameters were chosen according to the AR-model of Baccala et al. [2], Fig. 4, and were scaled by factor 0.5 to ensure the stationarity of the entire process. The internal networks $\boldsymbol{N}_k$

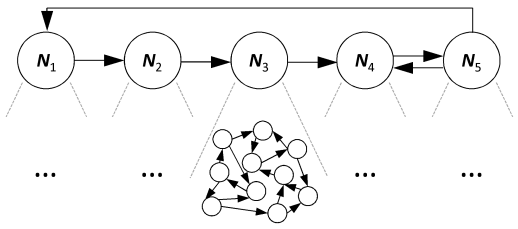

Figure 1: Network structure with five internal networks.

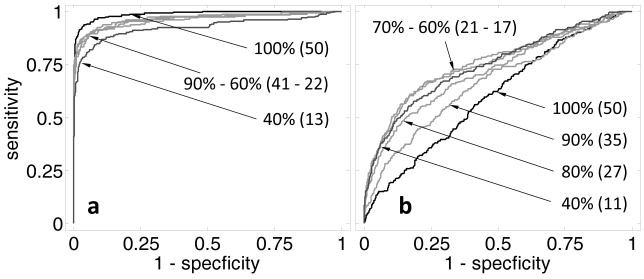

Figure 3: ROC curves for $N = 500$ (a) and $N = 125$ (b). The percentages specify the amount of variance explanation; numbers in parentheses specify C.

incorporate 20 directed edges by setting the associated first order AR-parameter to 0.2. The in- and out–degree of each node equals two. Finally, there are 20 randomly generated directed edges from nodes of $\boldsymbol{N}_1$ to nodes of $\boldsymbol{N}_2$, from nodes of $\boldsymbol{N}_2$ to nodes of $\boldsymbol{N}_3$, etc. (see Fig. 1). The added $E_d(n)$ were i.i.d. N(0,1) for all d and n.

Results

To evaluate the novel approach and to assess the effects of methodological differences by applying PCA we used the concept of ROC curves. Thereby (ls)GCIs serve as realizations of the test variable, and the status variable is defined by the presence (positive) or absence (negative) of an edge. First, the discriminative power of both PCA embeddings was investigated for different time series lengths, and differing amounts of variance explanation. As shown in Fig. 2 the sPCA approach exhibited primarily larger areas under the ROC curve (AUC). This finding was also confirmed for all other investigated time series lengths. Thus all subsequent analyses were performed with the sPCA approach. Secondly, ROC curves were used to analyze differing amounts of variance explanation. Fig. 3 depicts examples for $N = 500$ and $N = 125$. As expected for large N, the dimension reduction resulted in an inferior performance depending on the number of components reduced. However, this performance is within acceptable limits for reasonable dimensionality reductions (Fig. 3a). For small N, the embedded dimension reduction yielded a performance increase (Fig. 3b). Finally, we considered the detection accuracy after significance testing (Tab. 1) ($\alpha = 5\%$, adjusted for multiple comparisons by False Discovery Rate).

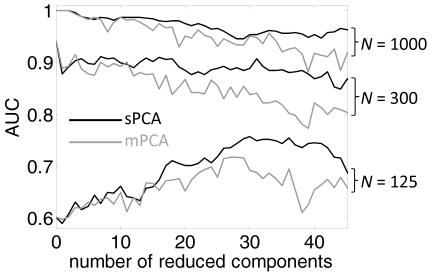

Figure 2: AUCs for different dimension reduction degrees.

Discussion

PCA is appropriate to extend linear GCI to HD time series. It reduces HD into lower-dimensional (LD) time series of PCs. LD time series are AR modeled, and the model residuals are transformed back into the original HD space. This transformation offers a better interpretability of results, enabling analysis of interactions between components of the original time series vs. between derived components (PCs). Alternative dimensionality reductions could also be considered if a back-transformation of the model residual from a temporary LD to the original HD space is allowed. An embedded dimension reduction appears to the quality of the network identification when enough time series samples are available, yet classical GCI still performs well. For shorter time series an embedded PCA seems to result in an improvement, most likely due to smaller AR parameter matrices and reduced estimator variances.

Table 1: Sensitivities and specificities after significance testing. The column '%' specifies the variance explanation.

N	*C*	*%*	**Sens.**	**Spec.**
500	50	100	70.5	97.7
	41	90.6	70.0	97.6
	27	70.3	65.4	97.6
125	50	100	0.4	97.8
	35	90.7	4.1	97.7
	21	70.8	6.8	97.5

Acknowledgement

This study was supported by the grant 01GQ1202 of the Federal Ministry of Education and Research (Germany), as well as by the NIH grant 1R01DA034977-01 (USA).

Bibliography

[1] C. W. J. Granger, "Investigating causal relations by econometric models and cross-spectral methods," *Econometrica*, vol. 37, no. 3, pp. 424–438, 1969.

[2] L. A. Baccala and K. Sameshima, "Partial directed coherence: a new concept in neural structure determination," *Biological Cybernetics*, vol. 84, no. 6, pp. 463–474, 2001.

Biomed Tech 2013; 58 (Suppl. 1) © 2013 by Walter de Gruyter · Berlin · Boston. DOI 10.1515/bmt-2013-4173

COORDINATION AND TIMING OF HEART RATE COMPONENTS OF CHILDREN AND ADOLESCENTS WITH TEMPORAL LOBE EPILEPSY

Schiecke K[1], Wacker M[1], Benninger F[2], Feucht M[2], Witte H[1]

[1]Institute of Medical Statistics, Computer Sciences and Documentation, Jena University Hospital, Friedrich Schiller University Jena, Germany
[2]Epilepsy Monitoring Unit, Department of Child and Adolescent Neuropsychiatry, University Hospital Vienna, Austria

Karin.Schiecke@mti.uni-jena.de

Abstract: *The aim of our study was to reveal specific patterns of the heart rate variability (HRV) during pre-ictal, ictal, and post-ictal periods in epileptic children. The continuous Morlet-wavelet transform was adapted to explore the time-frequency characteristics of the HRV (scalogram, linear and non-linear phase locking, and band-power analyses). The empirical mode decomposition was used to separate HRV components (e.g. blood-pressure-related waves and respiratory sinus arrhythmia). Their time-variant non-linear predictability was analysed (point prediction error). Timing and coordination of HRV components occurs 100 s before seizure onset producing a higher degree of synchronization and a higher predictability of HRV. The combined use of advanced linear and non-linear methods is crucial for this result.*

Keywords: *children, epilepsy, heart rate variability, signal-adaptive decomposition, time-frequency analysis*

Introduction

HRV analysis in epilepsy has been carried out with two major clinical objectives. One is to reveal causes for sudden unexpected death in epileptic patients. Another focus is using *HRV* analysis as a tool for automated seizure prediction. The pre-ictal, ictal and post-ictal *HRV* courses have been investigated by using time- and frequency-domain features. Features of the time-frequency domain have received much less attention. Non-linear *HRV* analyses are frequently applied also in epileptic patients. However, the methods are usually time-invariant (for stationary signals) and not frequency-selective. The aim of this study is to demonstrate that combinations of time-variant, frequency selective, linear and non-linear analysis methods can be beneficially applied for *HRV* analysis in epileptic patients. Our working hypothesis is that phase properties of and between *HRV* components react sensitively before *EEG* seizure occurs. This hypothesis is based on our findings with regard to *EEG* burst activity which is accompanied by strong phase coupling reactions [1]. Two rhythms are of particular interest: The Traube-Hering-Mayer waves found in blood pressure, which occur also in the *HRV* (low-frequency range *LF*: 0.04 - 0.15 Hz), and the respiratory sinus arrhythmia (*RSA*) (high-frequency range *HF*: 0.15 - 0.4 Hz). The *HRV* data were previously analysed (visual analysis of heart rate) and the results were published by Mayer et al. [2].

Methods

Subjects and HRV computation: The *HRV* data of 18 patients were analysed (median age 9 years 4 months, range 6 years 10 months to 18 years 0 month). Presurgical evaluation was performed following a standard epilepsy surgery protocol. *EEG* and *ECG* data were recorded referentially against *Pz* (filter 1 to 70 Hz; sampling frequency 256 Hz). Seizure onset and termination in the *EEG* were determined independently by two reviewers. *EEG* and *ECG* samples including 10 minutes epochs (5 minutes before (pre-ictal state) and 5 min after the seizure onset (seizure and post-ictal state) were analysed. *QRS* detection was performed and used for the heart rate computation. The low-pass filtered event series (*LPFES*) was utilized applying the French-Holden algorithm. The final *HRV* representations were down sampled to 8 Hz.
Continuous Morlet transform (MWT) and derived time-variant parameters: The frequency-dependent complex analytic signal of the *HRV* is computed by using the *MWT*. Power and phase information of the complex analytic signal can be extracted. The scalogram *S* and the phase-locked scalogram S_{PL} were estimated. From *S* and S_{PL} the mean band power for each sampling point is computed for the frequency bands 0.04 - 0.15 Hz (*LFP*) and 0.15 - 0.4 Hz (*HFP*) according to the task force standards. Amplitude-independent phase-locking effect were analysed by the phase-locking index *PLI*. Quadratic phase coupling (*QPC*) between both frequency bands given above are computed by using time-variant mean bi-amplitude (*mBA*) and (normalised) mean bi-coherence (*mBC*) in the region of interest (*ROI)* [3].
Empirical mode decomposition (EMD) and derived time-variant parameters: The *EMD* decomposes the *HRV* into intrinsic mode functions (*IMF*s). *EMD* preserves non-linear properties of the separated components. Therefore, averaged time-courses of non-linear point prediction error (*PPE*) of the *IMF*s were calculated. The *PPE* computation procedure was described by Schwab et al. [4]. High *PPE* denotes low non-linear predictability and vice versa.
Statistics: The non-corrected Rayleigh test (α=10%) was used to create a trigger threshold of strong phase-locking in a *PLI* time-frequency map. In order to estimate confidence tubes of the mean time-courses of the extracted parameters a Bootstrap approach was used (1000 bootstraps, sample size 600 s, lower bound 5% / upper bound 95% percentile).

Results

HR courses: In Fig. 1A the *HR* courses of all seizures and the averaged *HR* are depicted. The averaged *HR* is characterised by a slow increase 60 s before seizure onset, and fast acceleration followed by deceleration during seizure.
MWT-based analysis: In non-phase locked *S* (Fig. 1 B) the occurrence of strong Mayer-wave related *LF* and *RSA*-related *HF* component became most apparent between 200 and 300 s, collapsed with the onset of seizure, recurred with strong power at 380 s (end of seizure) and got less pronounced up to the end of analysis interval.

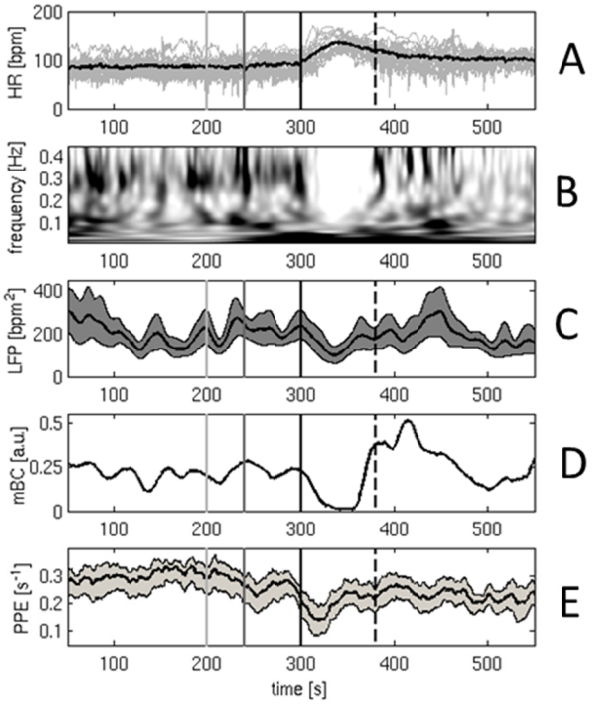

Figure 1: Original *HR* courses and derived parameters. "Bar code" of specific time points: black line - seizure onset, dashed black line - seizure termination, dark grey line - start of pre-onset acceleration, light grey line - start of timing and coordination of *HR* components. A) *HR* courses (grey: 18 seizures, bold black: averaged HR). B) *MWT*-based time-frequency related *S* analysis (black: high/white: low power). C) mean *LFP* band course and confidence tube. D) time-variant *mBC* in the *ROI*. E) mean *PPE* course and confidence tube of *EMD*-based *IMF2* component (*RSA*-related).

Power ridges in phase-locked scalogram S_{PL} could be observed at similar time-pattern as in *S*, and *LF* component related peaks in the *PLI* also occurred more often between 200 and 300 s (not shown). *LFP* (Fig. 1 C) as well as *HFP* band ranges (not shown) differ significantly during seizure in comparison to pre-ictal period (240 to 300 s) and parts of post-ictal period.
The *mBA* (not shown) and *mBC* (Fig. 1 D) revealed lower values during pre-ictal period, increased with a peak at the beginning of pre-onset acceleration of *HR* (240 s) and at seizure onset, and dropped down during seizure. The termination of seizure is accompanied by a rise of *mBC*.

EMD-based analysis: *EMD* separated the *HRV* into *IMF*s which are connected to specific components of *HR* (e.g. *IMF2*: *HF* component (≈0.3 Hz) / *IMF3*: *LF* component (≈0.1 Hz)). Averaged *PPE* of the original *HRV* (not shown) started to decrease (=higher predictability) at 260 s, showed significant increase during seizure and significant difference between pre- and post-ictal period (incomplete recuperation). The predictability of *IMF2* (Fig. 1 E) increased around 200 s (decrease of *PPE*), decreased shortly between 240 and 300s and significantly increased during seizure. Mean *PPE* is lower during post-ictal in comparison to pre-ictal period (no significant difference).

Discussion

An epileptic seizure is a time-dependent process, and time-variant *HRV* analysis may provide better information on the dynamics of coupling mechanisms between relevant cortical structures and the autonomic nervous system. The most striking clinical result of our methodological study is that timing and coordination of *HRV* components arises 100 s before *EEG*-seizure onset producing a higher degree of synchronization and a higher predictability of *HRV*. Certainly, this result is based on grand mean results and cannot be generalized to each patient/seizure. However our working hypothesis, that phase properties of the *HRV* components can be utilized for the description of these reactions/couplings, was confirmed. Our processing scheme is composed of time-variant analysis methods and the results complement each other. By means of the *MWT* the classical (time-invariant) power parameters can be made available as parameter courses. In addition, time-variant phase-locking and quadratic phase coupling can be examined. The results serve as a gold standard for signal-adaptive approaches like *EMD*. Although the *EMD* has method-intrinsic drawbacks, e.g. *EMD*'s filter characteristics are not always sufficient for biomedical applications and mode-mixing occurs, *EMD* based approaches provide advantages which should be used for *HRV* analysis.

Acknowledgement

This study was supported by the DFG (Wi 1166/10-2).

Bibliography

[1] Schwab, K., Skupin, H. et al.: Coordination of the EEG and the heart rate of preterm neonates during quiet sleep, *Neurosci. Lett.* , vol. 465, pp. 252-256, 2009
[2] Mayer, H., Benninger, F. et al.: EKG abnormalities in children and adolescents with symptomatic temporal lobe epilepsy, *Neurology*, vol. 63, pp. 324-328, 2004
[3] Witte, H., Putsche, P. et al.: Time-variant analysis of phase couplings and amplitude-frequency dependencies of and between frequency components of EEG burst patterns in full-term newborns, *Clin. Neurophysiol.*, vol. 122, pp. 253-266, 2011
[4] Schwab, K., Groh, T. et al.: Nonlinear analysis and modeling of cortical activation and deactivation patterns in the immature fetal electrocorticogram, *Chaos*, vol. 19, pp. 015111, 2009

Biomed Tech 2013; 58 (Suppl. 1) © 2013 by Walter de Gruyter · Berlin · Boston. DOI 10.1515/bmt-2013-4174

Correlation between autonomic dysfunction and impaired microcirculation in patients with schizophrenia

Seeck, A[1], Bär, KJ[2], Haueisen, J[3], Voss, A[1]

[1] Department of Medical Engineering and Biotechnology, University of Applied Sciences, Jena, Germany
[2] Department of Psychiatry and Psychotherapy, University Hospital, Jena, Germany
[3] Institute of Biomedical Engineering and Informatics, Technical University of Ilmenau, Germany

andreas.voss@fh-jena.de

Abstract: *Patients suffering from schizophrenia have an increased mortality risk due to cardiovascular events that might be associated with cardiac autonomic dysfunction. The aim of this study was to analyse the inter-dependencies between indices of autonomic regulation from heart rate and blood pressure variability, and spectral indices of Laser-Doppler-Flowmetry signals, reflecting the condition of the microcirculatory system. Therefore, we compared the correlation between indices in controls with indices in schizophrenic patients. We found that short term interaction between autonomic regulation and microcirculation decreases in schizophrenic patients compared to healthy controls while the permanently increased heart rate in patients is highly correlated with a periphery endothelial and sympathetic activation.*

Keywords: *Laser Doppler Flowmetry, Spectral Analysis, Heart Rate Variability, Blood Pressure Regulation*

Introduction

Several studies have documented an increased mortality risk due to cardiovascular events in patients suffering from schizophrenia [1, 2]. Some authors suggested that these events might be associated with cardiac autonomic dysfunction, specifically a decrease in vagal modulation and an increase in sympathetic activity. Bär et al. [3, 4] found a significant reduction of baroreflex sensitivity and heart rate variability as well as an increase of QT variability in schizophrenic patients indicating an autonomic imbalance.

Recently the analysis of peripheral microcirculation by means of Laser Doppler Flowmetry (LDF) has revealed a significantly altered microcirculation in patients with acute schizophrenia compared to healthy subjects [5]. The LDF is a non-invasive technology that facilitates the study of microcirculation via spectral analysis of the LDF signal. Five relevant frequency subintervals were introduced for spectral analysis of blood flow signals [6, 7]. Three of these intervals are associated with the local mechanisms of vasomotion, namely: the frequency band from 0.01-0.02 Hz (vascular endothelial activity), the frequency band from 0.02-0.06 Hz (neurogenic activity) and the frequency band from 0.06-0.2 Hz (myogenic response). The other two bands are related to the transmission of global hemodynamic alterations to microcirculation: from 0.2-0.6 Hz (respiratory activity) as well as from 0.6-1.6 Hz (cardiac activity). The aim of this study was to analyse the interdependencies between indices for the assessment of autonomic regulation, especially linear indices from heart rate and blood pressure variability, and indices from spectral analysis of LDF signals that reflect the condition of the microcirculatory system. Therefore, we compared the correlation coefficients between indices in healthy controls with indices in patients suffering from acute schizophrenia in order to figure out if pathologic alterations are detectable and if the interaction between autonomic regulation and microcirculatory regulation is impaired in schizophrenic patients.

Methods

In this study 37 healthy subjects (CON, mean age 34.6±11.8 years, 21 males and 16 females) and 32 patients (PAT, mean age 35.9±11.9 years, 16 males and 16 females) were enrolled. The investigation conforms to the principles outlined in the Declaration of Helsinki. Local ethics committee approval and the informed consent of all subjects were provided.

The LDF signals in two tissue depths (D1: 2mm; D2: 6mm) as well as an electrocardiogram (sampling frequency 1600 Hz) and continuous non-invasive blood pressure (Portapres, TNO Biomedical Instrumentation) were recorded simultaneously. A post-occlusive reactive hyperaemia test was performed, i.e. a forearm ischemia was produced by a pneumatic cuff placed on the upper arm and inflated to 30 mmHg above systolic blood pressure. After 3 minutes the cuff was deflated and registration of hyperaemia started.

From ECG and blood pressure recordings, time series of beat-to-beat intervals (BBI), systolic blood pressure (SBP) values and diastolic blood pressure (DBP) values were extracted. From the BBI time series several indices from time and frequency domain were calculated according to the guidelines of the Task Force [8]. Additionally, comparable time domain parameters were extracted from SBP and DBP time series [9].

From the two LDF signals the Short Time Fourier Transform (STFT) was calculated and features in the three frequency subintervals reflecting local mechanisms were determined referring to endothelial, sympathetic and myogenic activity. The activities of the respiratory and cardiac subintervals were not included in this analysis since they refer to global hemodynamic processes.

Table 1: Significant correlations between indices of cardiovascular regulation and indices of local microcirculation

	endothelial				sympathetic				myogenic			
	D1		D2		D1		D2		D1		D2	
	CON	PAT	CON	PAT	CON	PAT	CON	PAT	CON	PAT	CON	PAT
BBI_meanNN				++				++				
BBI_Shannon												
BBI_VLF/P	+				++							
BBI_LF/P					++				++			
BBI_LF/HF					+		+		+		++	
SBP_Shannon												++
DBP_meanNN					-							
DBP_Shannon		-										+

+: positive correlation with |r|<0.4; ++: positive correlation with |r|>0.4; -: negative correlation with |r|<0.4

A Spearmen rank correlation was performed between all indices for both groups respectively. The statistical significance level was set to $\alpha<0.05$.

Results

The analysis revealed significant correlations between indices from linear HRV and spectral indices for all three subintervals in CON. The significant correlations are presented in Table 1. The endothelial end sympathetic components in D1 showed positive linear correlations with the index VLF/P (0.003-0.04 Hz) from BBI. Additionally, the sympathetic and myogenic activities are linearly related to the frequency parameter LF/P (0.04-0.15 Hz) in D1 and the ratio LF/HF in both tissue depths. These correlations are not significant for PAT. In contrast, PAT showed high correlations between meanNN and the endothelial and sympathetic activity in D2.
The Shannon entropies of SBP and DBP were positively related to the myogenic component in the patients group in D2. Furthermore, a negative linear relation between the mean of DBP and sympathetic activity in CON as well as between the Shannon entropy of DBP and the endothelial component in PAT were detected.

Discussion

The results of the control group show significant correlations between the central frequency parameters of BBI and their respective peripheral frequency intervals of microcirculation. Further on, a physiologic negative correlation between DPB_meanNN and sympathetic activity is found confirming known issues [10]. In the patient group these correlations disappeared completely, probably due to the impairment of the autonomic regulatory processes. Schizophrenic patients are characterized by a strong increase of heart rate and sympathetic activity. This is accompanied by a strong positive correlation between meanNN and the endothelial and sympathetic activity in this group. The patients additionally showed an increase in the Shannon entropy of SBP and DBP ($p=0.02$ from Mann-Whitney-U-test) compared to CON. The correlation of the myogenic component with these parameters might reflect a stronger local response to the variability of blood pressure. In conclusion the short term interaction between autonomic regulation and microcirculation decreases in schizophrenic patients compared to healthy controls while the permanently increased heart rate is highly correlated with the periphery (increased) sympathetic activation.

Acknowledgement

This study has partly been supported by grants of the University of Applied Sciences, Jena and the Deutsche Forschungsgemeinschaft (DFG: Vo 505/8-2).

Bibliography

[1] Enger, C., Weatherby, L. et. al.: Serious cardiovascular events and mortality among patients with schizophrenia, *J Nerv Ment Dis,* vol. 192, no. 1, pp. 19-27, Jan, 2004.

[2] Brown, S., Inskip, H. et. al.: Causes of the excess mortality of schizophrenia, *Br J Psychiatry,* vol. 177, pp. 212-7, Sep, 2000.

[3] Bär, K.J., Koschke, M. et. al.: Acute psychosis leads to increased QT variability in patients suffering from schizophrenia, *Schizophr Res,* vol. 95, no. 1-3, pp. 115-23, Sep, 2007.

[4] Bär, K.J., Boettger, M.K. et. al.: Decreased baroreflex sensitivity in acute schizophrenia, *J Appl Physiol,* vol. 102, no. 3, pp. 1051-6, Mar, 2007.

[5] Seeck, A., Israel, A.K. et. al.: Dynamic microvascular blood flow analysis during post-occlusive reactive hyperemia test in patients with schizophrenia, *Ann Biomed Eng,* vol. 39, no. 7, pp. 1972-83, Jul, 2011.

[6] Stefanovska, A., Bračič, M. et. al.: Wavelet analysis of oscillations in the peripheral blood circulation measured by laser Doppler technique, *IEEE Trans Biomed Eng,* vol. 46, pp. 1230-1239, 1999.

[7] Bracic, M., Stefanovska, A.: Wavelet-based analysis of human blood-flow dynamics, *Bull Math Biol,* 60, no. 5, pp. 919-35, Sep, 1998.

[8] Heart rate variability. Standards of measurement, physiological interpretation, and clinical use. Task Force of the European Society of Cardiology and the North American Society of Pacing and Electrophysiology, *Eur Heart J*.; vol.17, no. 5, pp. 354-81, Mar, 1996

[9] Bär, K.J., Berger, S. et. al.: Autonomic dysfunction in unaffected first-degree relatives of patients suffering from schizophrenia, *Schizophr Bull,* vol. 36, no. 5, pp. 1050-8, Sep, 2010.

[10] H. Suzuki, and T. Saruta, *Kidney and Blood Pressure Regulation*: Karger, 2004.

Biomed Tech 2013; 58 (Suppl. 1) © 2013 by Walter de Gruyter · Berlin · Boston. DOI 10.1515/bmt-2013-4175

A WEARABLE DEVICE FOR REALTIME ASSESSMENT OF VIGILANCE

Hanke S[1], Oberleitner A[1], Lurf R[1] and König G[1]

[1]AIT Austrian Institute of Technology GmbH, Austria

sten.hanke@ait.ac.at

Abstract: *International recognized research groups have presented studies where EEG and EOG biosignals were used to visualize and classify sleep stages. Based on these state of the art fndings an automated detection and classifcation of sleep stages has been realized. Beyond that there is a mandatory necessity for an automated classification and estimation of vigilance and alertness during the wake state. This paper presents recent work on a classification model, implemented in a wearable device. Its application opens the opportunity to calculate a quantitative vigilance profile in real time, in real life situations. It has been shown that the device is suitable to acquire necessary biosignals in an unobtrusive way, and perform real-time vigilance classification.*

Keywords: *vigilance, wearable, EOG, signal processing*

Introduction

In the presented project a mobile setup has been developed which allows an uncomplicated and easy to assess long and short term vigilance profile recording and therefore a real time evaluation of the algorithms in real life situations. All developed algorithms have been implemented in the prototype processor platform. For a mobile setup, a compensation of movement artefacts and a light-weight hardware design as well as an easy self applicable sensor unit have been developed. The algorithms and the setup have been tested in first measurements. The algortihms integrated into the mobile hardware allow a more precise and complete insight into the alertness condition than current clinical test methods for vigilance assessment. The vigilance profile is based on physiological patterns respectively biomarkers in the time and frequency domain. As a first reference for the retrieved vigilance information the parameters from the approved alertness test have been used.

Methods

For developing the initial vigilance model and the algorithms, we used data measured on persons doing the Mackworth Clock test (a classic clock test). The results of this test setup have been presented earlier in Hanke *et al.*([1]).
For analysing the filtered EOG signals in time and frequency domain, 20-seconds time windows (2560 samples) with an overlap of 10 seconds (1280 samples) were used. Due to the overlapping windows technique there are no missed window pattern characteristics due to window transitions. After the filtering process, an Independent Component Analysis (ICA) has been performed. Three signal characteristics have been used for a further processing: the preprocessed amplitude signal, the calculated velocity signal and the mean power of both EOG channels.
The introduced algorithms have been tested and validated with 24h polysomnography data from the Sensation European Commission project[1]. The data has been recorded by the Sensation project partners in the year 2004. As specification for the recordings the protocols from the SIESTA project group[2] have been used. Overall in this study 100 all-night polysomnographies and 50 daytime polygraphic recordings under controlled conditions in 50 healthy subjects across all adult age ranges, and 100 24-hour ambulatory recordings from another 50 subjects have been performed. All recordings will consist of at least 16 channels (EEG, EOG, EMG, ECG, respiration, and others). For the EOG, a sampling rate of 200 Hz and a band pass filter of 0.1 to 40 Hz have been applied. For the 24h recordings 50 normal healthy controls have been recorded on two consecutive 24 hour periods.

Results

In the figure 1 the results of different analysis for the recorded EEG and EOG data are displayed. The first graph shows the results of a permutation entropy calculation for 4 EEG channels (fp1, c3, c4, o1) based on a paper of Olofsen *et al.* ([2]). The permutation entropy (PE) describesm a frequency characteristic of the EEG signal. As the parameter is coming from the anaesthesia is seems like it is a parameter which is calculated very much to a binary decision making. For the original purpose of decision making for the diagnosis of being anaesthetised or not anaesthetised this might be appropriate but for a detailed continuous vigilance assessment the parameter might not be optimal. The parameter shows in a good way epochs where the person is asleep and epochs where the person is awake.
The two graphs in the second picture of figure 1 are showing two different EMG values over time. Displayed is the mean value of the tibialis and submental EMG channel. Especially the tibialis EMG channel measured at the tibia can not count as artefact in the EEG. Therefore this EMG channel can be a possible correlation parameter for the EEG and EOG vigilance results. Especially recovery or sleeping phases are clearly indicated by the EMG measurements. The last three pictures are showing the results of the amplitude, velocity and frequency analysis of the EOG channel. The EOG results are showing a clear differentiation

[1]Sensation - Advanced Sensors Development for Attention Stress, Vigilance and Sleep/Wakefulness Monitoring

[2]http://www.thesiestagroup.com/index.php last seen: 19.05.2011

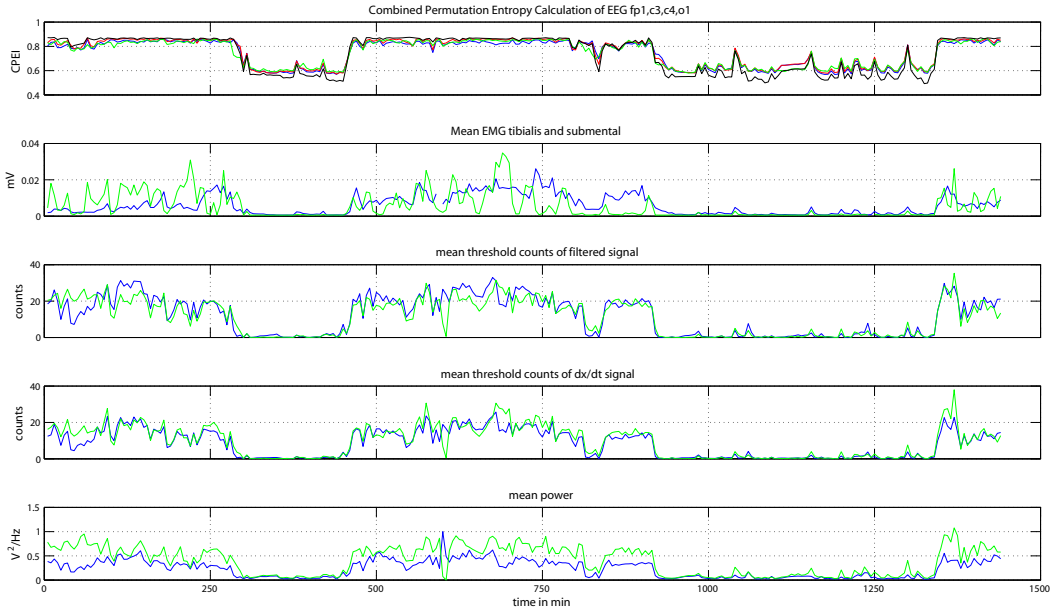

Figure 1: Results from a 24-h EOG and EEG measurement.

between awake and sleeping phases. But also in the awake phase the EOG seems to be a more clear indication for a vigilance dynamic than the entropy from the EEG. Of course this dynamic must be proven to reflect the vigilance with further tests and a correlating parameter which is indicating vigilance. Such a parameter does not exist in these 24h polysomnographic measurements.

For the purpose of data acquisition, a special dedicated hardware device was developed. The device has been tailored to be used in real life environments. The device called "'vigilance recorder"' allows rechargeable battery powered data acquisition of 2 EOG- und 6 EEG channels with 24bit resolution and 250Hz sampling rate per channel, over a period of up to 10 hours.

The data is preprocessed and can be streamed directly via Bluetooth to a computer or a mobile device, or stored on a microSD card respectively. Time information is provided by a built-in real time clock.

Discussion

It can be assumed that all described parameters extracted from EOG are useful to monitor the eye activity. Based on state-of-the art research findings it can be concluded that there is not just a single overall level of alertness as there is no single parameter vigilance. There are several alertness levels depending on which specific measure is considered and there are several parameters reflecting vigilance behaviour. The miniaturization of the necessary hardware and the more artefact resident combination of hardware design and software can bring the setup to applications like sleep surveillance which can now be brought into a familiar environment away from a clinical setting. This is also important for future research to leave the measured persons in an unobtrusive way in their daily live routine, which is an important fact but difficult to realize with older setups. The data aquisition is for the expert staff in a lot of application less time-consuming but allows at the same time a more precise measurement. The development of EEG and EOG sensors and electrodes has been pushed in the last years and made a step forward. This allows a better integration and enhancement of mobile setups. With such system a data aquisition can be performed outside the laboratory which is highly important for the quantitative measurements.

Acknowledgement

The work presented in this paper has been founded by the Austrian Research Promotion Agency (FFG) - (project number 827600).

Bibliography

[1] S. Hanke, J. Zeitlhofer, G. Wiest, W. Mayr, and D. C. Moser, "Automated Vigilance Classification based on EOG signals: Preliminary Results," *World Congress on Medical Physics and Biomedical Engineering, September 7 - 12, 2009, Munich, Germany*, vol. 25/9, pp. 428–431, 2009.

[2] E. Olofsen, J. W. Sleigh, and A. Dahan, "Permutation entropy of the electroencephalogram: a measure of anaesthetic drug effect," *British Journal of Anaesthesia*, vol. 101, no. 6, pp. 810–821, 2008.

Biomed Tech 2013; 58 (Suppl. 1) © 2013 by Walter de Gruyter · Berlin · Boston. DOI 10.1515/bmt-2013-4176

REAL-TIME SOFTWARE FOR FUNCTIONAL MAPPING OF ELOQUENT CORTEX USING ELECTROCORTICOGRAPHY

R. Prueckl[1], C. Kapeller[1], C. Potes[2], M. Korostenskaja[3], G. Schalk[2], Ki H. Lee[3], C. Guger[1]

[1]g.tec Guger Techologies OG, Schiedlberg, Austria
[2]Wadsworth Center, Albany, NY, USA
[3]Florida Hospital for Children, Orlando, FL, USA

prueckl@gtec.at

Abstract: *In this work, we present and validate a software package for functional mapping of eloquent cortex using task-related changes in gamma activity recorded from subdural electrocorticography electrodes prior to resective brain surgery. The software is designed for use by non-experts in addition to traditional mapping procedures such as electrical cortical stimulation (ECS) mapping.*

Keywords: *Functional Mapping, Electrocorticography, Epilepsy, Electrical Cortical Stimulation, Gamma Activity*

Introduction

Epilepsy is a disorder of the brain that impairs the quality of life of people by the effects of seizures or medication. For some of the patients, who are resistant to antiepileptic medication, surgical resection of the seizure focus can reduce or even cure epilepsy. Prior to the resection, the identification of eloquent cortex is important in order to minimize the possibility of functional deficits [1]. This has been done using several different approaches. Amongst them the most common is ECS [2]. While ECS is effective, it also has substantial problems [3]. We designed and validated a clinical product based on published methods [4] that is reliable and easy to use as a tool for cross-checking or narrowing down the sites of interest. The system analyzes data acquired from ECoG electrodes for task-related changes in the gamma band (i.e., between 60 and 170 Hz).

System Architecture

On the hardware side of the system, a synchronized array of high resolution multi-channel biosignal amplifiers (g.USBamp, g.tec Guger Technologies OG, Austria) is connected to the electrodes implanted in the brain of the patient. The amplifiers digitize the signals and transfer them to the recording computer. This computer has two screens, one for the patient that displays instructions for the tasks, the other for the operator, displaying the mapping results. See Fig. 1.

The Montage Creator is used to create a schematic picture of the implanted electrodes. For this purpose, the software comes with a library of electrode grid shapes. The program then generates a list pointing out how to connect the

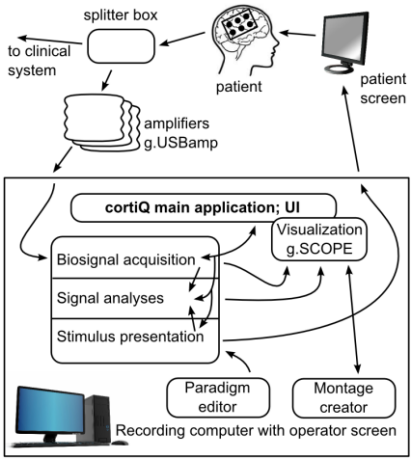

Figure 1: Hard- and software architecture of the cortiQ system.

grids to the amplifier. The Paradigm Editor is there for efficient editing of the tasks the patient should accomplish. The contents of the tasks can be designed using images, audio files, text, or tactile stimulation. Also referencing can be influenced, e.g., tasks vs. baseline or task x vs. task y. The Main Application provides the operator with a structured way of conducting the experiment with little need for input. After selecting the montage, raw data channels can be checked for data quality. Here, exclusion of noisy channels and re-assignment of ground and reference electrodes is possible. Then, the paradigm is selected and started. In real time, the results of the mapping are displayed according to the montage for each individual task and electrode as circles with different diameters. Additionally, the magnitude of the response is displayed.
Signal acquisition, signal processing, and stimulus presentation run as sub-processes in the background, and analyze the data according to methods that build on those described in [5].

System Validation

Two epilepsy patients from Florida Hospital for Children (Orlando, FL, USA) participated in the experiments. They underwent surgery to place subdural ECoG electrode grids over different brain regions. Eloquent cortex of the patients was identified using ECS. The patients gave informed consent through a protocol reviewed and approved by the review board of the Florida Hospital for

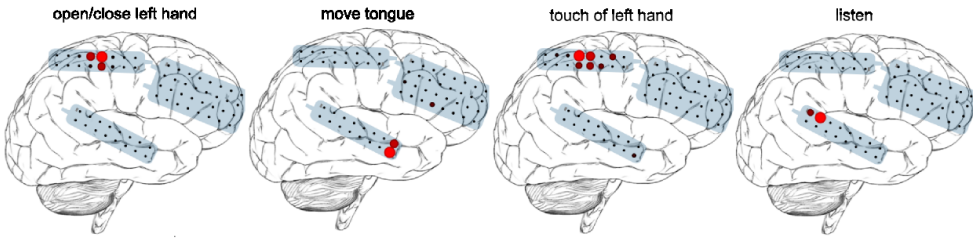

Figure 2: Topographical result maps of patient 1 as displayed on the operator screen.

Children.
After the preparation, the electrode montages and the paradigm, data were collected with the g.USBamp amplifiers at the bedside of the patients and processed by the cortiQ software in real time, gradually building the result in form of topographical brain maps that shows the task-related differences in activity (see Fig. 2).
The patients went through 3 repetitions of a paradigm which contained four tasks: open/close the left hand (task 1), move the tongue (task 2), feel the touch which is applied to the palm of the left hand (task 3), listen to a story (task 4). Each task had a length of 15 seconds with 15 seconds relaxation baseline in between.

Results

The outcome of the software is compared to the results of ECS mapping. Specifically, we counted the sites that were assigned to a particular function/area in the ECS procedure and checked whether the significant result values of the cortiQ software were at the same or at the next neighbor locations. Task 4 was not checked with ECS, so it was excluded from analyses. For both patients the error rates for tasks 1 to 3 reveal no false negative detections and the grand average of false positive identifications is 1.24 %.

Discussion

We demonstrated a clinical hardware and software system for cortical functional mapping of the eloquent cortex to be used prior to resective surgeries in epilepsy patients. Based on methods from previous research [4, 5], the results of the software are in the close neighborhood to locations determined by the well-established ECS procedure. While ECS has been applied regularly over the past decades, it has some important drawbacks. We expect that cortiQ software should provide distinct benefits to mapping of eloquent cortex. Most importantly, the results from cortiQ mapping may be used to optimize subsequent ECS mapping.

Bibliography

[1] A. Chakraborty, A. W. McEvoy, Presurgical functional mapping with functional MRI, *Curr Opin Neurol* 21 (4) (2008) 446–451.

[2] K. Hara, S. Uematsu, R. Lesser, B. Gordon, J. Hart, E. Vining, Representation of primary motor cortex in humans: studied with chronic subdural grid, *Epilepsia* 32(suppl) (1991) 23–24.

[3] S. Arroyo, R. P. Lesser, et al. (2004). Subdural Electrodes. *Electroencephalography: Basic Principles, Clinical Applications, and Related Fields*. E. Niedermeyer and F. L. d. Silva. Baltimore, Lippincott Williams & Wilkins: 701-711.

[4] P. Brunner, et al. "A practical procedure for real-time functional mapping of eloquent cortex using electrocorticographic signals in humans." *Epilepsy & Behavior* 15.3 (2009): 278-286.

[5] G. Schalk, E. C. Leuthardt, P. Brunner, J. G. Ojemann, L. A. Gerhardt, J. R. Wolpaw, Real-time detection of event-related brain activity, *Neuroimage* 43 (2) (2008) 245–249.

Biomed Tech 2013; 58 (Suppl. 1) © 2013 by Walter de Gruyter · Berlin · Boston. DOI 10.1515/bmt-2013-4177

A SYSTEM FOR ONLINE NEUROELECTROMAGNETIC SOURCE IMAGING

Christof Pieloth[1], Thomas Knösche[2], Burkhard Maess[2] and Mirco Fuchs[1,2]

[1]Laboratory for Biosignal Processing, HTWK Leipzig, Leipzig University of Applied Sciences, Germany
[2]Max-Planck-Institute for Human Cognitve and Brain Sciences, Leipzig, Germany

pieloth@labp.htwk-leipzig.de

Abstract: *Electroencephalography (EEG) and magnetoencephalography (MEG) provide an insight into neuronal processes in the brain in a real-time scale. Brain activity can be modeled in terms of a source distribution found by solving the bioelectromagnetic inverse problem, e.g. using linear source reconstruction methods. Such methods are particularly suitable to be used on modern highly parallel processing systems, such as widely available graphic processing units (GPUs). The utilization of these capabilities paves the way for online neuroelectromagnetic source imaging. We present a system that, according to its modular scheme, can be configured in a very flexible way using graphical building blocks. It allows to use different preprocessing algorithms together with a linear source reconstruction method. The algorithms use both CPU and GPU resources.*

Keywords: *EEG, MEG, Source Reconstruction, GPGPU*

Introduction

EEG/MEG provides an insight into brain processes in a real time scale, which is not possible with hemodynamic imaging techniques as, for example, functional magnetic resonance imaging (fMRI). A common method in EEG/MEG analysis is distributed source localization, which is based on modeling sources as equivalent current dipoles that densely cover the space where activity is expected. See [1] for a short overview.

Due to the high computational effort of source reconstruction, online was not possible so far. Modern high performance computing frameworks, for example provided by NVIDIA's CUDA[1], open new possibilities for online EEG/MEG analysis. For example, a method recently proposed in [2] is optimized for GPUs. Source localization requires several preprocessing steps, e.g., artefact correction, filtering, epoch separation and averaging. They require user interaction, and are therefore usually performed offline. It is not unusual that data is useless due to insufficient signal quality, e.g., because of artifacts. Online processing could not just overcome such problems, but also provides the visualization of brain activity during measurements, which is interesting for both medical and researching applications.

We present an application that allows to set up and tune an online processing chain, including source localization.

[1] http://www.nvidia.com/object/cuda_home_new.html

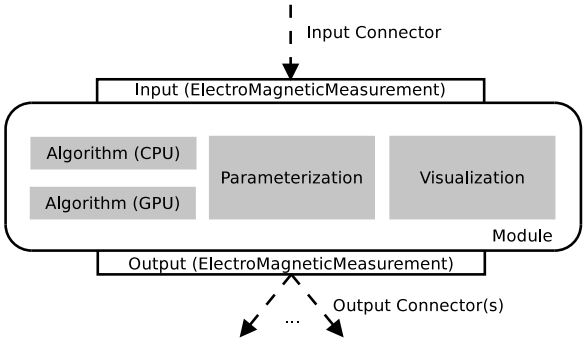

Figure 1: Abstract structure of a module in OpenWalnut.

Concept and Implementation

To account for the requirements of high flexibility and extensibility, the basic idea of the concept is to split the signal processing chain into separate functional units, i.e. modules, that can be put together. Each module is realized in terms of a prototype that becomes part of a processing chain after parameterization. This allows to set up and reuse modules easily, even several times during the same measurement. The module's intended functionality is reflected by a certain algorithm that can either be executed on the CPU or on the GPU. The implementation of our concept is based on *OpenWalnut*, a software for multi-modal brain visualization [3]. This platform also follows a strict modular concept, where modules have so called input and output connectors to interact with other modules. These connectors can have any data type, only outputs and inputs that are directly connected need to share the same data structure. Whenever a module updates data at its output connector, linked modules are scheduled to allow seamless processing. Besides this useful architecture, OpenWalnut provides an intuitive mechanism to select modules and put them together by means of graphical building blocks.

According to our concept and the architecture of OpenWalnut, the structure of a module is summarized in Fig. 1. It is worth to note that each module has to provide desired visualization capabilities. On the one hand, this provides a very high flexibility and also allows a relatively easy implementation because of nonexisting dependencies or information from other modules. On the other hand, already a few sophisticated active visualizations can become computationally intractable and, besides that, drastically increase the complexity of the user front-end. Therefore visualization can be deactivated if desired.

Results

So far, the following modules were implemented: *Electromagnetic Measurement*, *FIR Filter*, *Epoch Separation*, *Epoch Averaging*, *Source Reconstruction*. *Electromagnetic Measurement* serves as a collector that reads different data, e.g. head models, from different files and provides a link to EEG/MEG data. The *FIR Filter* module is used to filter the signals according to lowpass, highpass, bandpass and bandstop characteristic. It provides CPU and GPU execution of the filter algorithms. *Epoch Separation* splits the continuous data stream according to stimulus information into single epochs that range from a time point before to a point after stimulus onset. *Epoch Averaging* allows to calculate moving or total average of detected epochs. *Source Reconstruction* estimates a source distribution according to a linear source reconstruction algorithm, e.g. the minimum norm method [4]. It is implemented for CPU and GPU.

To examine the feasibility of online processing, recorded data was streamed through a pipeline of a bandpass filter with an order of 200, an epoch separation/averaging and finally, a source reconstruction for EEG data with 244662 sources. For streaming we used a block size of 1s and the epoch separation/averaging module was setup with a pre/post stimulus time of -100/+200ms.

Tab. 1 shows the averaged processing time of each module for a block of 1s. As can be seen, the processing time for *FIR Filter* and *Source Reconstruction* drastically decreases if the GPU is used. The total processing time for the CPU-only[2] case exceeds the block size by approx. 50 percent, while the total time for GPU-supported[3] processing is in the range of less than 20 percent of the block size. A total processing time less than the block size is necessary in order to process incoming data in time, i.e. to provide online capabilities. Given the setup presented here, this can only be achieved using the GPU.

Table 1: Averaged processing time for one block, all times in milliseconds.

	CPU-only	**GPU-supported**
FIR Filter	86	31
Epoch Separation	2	2
Epoch Averaging	2	2
Source Reconstruction	1416	130
Total sum	**1506**	**165**

Conclusion

We have shown that the current system can principally be used to reconstruct and visualize evoked brain activity based on distributed source localization during EEG/MEG measurements. Particular the usage of GPUs provides promising resources that can be used to improve the system further and to implement additional functions and algorithms such as artefact detection and rejection.

We currently realize the physical link to an EEG/MEG system (Neuromag Vectorview System, Elekta, Helsinki, Finland) using the MNE C++ library[4], which is hosted at the MPI for Human Cognitve and Brain Sciences Leipzig.

Some issues need to be solved before the presented system is finally ready for a productive use. For example, the source reconstruction requires the recalculation of the inverse operator whenever the estimated signal-to-noise-ratio (SNR) changes, which is basically the case whenever a new epoch is detected. While this is currently ignored for practical reasons, a compromise to account for that could be to calculate a set of inverse operators in advance, where each covers a certain SNR range. Thus, recalculation would be replaced by the selection of an appropriate operator. Further, the system currently requires that the Leadfield matrix is available at the begin of a measurement. However, the actual EEG sensor positions are required for this calculation which are unknown before the measurement. One possible solution is to calculate a high resolution Leadfield matrix based on virtual EEG electrodes that densely cover the head surface. The Leadfield for the true sensor positions can than be derived from Leadfield interpolation or nearest neighbor selection. For MEG, a Leadfield matrix can be calculated before the measurement under the assumption that the head is centered in the device. To account for the head movement, a method based on a simplified source model and a minimum norm inverse algorithm could be an efficient solution [5].

[2] Intel Xeon E5620 CPU with 2.4 GHz

[3] NVIDIA Tesla C2070

[4] `http://www.martinos.org/mne`

Acknowledgement

Supported by grants of the Federal Ministry of Education and Research (Germany, 17108X10) and the European Social Fund (100098255).

Bibliography

[1] S. Baillet, J. Mosher, and R. Leahy, "Electromagnetic brain mapping," *Signal Processing Magazine, IEEE*, vol. 18, pp. 14–30, nov 2001.

[2] C. Dinh, J. Rühle, S. Bollmann, J. Haueisen, and D. Güllmar, "A gpu-accelerated performance optimized rap-music algorithm for real-time source localization," in *Biomed Tech 2012*, 2012.

[3] S. Eichelbaum, M. Hlawitschka, A. Wiebel, and G. Scheuermann, "Openwalnut - an open-source visualization system," in *Proceedings of the 6th High-End Visualization Workshop* (W. benger, A. Gerndt, S. Su, W. Schoor, M. Koppitz, W. Kapferer, H.-P. Bischof, and M. D. Pierro, eds.), December 2010.

[4] M. S. Hämäläinen and R. J. Ilmoniemi, "Interpreting magnetic fields of the brain: minimum norm estimates," *Medical and Biological Engineering and Computing*, vol. 32, no. 1, pp. 35–42, 1994.

[5] T. R. Knösche, "Transformation of whole-head meg recordings between different sensor positions," *Biomedical Engineering / Biomedizinische Technik*, vol. 47, pp. 59–62, 2002.

Biomed Tech 2013; 58 (Suppl. 1) © 2013 by Walter de Gruyter · Berlin · Boston. DOI 10.1515/bmt-2013-4178

DETECTION OF MULTIPLE PACEMAKER CENTERS IN CARDIOMYOCYTE CELL LAYERS FOR ESTIMATING WAVEFRONT PROPAGATION PATTERNS

R. Kienast[1], M. Stöger[1], M. Handler[1], G. Fischer[1], F. Hanser[1] and C. Baumgartner[1]

[1]Institute of Electrical and Biomedical Engineering , UMIT, Hall in Tyrol, Austria

roland.kienast@umit.at

Abstract: *Multielectrode arrays are more commonly used to investigate fundamental electrophysiological mechanisms of cardiac cell monolayers. However, a problem for investigating propagation direction dependent features such as propagation velocity or field potential rise time may arise through the presence of multiple active pacemaker centers in a cultured cell layer. Therefore, we developed a novel algorithm based on the spatial gradient of the wavefront's arrival time to extract information about the spatial and temporal distribution of active pacemaker centers in the cell layer. This information can be used to improve the analysis of propagation dependent features.*

Keywords: *electrophysiology, multielectrode arrays, field potentials, cardiomyocytes*

Introduction

Cardiac cell monolayers cultured on multielectrode arrays (MEAs) are commonly used for investigating the electrophysiology of cardiomyocytes at tissue level under normal or pathologic conditions [1]. Presence of multiple active pacemaker centers in a cultivated cell layer, however, causes problems in the investigation of propagation-direction-dependent features, such as the propagation velocity or field potential rise time [2]. This likely changes the origin of excitation and, consequently, changes the direction of wavefront propagation. The analysis of these parameters requires accurate information about the spatial distribution and temporal activation of these pacemakers centers. To overcome this problem, an algorithm was developed capable of extracting information from experimental data in order to study wavefront propagation characteristics of each single pacemaker center separately.

Methods

Cell culture: Primary embryonic cultures of ventricular cardiomyocytes from chicken were plated onto high-resolution MEAs. This MEA comprises 60 electrodes and is connected to a special data acquisition system (Multi Channel Systems MCS GmbH, Reutlingen). The extracellular signals were registered with a sampling rate of 20 kHz per electrode and the cells were actively held at a temperature of 37°C. Besides the natural pacemakers, artificial stimuli were also used to alter and conduct the starting point of excitation.

Algorithm: The source of excitation of a single wavefront is detected in registered data by calculating the spatial gradient (two dimensional) of the wavefront's arrival time in the MEA. Algorithm 1 shows a pseudo code description of the algorithm to estimate the spatial origin of the pacemaker center from registered experimental data.

Algorithm 1 Pseudo code for excitation source detection

Require: Detected spikes of all field potentials for a single wavefront moving across the array
Start
Get time stamps of each spike
Calculate gradient of the wavefront arrival time
for $i = 1 \rightarrow$ Number of Electrodes **do**
for $j = 1 \rightarrow$ Number of Electrodes **do**
$il \leftarrow$ Line equation (gradient, electrode i)
$jl \leftarrow$ Line equation (gradient, electrode j)
$P_{ij} \leftarrow il \cap jl$
end for
end for
Divide area into bins.
Count P_{ij} (intersection points) for each bin.
return Source $\leftarrow$ bin with maximum P_{ij} count.
End

The calculated information of the spatial excitation source of each single wavefront propagation was further processed to identify local clusters of active pacemaker centers on the array. After locating each excitation source the temporal activity was determined. To allow a visual inspection of the quality of cluster separation, contour plots of each single wavefront propagating across the MEA were generated and superimposed on the information of the temporal distribution of the single active pacemaker centers. A high degree of inhomogeneity is a visual indicator for a false detection.

Results

A dataset of a multiple pacemaker cell layer experiment was analyzed to demonstrate the suitability of the proposed algorithm. Properties of this dataset are summarized in Table 1 .

Figure 1 shows the estimated spatial distribution of the excitation sources outside the MEA's area. The degree of activity of each center is shown in Figure 2. Temporal

Table 1: Dataset description

Property	Value
Time of cultivation	3d
Active pacemaker centres	n = 4
Artificial stimulus centres	n = 1
Recording temperature	T = 37°C
Recording Time	t = 200s
Number of excitations	n = 169

activation patterns of each detected pacemaker center are displayed in Figure 3. Figure 4 shows superimposed contour plots for a visual quality check.

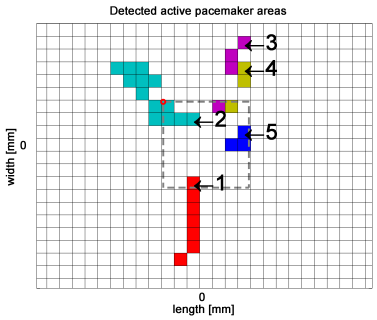

Figure 1: Detected areas of active pacemaker centers. Number 1 to 4 are biological pacemaker centers where number 5 indicates an artificial stimulus. The dashed line marks the MEA's area.

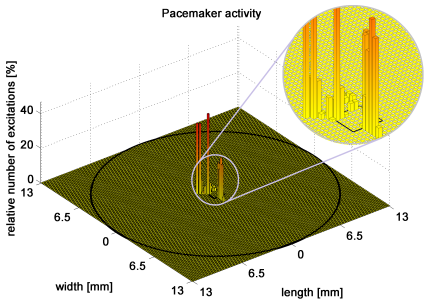

Figure 2: Degree of activity of multiple pacemaker centers. The black circle symbolizes the Petri dish. The active MEA's area is marked by the black square (zoomed field).

Conclusion

The proposed algorithm provides detailed information about the temporal and spatial distribution of active pacemaker centers within a cell culture of primary cardiomyocytes. Employing MEA technology this information can be used for an investigation of wavefront propagation-direction-depended features in field potentials such as propagation velocity or field potential rise time [2]. This is crucial to obtain a better understanding of these characteristics and thus of the underlying physiological mechanisms.

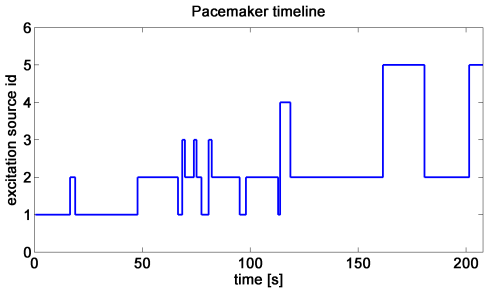

Figure 3: Temporal activation patterns of the detected pacemaker centers during the registration (id 1..4 physiological signals, 5 artificial stimulus).

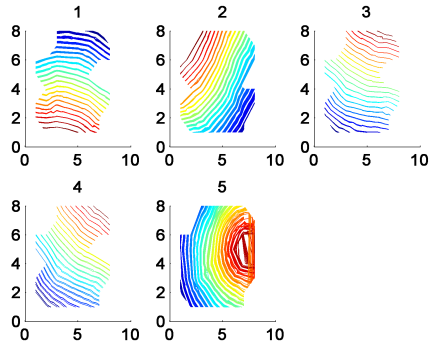

Figure 4: Automatically separated wavefront propagation patterns visualized as contour plots (red marks early activation). Plot 1 to 4 originates from pacemaker cells outside the active MEA's area. Plot 5 shows an artificially generated stimulus within the MEA's area. Plot 1 comprises n=41 excitations, plot 2 n=93, plot 3 n=3, plot 4 n=3 and plot 5 n=29 of a total of n=169 registered excitations (Table 1).

Acknowledgement

This work was funded by the K-Regio-Project of the Standortagentur Tirol, Innsbruck, Austria and by the European Regional Development Fund (ERDF).

Bibliography

[1] A. Stett, U. Egert, E. Guenther, F. Hofmann, T. Meyer, W. Nisch, and H. Haemmerle, "Biological application of microelectrode arrays in drug discovery and basic research," *Anal Bioanal Chem.*, vol. 377, no. 3, pp. 486–495, 2003.

[2] M. Halbach, U. Egert, J. Hescheler, and K. Banach, "Estimation of action potential changes from field potential recordings in multicellular mouse cardiac myocyte cultures," *Cell Physiol Biochem.*, vol. 13, no. 5, pp. 271–284, 2003.

Biomed Tech 2013; 58 (Suppl. 1) © 2013 by Walter de Gruyter · Berlin · Boston. DOI 10.1515/bmt-2013-4179

CNAP – EVOLUTION OF CONTINUOUS NON-INVASIVE ARTERIAL BLOOD PRESSURE MONITORING

Fortin J[1], Wellisch A[1], Maier K[1]

[1] CNSystems Medizintechnik AG, Reininghausstrasse 13, 8020 Graz, Austria

juergen.fortin@cnsystems.at

Abstract: *Blood pressure (BP) is one of the most important cardiovascular parameters in nearly every care area. A method for continuous non-invasive arterial pressure (CNAP) monitoring is described. CNAP is especially designed for perioperative, critical and emergency care. It concentrates on the clinically important BP-information such as absolute BP and BP-changes as well as physiological BP-rhythms and BP-waveforms, where other hemodynamic parameters like cardiac output (CO) and dynamic fluid management parameters (e.g. pulse pressure variation PPV) can be derived. For this kind of hemodynamic information, tailor-made mechanisms have been developed. Recent validation studies underline accuracy and clinical acceptance of the CNAP technology.*

Keywords: *Continuous, non-invasive, blood pressure*

Introduction

Up to now beat-to-beat BP monitoring has required invasive placement of an intra-arterial catheter (IBP). Due its invasive nature, IBP is applied in less than 20% of surgical patients [1]. The remaining 80% are monitored with intermittent upper arm sphygmomanometers (NBP), although discontinuous NBP is unable to track hemodynamic instabilities in up to 40% of all cases [2].

In addition, the concept of hemodynamic optimization using continuous BP and its derived parameters such as CO, PPV, etc. has shown an increase in medical outcome and thus has rapidly found acceptance in anesthesia and critical care [3]. Hemodynamic optimization could be performed in about 30% of all surgical procedures, if non-invasive continuous BP information would be available [1]. Non-invasive BP monitoring with accurate BP tracing as well as high-fidelity waveform to obtain hemodynamic parameters would be of high clinical interest.

However, patients in the OR, ICU or ER often receive high dose rates of vasoactive drugs to get their hemodynamic status regulated. These drugs not only induce fast changes in BP but also change the vascular tone of the peripheral arteries. Such vasomotor changes have a significant impact on the accuracy of BP in non-invasive technologies. Thus, older technologies have struggled with providing accurate values due to their lack of vasomotor artefact rejection [4, 5, 6]. CNAP was specifically designed to overcome these limitations. In this article the technological principles of CNAP and its advantages are briefly described and validation data is shown.

Methods

Continuous BP is measured with the help of a finger sensor combining two methods: The "Vascular Unloading Technique" (VUT) [7] is used for BP-rhythms and BP-waveforms and the new VERIFI-technology controls periods of slower BP-changes, where vasomotor tone may influence the measurement. Further, the resulting BP-signal is scaled to an initial upper arm NBP (absolute BP) by means of a mathematical transfer function (Figure 1).

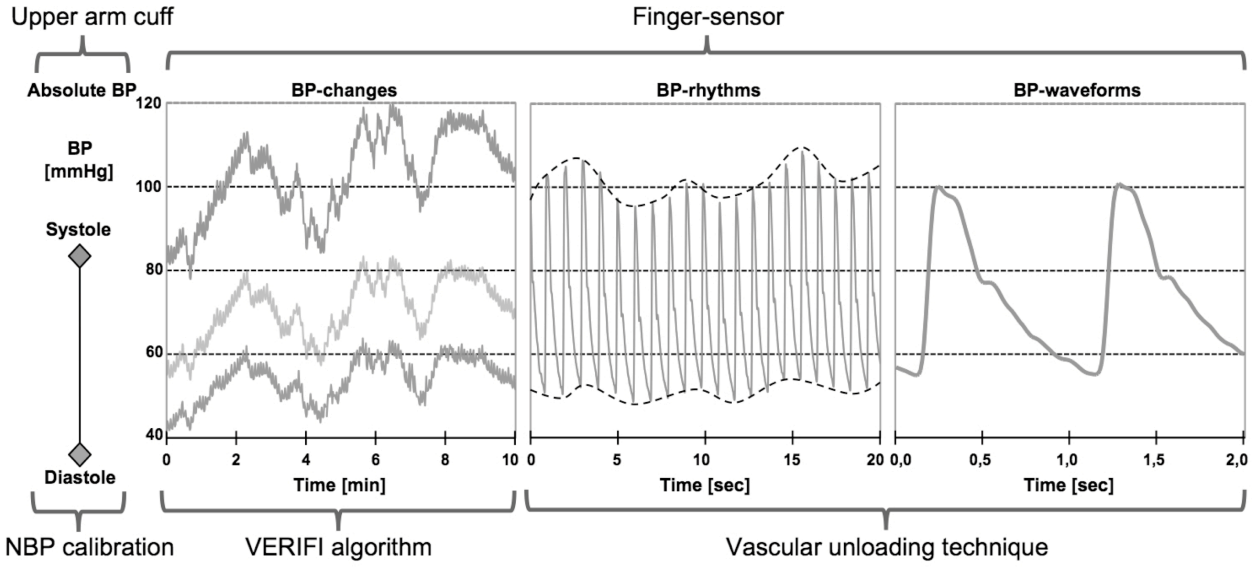

Figure 1: Interaction between the measurement locations (upper arm cuff and finger sensor) and technological methods (NBP-calibration, VERIFI and VUT) used for different BP-information.

Upper arm cuff BP is the gold standard in clinical practice [8]. Due to its daily use in clinical routine it is obvious that the physician wants to obtain continuous BP that is as accurate as the gold standard. Thus, a mathematical calibration to NBP is performed using a transfer function [9].
VUT is a sound method for measuring BP rhythms and waveforms. Typical VUT methods use a single control loop [10], which has to deal with fast pressure increase and release in the cuff as well as with the tracking of BP changes for the stability of the system. In contrast to older methods, a number of interlocking control loops is used within CNAP. Each inner loop is responsible for a well-defined characteristic of its underlying control mechanism and provides near-ideal conditions for the surrounding outer control loops. There are multiple loops for BP-waveforms and a loop for slower BP-rhythms [11].
However, for BP-changes and long-term stability VUT is directly affected by changes in vasomotor tone. Thus, for the measurement of BP-changes, the so-called VERIFI-algorithm has been designed:
Vasomotor changes typically affect the long-term BP changes in a time range below physiological BP-rhythms. This time range is filtered out and the VUT system operates with the signal content of BP-rhythms and pulse waves only. Thus, the vasomotor effect is eliminated, but also all relevant information of BP-changes. For the restoration, the VERIFI-algorithm inspects the waveforms on a beat-per-beat basis and identifies, if the control loop set point corresponds to mean BP. When there is a deviation, the system corrects the set point on an adaptive basis until the set point equals mean BP [9]. This "**V**asomotoric **E**limination and **R**econstructed **I**denti**F**ication of the **I**nitial set point" names the VERIFI-algorithm.
The accuracy and clinical value of CNAP was tested in several international clinical trials shown in Tab. 1 and 2.

Results

Table 1: Differences of IBP and CNAP (BP-changes):

Study (First Author)	Care Area	Patients	Bias mmHg	SD mmHg
Jagadeesh, 2012 [12]	ICU	30	-0,04	2,05
Neuner, 2012 [13]	OR	100	-3,1	9,45
Bias 2012 [14]	OR	25	-1,8	10,3
Ilies, 2012 [15]	OR	90	-4,3	10,4
Jeleazcov, 2010 [16]	OR	88	-1,6	11
Monnet, 2012 [17]	ICU	47	5	11

Table 2: Validation of BP-rhythms (PPV):

Study (First Author)	Care Area	Patients	Bias %	SD %
Monnet, 2012 [17]	ICU	47	-0,6	2,3
Bias 2011 [18]	OR	35	0,6	2,6

Discussion

Studies in Tab.1 show that CNAP provides BP traces in OR and ICU during daily routine within a clinically acceptable difference to IBP. PPV can accurately be derived from the CNAP-signal (Tab. 2). Further ongoing research shows accurate CO-estimation from pulse wave analysis (not shown). This high fidelity BP has technically become possible by combining VUT, NBP calibration and the VERIFI algorithm. The demonstrated accuracy, ease of use and non-invasive nature of the new CNAP technology allows clinicians to rapidly obtain all relevant BP information. CNAP allows for a new standard in routine patient monitoring in such areas where continuous hemodynamic information can clearly increase patient outcome.

Acknowledgement

The authors are employees of CNSystems Medizintechnik AG, which has developed and markets CNAP products.

Bibliography

[1] S. Maguire et al.: Respiratory Variation in Pulse Pressure and Plethysmographic Waveforms: Intrapoperative Applicability in a American Academic Center. *Anesth Analg.* 2011; 112(1): 94-96
[2] C. Ilies et al.: Detection of hypotension during Caesarean section with continuous non-invasive arterial pressure device or intermittent oscillometric arterial pressure measurement. *Br J Anaesth.* 2012 Sep;109(3):413-9.
[3] M. Hamilton et al.: A systematic review and meta-analysis on the use of preemptive hemodynamic intervention to improve postoperative outcomes in moderate and high-risk surgical patients. *Anesth Analg* 112(6), 1392–402. 2011
[4] BP. Imholz et al.: Effects of vasoconstriction upon the measurement of finger arterial pressure. *J Hypertens*, 10(9), 979–84. 1992
[5] R. Raamat et al.: Different responses of Finapres and the oscillometric finger blood pressure monitor during intensive vasomotion. *J Med Eng Technol*, 24(3), 95–101. 2000
[6] K. Jagomägi et al.: Effect of altering vasoactivity on the measurement of finger blood pressure. *Blood Pres Mon*, 6(1), 33–40. 2001
[7] J. Peňáz: Photoelectric Measurement of blood pressure, volume and flow in the finger. Digest of the 10th international conference on medical and biological engineering – Dresden (1973).
[8] DB. Wax et al.: Invasive and concomitant noninvasive intraoperative blood pressure monitoring: observed differences in measurements and associated therapeutic interventions. *Anesthesiology*, 2011; 115(5), 973–8.
[9] J Fortin, R. Grüllenberger: US 2011/0105918, May 5th 2011
[10] RD. Boehmer: Continuous, real-time, noninvasive monitor of blood pressure: Penaz methodology applied to the finger. *J Clin Monit.* 1987 Oct;3(4):282-7.
[11] J. Fortin et al.: Continuous non-invasive blood pressure monitoring using concentrically interlocking control loops. *Comput Biol Med* 36 941–957, 2006
[12] AM. Jagadeesh et al.: A comparison of a continuous noninvasive arterial pressure (CNAP) monitor with an invasive arterial blood pressure monitor in the cardiac surgical ICU. *Ann Card Anaesth*, 15(3), 180–4. 2012
[13] M. Neuner et al.: Clinical validation of a continuous non-invasive haemodynamic monitor (CNAP 500) during general anaesthesia. *Brit J Anaesth*, 2012 Apr;108(4):581-5.
[14] M. Biais et al.: Continuous non-invasive arterial pressure measurement: evaluation of CNAP device during vascular surgery. *Ann Fr Anesth*, 29(7-8), 530–5. 2010
[15] C. Ilies et al.: Investigation of the agreement of a continuous non-invasive arterial pressure device in comparison with invasive radial artery measurement. *Br J Anaesth*. 2012 Feb;108(2):202-10
[16] C. Jeleazcov et al: Precision and accuracy of a new device (CNAP) for continuous non-invasive arterial pressure monitoring: assessment during general anaesthesia. *Br J Anaesth*. 2010 Sep;105(3):264-72
[17] X. Monnet et al. Prediction of fluid responsiveness by a continuous non-invasive assessment of arterial pressure in critically ill patients: comparison with four other dynamic indices. *Br J Anaesth*. 2012 Sep;109(3):330-8
[18] M. Biais et al.: The ability of pulse pressure variations obtained with CNAP device to predict fluid responsiveness in the operating room. *Anesth Analg*. 2011 Sep;113(3):523-8

Biomed Tech 2013; 58 (Suppl. 1) © 2013 by Walter de Gruyter · Berlin · Boston. DOI 10.1515/bmt-2013-4180

TOCSY - Toolboxes for modelling of dynamical systems and time series

Wessel N[1], Marwan N[2], Krämer JF[1], Kurths J[1,2], et al.

[1]Department of Physics, Humboldt-Universität zu Berlin, Germany
[2]Transdisciplinary Concepts and Methods, Potsdam Institute for Climate Impact Research, Germany
tocsy@agnld.uni-potsdam.de

Abstract: *With Toolboxes for Complex Systems we provide a compilation of innovative methods for modern nonlinear data analysis and modelling. These methods were developed during scientific research in the Interdisciplinary Center for Dynamics of Complex Systems Potsdam, the Humboldt-Universität zu Berlin and the Potsdam Institute for Climate Impact Research (PIK). It provides analysis tools for recurrence quantification analysis, nonlinear regression analysis, innovative filtering and processing of physiological data, coupling direction estimations, wavelet spectrum and coherence analysis, time series graph estimation and more.*

Keywords: *nonlinear data analysis, modelling, coupling directions, recurrence plot, wavelets*

Introduction

The methods provided in TOCSY (**TO**olboxes for **C**omplex **Sy**stems) were developed during scientific research in the Interdisciplinary Center for Dynamics of Complex Systems Potsdam, the Humboldt-Universität zu Berlin and the Potsdam Institute for Climate Impact Research (PIK). The content is purely scientific and support may be provided by the respective authors. We ask you to cite the corresponding publication and the web site if you make use of our offer.

Methods

ACE – Nonlinear Regression Analysis
Voss H, Kurths J: Reconstruction of nonlinear time delay models from data by the use of optimal transformations, Phys. Lett. A, 234, 1997, 336-344.

Adaptive Filtering Procedure
Wessel N, Voss A, Malberg H, et al.: Nonlinear analysis of complex phenomena in cardiological data, Herzschr. Elektrophys., 11(3), 2000, 159-173.

COPRA – Constructing Proxy Records From Age Models
Breitenbach SFM, Rehfeld K, Goswami B, et al.: COnstructing Proxy Records from Age models (COPRA), Climate of the Past Discussion, 8, 2012, 2369-2408.

Commandline Recurrence Plots
Marwan N, Romano MC, Thiel M, Kurths J: Recurrence Plots for the Analysis of Complex Systems, Physics Reports, 438(5-6), 2007, 237-329.

Cross Recurrence Plot Toolbox
Marwan N, Wessel N, Meyerfeldt U, et al.: Recurrence Plot Based Measures of Complexity and its Application to Heart Rate Variability Data, Phys. Rev. E, 66(2), 2002, 026702.
Marwan N, Romano MC, Thiel M, et al.: Recurrence Plots for the Analysis of Complex Systems, Physics Reports, 438(5-6), 2007, 237-329.

Identification of Coupling Direction
Rosenblum MG, Cimponeriu L, Bezerianos A, et al.: Identification of coupling direction: Application to cardiorespiratory interaction, Phys. Rev. E, 65, 2002, 041909.

K2 - Dynamical Invariants by Recurrence Plots
Thiel M, Romano MC, Kurths J: Analytical Description of Recurrence Plots of white noise and chaotic processes, Applied Nonlinear Dynamics, 11(3), 2003, 20-30.

NEXCF - Cross-correlation estimates for non-equidistantly sampled time series
Rehfeld K, Marwan N, Heitzig J, et al.: Comparison of correlation analysis techniques for irregularly sampled time series, Nonlin. Proc. Geophys., 18(3), 389-404, 2011.

DS Prolog
Hübner S: Wissensbasierte Modellierung von Klassifikatoren für Zeit-Frequenz-Muster in PCM-Daten, Logos Verlag, Berlin, ISBN 978-3-8325-1596-6, 2007.

System Identification Tool
Sitz A, Schwarz U, Kurths , et al.: Estimation of parameters and unobserved components for nonlinear systems from noisy time series, Phys. Rev. E, 66, 2002, 016210.

TIGRAMITE - Time Series Graph and Momentary Information Transfer Estimation
Runge J, Heitzig J, Petoukhov V, et al.: Escaping the Curse of Dimensionality in Estimating Multivariate Transfer Entropy, Physical Review Letters, 108, 2012, 258701.

SOWAS – Wavelet Spectral and Coherence Analysis
Maraun D, Kurths J: Cross Wavelet Analysis. Significance Testing and Pitfalls, Nonlin. Proc. Geoph., 11, 2004, 505-514.

http://tocsy.pik-potsdam.de/index.php

Biomed Tech 2013; 58 (Suppl. 1) © 2013 by Walter de Gruyter · Berlin · Boston. DOI 10.1515/bmt-2013-4181

STIMFIT: A FAST VISUALIZATION AND ANALYSIS ENVIRONMENT FOR CELLULAR NEUROPHYSIOLOGY

Schlögl A[1], Jonas P[1], Schmidt-Hieber C[2,3] and Guzman SJ[1],

[1]Institute of Science and Technology (IST), Austria

[2]Wolfson Institute for Biomedical Research, University College London, London, UK

[3]Department of Neuroscience, Physiology and Pharmacology, University College London, London, UK.

alois.schloegl@ist.ac.at

Abstract: *Stimfit is a free cross-platform software package for viewing and analyzing electrophysiological data. It supports most standard file types for cellular neurophysiology and other biomedical formats. Its analysis algorithms have been used and validated in several experimental laboratories. Its embedded Python scripting interface makes Stimfit highly extensible and customizable.*

Keywords: *Electrophysiology, patch-clamp, data analysis, biomedical data formats, free software.*

Introduction

Electrical activity that arises from cellular and subcellular processes is commonly studied with intracellular techniques (e.g patch-clamp or sharp electrodes) in repetitive epoch-like events at high precision and temporal resolution. A detailed study of the acquired electrical signals generally requires both fast data visualization and ready access to complex analysis routines. We developed Stimfit[1], an open-source software package available for several operating systems, for fast and easy visualization of such recordings. Using the BioSig[2] library as an optional backend for file I/O [1], Stimfit supports more than 20 biomedical formats, including those most commonly used in cellular electrophysiology (see Table 1). It features robust algorithms for analysis in neurophysiology (e.g. calculations of synaptic and action potential latencies, rise and slope values, thresholds, etc.). These measurements are indicated to the user by a pair of cursors on the screen (see Figure 1) and are updated upon navigation along the recording. In addition, detection routines of spontaneous events are also provided [2, 3]. An implementation of the Levenberg-Marquardt algorithm [4] is used for fitting data to standard mathematical functions (single and multiexponentials) and common models in cellular neuroscience. Moreover, Stimfit is highly customizable with an embedded Python shell giving access to common scientific Python libraries such as NumPy or SciPy [5]. In summary, we present a cross-platform analysis environment that is easy to use and can be adapted to individual experimental requirements with Python [6].

[1]Stimfit is available on line from `http://www.stimfit.org`

[2]BioSig is available on line from `http://biosig.sourceforge.net/`

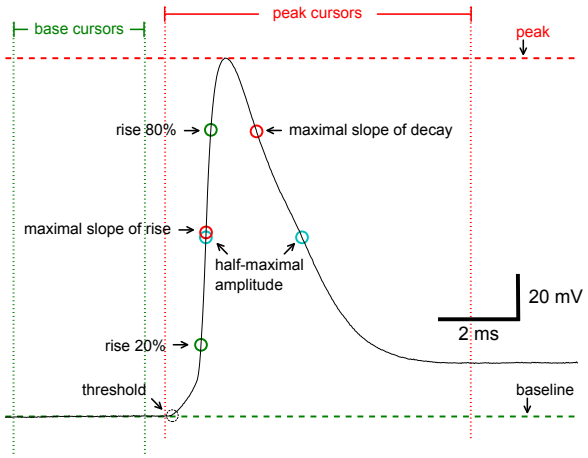

Figure 1: Principal measurements obtained when base and peak cursors are positioned on an action potential in a Stimfit session.

Table 1: File formats supported by Stimfit - only formats relevant for cellular electrophysiology are listed. (*) indicates support through biosig, (+) indicates improved support through biosig.

file type	read	write
Axon text	yes	yes
Axon binary v1	yes	no
Axon binary v2	yes	no
CFS binary	yes(+)	yes
HDF5 files	yes	yes
Axograph	yes	no
HEKA	yes(+)	no
Igor binary	yes(*)	yes
GDF	yes(*)	yes(*)
NEURON	yes(*)	no

Methods

Stimfit is written in C++ with some external libraries (see Table 2) and extensions in Python. To create the GUI, the wxWidgets library was chosen because it provides cross-platform support [7]. The BioSig library has recently been added to support additional biomedical data formats and the GDF file format [8]. The source code can be compiled with an ANSI/ISO C++ compliant compiler and has been tested with the GNU compiler for GNU/Linux, Mac OS

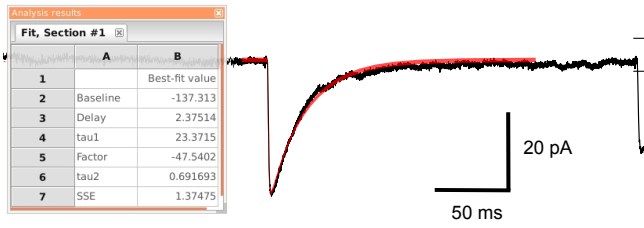

Figure 2: Fitting of an averaged excitatory postsynaptic current to a biexponential function by least-square optimization implementation in Stimfit.

Table 2: List of C++ external libraries.

library	purpose
BioSig	Biomedical file formats, input/output
boost	Shared pointers and arrays
FFTW	Fast Fourier transform for filtering
HDF5	Support to HDF5 file format
LAPACK	Linear algebra, non-linear regression
levmar	Non-linear regression
wxWidgets	Graphical user interface
Python	Python interpreter
wxPython	Embedded Python shell

X and with Microsoft Visual C++ 2008® for Microsoft® Windows. Alternatively, the the MinGW-cross-compiler environment (MXE) [9] tool-chain can be used for building the Windows version to avoid proprietary compilers. Some regressions when using MXE, such as missing Python and ABF support, will eventually be fixed in future releases.

Fast visualization by avoiding line plot redundancies
To efficiently plot data obtained at high sampling rates, two algorithms are employed. A down-sampling algorithm is used to reduce the number of lines plotted between two pixel columns by choosing the maximum and minimum sampling value within a column and plotting one single line between them. An anti-aliasing algorithm is used to connect pixel columns.

Event detection and fitting algorithms
Spontaneous or miniature synaptic events can be detected by minimizing the sum of squared errors between a template waveform and recording periods. To decide whether an event has occurred, the user can choose between two criteria: either the correlation coefficient between optimal template and recording [3], or the ratio of template scaling factor and noise standard deviation [2].

Python integration
To provide a customizable analysis platform, Stimfit includes a command-line Python interface to control the GUI and access the analysis algorithms. In addition, the Python shell gives access to the extensive ecosystem of scientific libraries that are available for Python, such as NumPy or SciPy. In addition, a stand-alone Python module (stfio) allows users to read and write standard electrophysiology file formats from Python without the Stimfit GUI.

Discussion

Robust algorithms for visualization and analysis are necessary for our understanding of the electrical signals in neuroscience. A free software model facilitates reproducibility, one of the cornerstones of scientific progress. For that reason, Stimfit is released under the GNU general public license (GPL), and all its libraries and dependencies are released under free software licenses. Among all programming languages under the GPL license, Python was chosen as a scripting language for Stimfit because of its widespread use in neuroscience [10]. Thus, as an alternative to proprietary software solutions, Stimfit combines an intuitive user interface with a general-purpose programable environment.

Bibliography

[1] C. Vidaurre, T. H. Sander, and A. Schlögl, "BioSig: The free and open source software library for biomedical signal processing," *Computational intelligence and neuroscience*, vol. 2011, p. 12 pages, 2011.

[2] J. D. Clements and J. M. Bekkers, "Detection of spontaneous synaptic events with an optimally scaled template.," *Biophys J*, vol. 73, pp. 220–229, Jul 1997.

[3] P. Jonas, G. Major, and B. Sakmann, "Quantal components of unitary EPSCs at the mossy fibre synapse on CA3 pyramidal cells of rat hippocampus.," *J. Physiol.*, vol. 472, pp. 615–663, Dec 1993.

[4] M. Lourakis, "levmar: Levenberg-marquardt nonlinear least squares algorithms in C/C++." [web page] `http://www.ics.forth.gr/~lourakis/levmar/`, Jul. 2004. [Accessed on 13 Mar. 2013.].

[5] T. E. Oliphant, "Python for scientific computing," *Computing in Science Engineering*, vol. 9, no. 3, pp. 10–20, 2007.

[6] G. van Rossum, "The python programming language," *Python Software Foundation*, 2007.

[7] J. Smart, K. Hock, and S. Csomor, *Cross-Platform GUI Programming with wxWidgets (Bruce Perens Open Source)*. Upper Saddle River, NJ, USA: Prentice Hall PTR, 2005.

[8] A. Schlögl, "GDF - a general dataformat for biosignals." [web page] `http://arxiv.org/abs/cs/0608052`, 2006. [Accessed on 13 Mar. 2013.].

[9] V. Grabsch, "Mingw-cross-compiler environment." [web page] `http://mxe.cc`, 2007-2013. [Accessed on 13 Mar. 2013.].

[10] A. P. Davison, M. L. Hines, and E. Muller, "Trends in programming languages for neuroscience simulations.," *Front Neurosci*, vol. 3, no. 3, pp. 374–380, 2009.

Biomed Tech 2013; 58 (Suppl. 1) © 2013 by Walter de Gruyter · Berlin · Boston. DOI 10.1515/bmt-2013-4182

EEGLAB – AN OPEN SOURCE MATLAB TOOLBOX FOR ELECTROPHYSIOLOGICAL RESEARCH

Clemens Brunner[1], Arnaud Delorme[2] and Scott Makeig[2]

[1]Institute for Knowledge Discovery, Graz University of Technology, Austria

[2]Swartz Center for Computational Neuroscience, Institute for Neural Computation, University of California San Diego, CA, USA

clemens.brunner@tugraz.at

Abstract: *EEGLAB is a widely used open-source MATLAB toolbox for analysis of electrophysiological data. Using EEGLAB, users can import various data formats, preprocess data (filter, resample, average, epoch), visualize data (signal browser, event-related potentials, power spectra), perform independent component analysis (ICA), use various time/frequency analysis methods such as event-related spectral perturbation (ERSP) and inter-trial coherence (ITC). The extensible plug-in architecture enables third parties to contribute additional functionality such as source localization, connectivity estimation or the design of online brain-computer interfaces.*

Keywords: *Biosignal analysis, MATLAB, software, open source, GPL*

Introduction

The EEGLAB signal processing environment, an open source software project of the Swartz Center for Computational Neuroscience (SCCN) of the University of California San Diego (UCSD), began as a set of electroencephalogram (EEG) data analysis tools for MATLAB (The Mathworks, Inc.). These tools were made publicly available by Scott Makeig in 1997, which evolved into EEGLAB, which was first released with a coherent structure and graphical user interface in 2001. More than ten years later, the EEGLAB reference paper [1] has over 2,500 citations, the opt-in EEGLAB discussion email list links over 6,500 researchers, the EEGLAB news list has over 10,000 subscribed researchers, and a recent survey of 687 research respondents has reported EEGLAB to be the software environment most widely used for electrophysiological data analysis. In addition, at least 35 EEGLAB plug-in tools have now been released by researchers from many laboratories. EEGLAB is now a de facto standard supporting a wide range of EEG and other electrophysiological research studies with contributions from many researchers.

Data import and preprocessing

EEGLAB supports importing numerous different data formats such as ASCII, MATLAB, BCI2000, Neuroscan, Biosemi, ANT EEProbe, and BrainVision. In addition, EEGLAB includes some functions from BioSig[1] and FieldTrip[2] that together provide support for many other data formats.

Standard preprocessing methods available in EEGLAB include filters (FIR and IIR), epoch extraction, baseline removal, resampling, and re-referencing. Furthermore, data channels can be deleted or interpolated, and artifacts can be removed using fully- or partially-automated methods (based on channels or epochs).

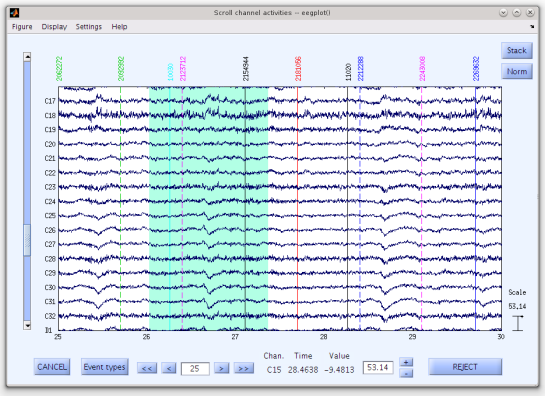

Figure 1: Signal browser showing 17 EEG channels with colored event markers, control buttons, and a selected segment (green background between 26–27.4 s).

Data visualization

Data can be visualized in a scrollable interactive view which displays a specific number of channels in a specific time range. Figure 1 shows this channel activities window with event markers and a custom selection. This visualization is particularly useful for manual artifact rejection, where the user selects signal segments by clicking and dragging with the mouse.

Independent component analysis (ICA)

A particular strength of EEGLAB is its seamless integration of independent component analysis (ICA). ICA algorithms can be used to detect and isolate stereotypical artifacts (such as eye movements and electrocardiographic signals) mixed by volume conduction in EEG recordings. Fur-

[1]biosig.sourceforge.net

[2]fieldtrip.fcdonders.nl

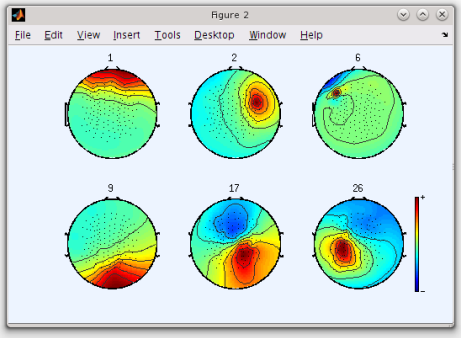

Figure 2: Scalp maps for six independent components from a 128-channel decomposition.

thermore, ICA algorithms are capable of separating biologically plausible dipolar brain sources. The default ICA algorithm available in EEGLAB is extended Infomax [2], but other algorithms including JADE[3], FastICA[4], and AMICA[5] are also available in the core EEGLAB distribution or as plug-ins. Most visualization functions and processing tools are available for both channel and component data (for example, ERP plotting, time/frequency plots, power spectra, artifact rejection, data visualization), so it is straightforward to work with either or both signal types. Figure 2 shows scalp maps of selected independent components. Dipole source localization of such maps is possible using DIPFIT2 (included) or the NFT[6] [3] toolbox.

Time/frequency analysis

EEGLAB supports time/frequency analysis measures such as (baseline or averaged) power spectrum, event-related spectral perturbation (ERSP), inter-trial coherence (ITC), and event-related cross-coherence. The SIFT[7] toolbox offers a wide range of additional connectivity measures.
ERSP visualizes event-related changes in the averaged power spectrum in a broad frequency range relative to a baseline interval. ITC measures the amount of event-related phase-locked activity as a function of time and frequency, whereas ERCOH calculates event-related coherence between two signals.

User interface

EEGLAB features a graphical user interface (GUI) useful for new users and for exploring new data. However, all functions are also accessible via the command line at two different levels: (1) so-called pop functions are the basis of all GUI functionality and are also available through EEGLAB's command history, and (2) low-level functions and data structures. MATLAB scripting is fully supported.

[3] bsp.teithe.gr/members/downloads/Jade
[4] research.ics.aalto.fi/ica/fastica/
[5] sccn.ucsd.edu/~jason/amica_web.html
[6] sccn.ucsd.edu/wiki/NFT
[7] sccn.ucsd.edu/wiki/SIFT

Documentation and support

EEGLAB is distributed under the GNU General Public License, the complete source code is publicly available.
EEGLAB is based on (and therefore requires) the commercial MATLAB software environment (version 7 or higher). However, all dependencies on additional MATLAB toolboxes have been removed from the core EEGLAB distribution (some advanced EEGLAB plug-ins may still require specific MATLAB toolboxes).
Most EEGLAB functions also run under Octave, an open source software environment compatible with MATLAB. However, graphical output might not be fully functional.
EEGLAB documentation is freely available on the web[8], featuring a hands-on tutorial, an online workshop, a wiki, frequently asked questions (FAQ), a bug report interface, mailing lists for news and discussions, and a support email account (these email addresses can be found on the EEGLAB website).

Discussion

The functionality of EEGLAB can be extended with plug-ins. Currently, the community has contributed around 35 EEGLAB plug-ins, ten of which are included in the core EEGLAB distribution (for example, DIPFIT2 from FieldTrip, BioSig data import, IIRfilt, and LORETA[9]).
Future development of EEGLAB will focus on supporting, maintaining, and integrating important plug-ins. Major examples include the in-house developed toolboxes BCILAB, SIFT, MPT, NFT, and MoBILAB [3]. EEGLAB core tools will be strengthened (including improved source localization, a wider range of ICA and beamforming algorithms, and support for computations on high-performance clusters, GPUs, and the cloud). Finally, a new web infrastructure will be developed (including a new software hosting facility and a comprehensive community website featuring more extensive documentation and tutorials).

Bibliography

[1] A. Delorme and S. Makeig, "EEGLAB: an open source toolbox for analysis of single-trial EEG dynamics including independent component analysis," *Journal of Neuroscience Methods*, vol. 134, no. 1, pp. 9–21, 2004.

[2] A. J. Bell and T. J. Sejnowski, "An information-maximization approach to blind separation and blind deconvolution," *Neural Computation*, vol. 7, no. 6, pp. 1129–1159, 1995.

[3] A. Delorme, T. Mullen, C. Kothe, Z. Akalin Acar, N. Bigdely-Shamlo, A. Vankov, and S. Makeig, "EEGLAB, SIFT, NFT, BCILAB, and ERICA: new tools for advanced EEG processing," *Computational Intelligence and Neuroscience*, vol. 2011, p. 130714, 2011.

[8] sccn.ucsd.edu/wiki/EEGLAB
[9] www.uzh.ch/keyinst/loreta.htm

Biomed Tech 2013; 58 (Suppl. 1) © 2013 by Walter de Gruyter · Berlin · Boston. DOI 10.1515/bmt-2013-4183

OPENWALNUT: AN OPEN-SOURCE TOOL FOR VISUALIZATION OF MEDICAL AND BIO-SIGNAL DATA.

Sebastian Eichelbaum[1], Mario Hlawitschka[2], Gerik Scheuermann[1],

[1]Abteilung für Bild- und Signalverarbeitung, Universität Leipzig, Germany

[2]Lehrstuhl für Wissenschaftliche Visualisierung, Universität Leipzig, Germany

eichelbaum@informatik.uni-leipzig.de

Abstract: *The number of medical imaging modalities and bio-signal acquisition methods has increased dramatically in the last years. Each is designed to answer a certain set of questions or to explore certain features of living tissue. With visualization, it is possible to combine these different types of images and data to grasp their meaning in the context of each other. Unfortunately, many existing visualization tools are focused on certain modalities and signals. With OpenWalnut, we provide a tool which is designed to be used with different signals and modalities in combination with each other. It aims at providing interactive rendering and explorability with a clean data-flow-based interface. The project is open-source and well documented and has yet been extended and used by many groups and researchers. In this short-paper, we provide a coarse overview of the principles and focus-points of OpenWalnut.*

Keywords: *visualization, medical data, bio-signals, open-source, software*

Introduction

In the course of the ongoing research into neurological diseases and the function and anatomy of the brain, a large variety of examination techniques has evolved. The different techniques aim at findings for different research questions or different viewpoints of a single task.

Considering the different applications, it is evident that for many research areas only a combination of these techniques can help answering the posed questions. To name only one example, the combination of diffusion-weighted MRI and functional MRI with an anatomical context provided by T1 MRI images is very common.

To be able to analyze the data measured by the different techniques, a tool that can efficiently visualize the different modalities simultaneously is needed. The software (called *OpenWalnut*) we will present in this work aims at exactly this task. It does not only allow to display the different modalities together, but also provides tools to analyze their interdependence and relations.

In the following, we will point out the focus-points of OpenWalnut and its basic working principles.

Focus and Reasoning

As mentioned above, it is very crucial to handle a multitude of different kinds of images and signals. Besides this, there are several other criteria for visualization software, especially in a scientific environment, which is our target group of users. There are many visualization tools available which have their specific strengths and weaknesses ([1, 2, 3, 4, 5, 6]), but none of them where able to completely fulfill our criteria. In this section, we point out these criteria, building the fundamentals of OpenWalnut's software design and implementation.

Open Source: In a scientific environment, it is very important to be able to re-produce results of other researchers and to comprehend algorithms of others. With the help of open-source software, this can be achieved. It provides a possibility to share algorithms and calculation pipelines with others in a common framework. Besides this, an open-source framework allows for easy extension and adaption of existing methods to new problems. Thus, OpenWalnut is developed as free and open software to allow us and others to work on a common framework.

General Purpose and Extensible: Very focused software is not able to handle the above mentioned multitude of signal and image modalities. Additionally, in a research environment, it is very often required to find new ways of solving a certain medical or neurological problem. To achieve this, the used software must not limit the researcher in terms of applicability of algorithms and in terms of easy programmatic extensibility. OpenWalnut is two things in this context: (1) a powerful visualization tool and (2) a powerful programming framework which provides maximum flexibility to the researcher. We even allow interfacing OpenWalnut with the famous script language Python.

Re-using existing Tools: There are a lot of very powerful tools and frameworks available for very different tasks. To utilize certain strengths of these toolkits, a software needs to interact with them instead of re-inventing them. OpenWalnut integrates several well-know toolkits like Eigen [7] and OpenSceneGraph [8] and interfaces other tools more indirectly, like FSL [9], teem [10], BioSig [11], NIfTI [12] or, due to our Python bindings, numPy [13], and NiBabel [14]. This way, we make OpenWalnut even more extensible and flexible.

Graphical User Interface: Most software aims either at the visualization researcher or the neuro-scientist, with accordingly designed GUIs. OpenWalnut aims at both groups. The neuro-scientist, who needs a usable tool to handle and visualize its data and the visualization researcher, who needs a powerful, programmable tool and flexible user interface. To achieve this ambitious goal, OpenWalnut focuses on a clean and straight interface, which is centered

around a data-flow network as shown in Figure 1. The principle of using a data-flow networks is very common to many image/signal processing tools, visualization tools and even programming frameworks [15]. We avoid complex and complicated GUI dialogs for algorithms, provide useful default values for all parameters, direct and visual feedback for parameter changes and allow to combine complex data pipelines into containers, to hide their complexity. **Availability:** The hurdle of using software which is not available on your machine or operating system or which needs to be compiled tediously for your system is very hight. Thus, OpenWalnut focuses on portability and availability. We focus the three major operating systems in use today (Linux, Windows and Mac OS) and provide pre-compiled and packaged versions of OpenWalnut for them. This makes OpenWalnut available for most of the researchers directly.

Results and Conclusion

In the last section we gave a short insight into the criteria that have driven and still drive the development of OpenWalnut. Although there are many tools available for handling and visualizing medical images and bio-signal data, each has its advantages and disadvantages. We do not try to re-invent the wheel, nor do we claim our project is superior to the others. We created a tool which complies to a certain set of criteria and tries to re-use as many as possible of existing tools and frameworks. We have targeted OpenWalnut at researchers in the medical and neuroscientific field and provide them with an open and powerful tool to explore their data or to create new ways of visualizing them. The software is available at `http://www.openwalnut.org`.

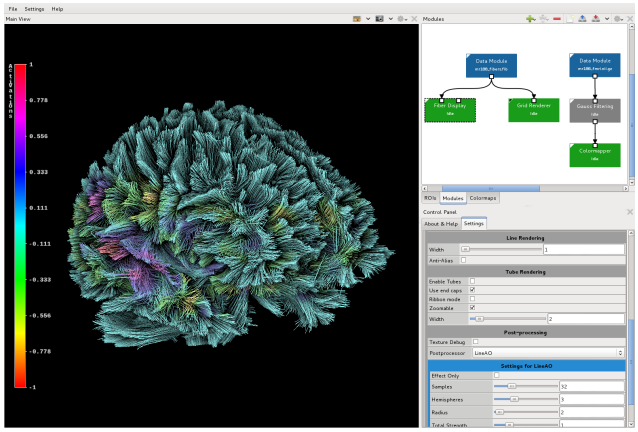

Figure 1: The GUI of OpenWalnut. On The right, you see the data-flow network and the properties (parameters) of the module "Fiber Display". You can also see the tool-buttons in the title-bar of each dock. We strictly provide options and operations only where they can be applied, making the GUI more structured. The left part of the GUI contains the final rendering of fiber tractography data in combination with FMRI activations, improved with the LineAO algorithm [16]

Bibliography

[1] "Amira - visualize analyze present." http://www.amira.com/.

[2] "MeVisLab: development environment for medical image processing and visualization." http://www.mevislab.de/.

[3] "Medinria: Medical image navigation and research tool by inria." http://www-sop.inria.fr/asclepios/software/MedINRIA/.

[4] "SCIRun: A scientific computing problem solving environment, scientific computing and imaging institute (SCI)." http://www.scirun.org.

[5] J. Ahrens, B. Geveci, and C. Law, "Paraview: An end-user tool for large data visualization," in *Visualization Handbook* (C. Hansen and C. Johnson, eds.), Elsevier, 2005.

[6] W. Benger, G. Ritter, and R. Heinzl, "The concepts of vish," in 4^{th} *High-End Visualization Workshop, Obergurgl, Tyrol, Austria, June 18-21, 2007*, pp. 26–39, Berlin, Lehmanns Media-LOB.de, 2007.

[7] "Eigen: a c++ template library for linear algebra: matrices, vectors, numerical solvers, and related algorithms." http://eigen.tuxfamily.org/.

[8] "OpenSceneGraph: an open source high performance 3d graphics toolkit." http://www.openscenegraph.org/.

[9] "FMRIB software library." http://www.fmrib.ox.ac.uk/fsl/.

[10] "Teem: Tools to process and visualize scientific data and images." http://teem.sourceforge.net/.

[11] "BioSig: an open source software library for biomedical signal processing." http://biosig.sourceforge.net/.

[12] "NIfTI: Neuroimaging informatics technology initiative." http://nifti.nimh.nih.gov/.

[13] "numPy: Scientific computing tools for python." http://www.numpy.org/.

[14] "NiBabel: Access a cacophony of neuro-imaging file formats." http://nipy.sourceforge.net/nibabel/.

[15] "VTK visualization toolkit." http://www.vtk.org/.

[16] S. Eichelbaum, M. Hlawitschka, and G. Scheuermann, "LineAO — improved three-dimensional line rendering," *IEEE Transactions on Visualization and Computer Graphics*, vol. 19, pp. 433–445, March 2013.

Biomed Tech 2013; 58 (Suppl. 1) © 2013 by Walter de Gruyter · Berlin · Boston. DOI 10.1515/bmt-2013-4184

MNE-X: MEG/EEG REAL-TIME ACQUISITION, REAL-TIME PROCESSING, AND REAL-TIME SOURCE LOCALIZATION FRAMEWORK

Christoph Dinh[1,2], Martin Luessi[1], Limin Sun[1], Jens Haueisen[2,3] and Matti S Hamalainen[1]

[1]Athinoula A. Martinos Center for Biomedical Imaging, Massachusetts General Hospital - Massachusetts Institute of Technology - Harvard Medical School, United States

[2]Institute of Biomedical Engineering and Informatics, Ilmenau University of Technology, Germany

[3]Biomagnetic Center, Department of Neurology, University Hospital Jena, Germany

chdinh@nmr.mgh.harvard.edu

Abstract: *Providing millisecond-temporal resolution for non-invasive mapping of human brain functions, Magneto-/Electroencephalography (MEG/EEG) is predestined to monitor brain activity in real-time. While data analysis to date is mostly done subsequent to the acquistion process we introduce here an acquisition and real-time analysis application. Online feedback allows the adaption of the experiment to the subject's reaction creating a whole set of new options and increasing time efficiency by shortening acquisition and offline analysis. To build a standalone application, we first designed MNE-CPP a cross-platform open source Qt5 C++ library, which implements the validated parts of our scripting toolboxes MNE-Python/MATLAB. Based on MNE-CPP we built MNE-X, which allows real-time acquisition, processing, and source localization.*

Keywords: *Real-Time, Magnetoencephalography, Electroencephalography, Processing, Source Localization*

Introduction

Real-time processing and source localization for MEG/EEG enables possibilities for novel experimental paradigms and improves the efficacy of these methods in clinical diagnosis where fast analysis procedures are essential. Given that some information is processed during the acqusition, the subsequent off-line analysis will be facilitated and made faster. Such a real-time MEG/EEG monitor has to be able to control the MEG/EEG hardware to acquire data, as well as to be capable of processing the acquired data online. Several application frameworks [1, 2] to acquire as well as scripting toolboxes [2, 3, 4] to analyse MEG/EEG data already exist. For designing a standalone acquisition and processing application, such as MNE-X, it is necessary to have a highly flexible library which unites the acquisition and the analysis. Here we want to introduce MNE-CPP, our new cross-platform opensource Qt5 C++/CUDA library package. MNE-CPP is designed as a basis for standalone applications and enables the application programmer to make full use of the given hardware capabilities and develop processing pipelines with almost the ease of a scripting toolbox. MNE-CPP is part of the MNE-Suite and can be freely accessed at:

`https://github.com/mne-tools`

Methods

MNE-CPP is a derivative of our scripting toolboxes MNE-Python/MNE-MATLAB and consists of several sub-libraries (Fig. 1). Except of the inverse sub-library, MNE-CPP only depends on Qt5 [5] and the light-weight Eigen [6] template library for linear algebra. This enables the user to build MEG/EEG applications for almost any computational device. PCs, tablets, smartphones and even embedded solutions are supported.

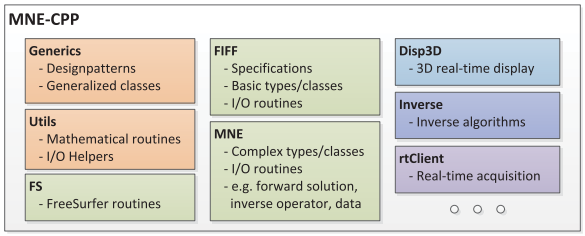

Figure 1: Sub-libraries of MNE-CPP: helpers (orange), core (green), specific tasks (blue to violet)

Besides the C++ implementation, the inverse library provides a GPU CUDA kernel for some algorithms, and relies if GPU computing is wanted on NVDIAs nvcc compiler.

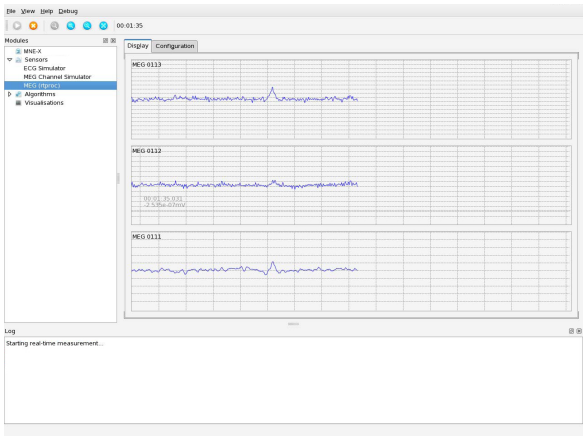

Figure 2: User interface of MNE-X

MNE-X (Fig. 2) is built based on MNE-CPP. It is designed for the daily clinical use and comes with several real-time plug-ins, e.g. the averaging, source localization, and frequency estimation toolboxes. Also the development of further plug-ins, e.g., real-time Signal Source Separation (SSS)/ Signal Space Projection (SSP), is already in progress.

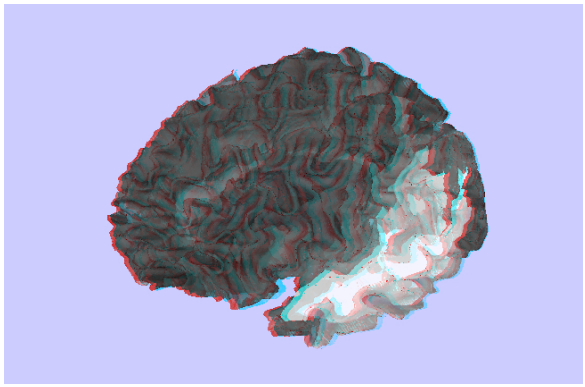

Figure 3: Screenshot of the real-time stereoscopic 3D (anaglyph red/cyan) source localization monitor. The display shows the localization of an auditory stimulus with an applied moving average.

Here we also want to introduce our online source localization toolbox, which, in addition to the localization algorithms, provides a real-time 3D stereoscopic display (fig. 3)). The applied algorithm uses a region-of-interest forward solution clustering and an adapted MNE [7] algorithm.

Results

MNE-X is able to control the MEG/EEG hardware to acquire data. It also provides fast and effective algorithms to process the acquired data online. It is designed as a cross-platform opensource application and introduces a new plug-in framework to easily adapt and extend the MEG/EEG online analyzation capabilities. To realize MNE-X we designed in a highly portable MNE-CPP library.

Discussion

By providing online feedback and increasing time efficiency, MNE-X aims to improve the clinical value of MEG/EEG by providing new experiment options and integragting them into fast diagnostic procedures. However, more work is needed to address, e.g., the accuracy of online source localization. Clinical and basic research studies are needed to assess the benefits of MNE-X and to guide its further development.

Bibliography

[1] G. Schalk, D. McFarland, T. Hinterberger, N. Birbaumer, and J. Wolpaw, "Bci2000: a general-purpose brain-computer interface (bci) system," *Biomedical Engineering, IEEE Transactions on*, vol. 51, no. 6, pp. 1034–1043, 2004.

[2] R. Oostenveld, P. Fries, E. Maris, and J.-M. Schoffelen, "Fieldtrip: Open source software for advanced analysis of meg, eeg, and invasive electrophysiological data," *Computational Intelligence & Neuroscience*, p. 156869 (9 pp.), 2011 2011.

[3] A. Delorme and S. Makeig, "Eeglab: an open source toolbox for analysis of single-trial eeg dynamics including independent component analysis," *Journal of Neuroscience Methods*, vol. 134, no. 1, pp. 9–21, 2004.

[4] F. Tadel, S. Baillet, J. C. Mosher, D. Pantazis, and R. M. Leahy, "Brainstorm: A user-friendly application for meg/eeg analysis," *Computational Intelligence & Neuroscience*, p. 879716 (13 pp.), 2011 2011.

[5] Qt project authors, "Qt5 cross-platform application and ui framework," 2013.

[6] Eigen authors, "Eigen 3 c++ template library," 2012.

[7] M. S. Hamalainen and R. Ilmoniemi, "Interpreting magnetic fields of the brain: minimum norm estimates," *Medical & Biological Engineering & Computing*, vol. 32, no. 1, pp. 35–42, 1994.

Biomed Tech 2013; 58 (Suppl. 1) © 2013 by Walter de Gruyter · Berlin · Boston. DOI 10.1515/bmt-2013-4185

PANEL DISCUSSION: INTEROPERABILITY OF TOOLBOXES – A USEFUL SECOND LEVEL AIM ?

Sander T

Biosignals, Physikalisch-Technische Bundesanstalt, Germany

Tilmann.sander-thoemmes@ptb.de

Abstract: *Free software is an important tool in biosignal processing. The integration of several free toolboxes (FTB) for a data analysis task beyond the scope of a single FTB is a multiplier of the time and cost saving effects of a single FTB. Open questions in relation to interoperability shall be discussed.*

Keywords: *free software, toolbox, interoperability, biosignal processing*

Introduction

With the advent of powerful computers and microcontrollers digital biosignal processing has become a ubiquitous ingredient in biomedical engineering. A multitude of highly specialized analysis methods and complex processing chains have been developed. It is highly inefficient if methods or algorithms are coded from scratch for a research project. Therefore the biosignal research community has followed the "Linux" or free software paradigm, i.e. the source code of the software must be accessible, and it is allowed to modify (expand) and redistribute the software. These principles are very similar to the scientific process, where the next research steps are based on published previous research results. Despite the purely scientific benefit free toolboxes (FTB) are of interest for industry to be able to evaluate a wide range of algorithms rapidly.

Results

Many reusable FTBs have been developed (e.g. see [1,2] for exemplary collections). Reusability relies on several requirements: The FTB is well maintained and easily accessible; it has a bug reporting system and a reasonably fast bug resolution chain; a help system; etc. As with scientific results proper credit needs to be given to FTB developers.

A second level of reusability is achieved if FTBs can interact with each other or if at least a defined data exchange procedure exists. Examples for interoperability are given in Fig. 1. In a) FieldTrip [1] has an external directory containing the complete Biosig code. If a file-input-output (fileio) operation reads data in a format supported by the Biosig, then FieldTrip branches to the external/biosig directory to call a native Biosig function. In b) an example for an even closer integration is given, where SPM8 [1] incorporates lower level FieldTrip directories to rely solely on FieldTrip functionality for certain types of operation.

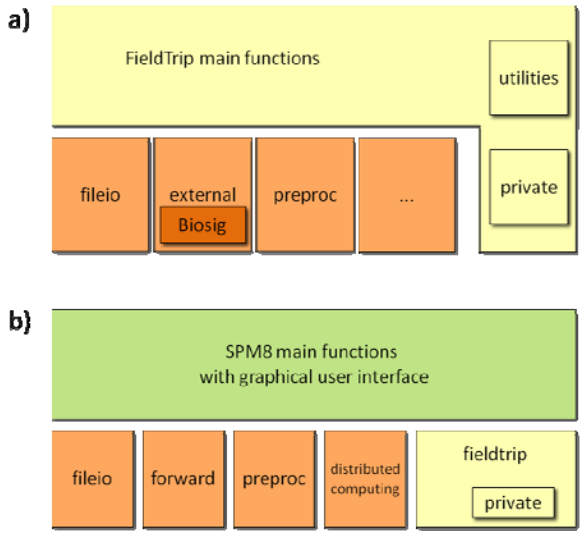

Figure 1: Examples for FTB interoperability (adapted from FieldTrip introductory material). a) FieldTrip uses the Biosig to read data in various formats. b) SPM integrates functional directories of FieldTrip for certain tasks.

Discussion

How does the hierarchical structure in Fig. 1 compare to a flat linear processing chain of FTBs ? Should data exchange be managed either by a data structure within a programming language or by storing the data in a common file format ? What would motivate developers to support interoperability as a community goal ? How to improve the credit or citation system for processing chains of several FTBs ?

Acknowledgement

Helpful discussions with V. Litvak, R. Oostenveld, A. Schlögl, U. Steinhoff, and C. Wolters are gratefully acknowledged.

Bibliography

[1] Academic Software Applications for Electromagnetic Brain Mapping Using MEG and EEG. Baillet S, Friston K, Oostenveld R, Eds. Computational Intelligence and Neuroscience 2011, ID 972050.

[2] Python in neuroscience (I and II). Gewaltig M-O et al., Eds. Frontiers in Neuroinformatics 2008-2013

Biomed Tech 2013; 58 (Suppl. 1) © 2013 by Walter de Gruyter · Berlin · Boston. DOI 10.1515/bmt-2013-4186

EEG MEASURES INDICATING ANAESTHESIA INDUCED CHANGES OF CORTICAL INFORMATION PROCESSING

Jordan D[1], Ilg R[2], Schneider G[1,3], Stockmanns G[4], Kochs EF[1]

[1]Department of Anaesthesiology, Klinikum rechts der Isar, Technische Universität München, Germany
[2]Department of Neurology, Klinikum rechts der Isar, Technische Universität München, Germany
[3]Department of Anaesthesiology, Witten/Herdecke University, HELIOS Clinic Wuppertal, Germany
[4]Hochschule Niederrhein, FB Elektrotechnik und Informatik, Krefeld, Germany

d.jordan@lrz.tum.de

Abstract: *Consciousness is related to the brains ability to process information. This is inline with EEG studies observing decreased signal "complexity" under anaesthesia induced unconsciousness. In the present investigation, 64-channel electroencephalogram (EEG) of 15 volunteers was analyzed during consciousness, propofol induced sedation and unconsciousness. Univariate EEG parameters (spectral power, Higuchi fractal dimension, permutation entropy) and cortico-cortical information exchange in EEG based on symbolic transfer entropy (STE) were analysed to indicate effects of anaesthetics on the systemic information processing of the brain. The STE revealed affected interaction between frontal and parietal brain regions during unconsciousness.*

Keywords: *Electroencephalogram, consciousness, anaesthesia, propofol, entropy*

Introduction

Information processing in the human brain is an active field of research and is investigated with respect to specific paradigms [1]. It has been suggested that unconsciousness results from an impaired ability of the brain to integrate information. Functional magnetic resonance imaging (fMRI) studies on the effects of anaesthesia induced sedation and unconsciousness on the functional connectivity (FC) of the resting brain reported a disintegration of higher cortical networks [2]. Further, electroencephalographic (EEG) studies indicated an uncoupling of electrical coherence or suppression of long-range synchronization during unconsciousness when compared to wakefulness [3]. Beyond classical spectral power analyses of the EEG, new techniques were introduced to quantify the content of processed information. Approaches include state space methods such as fractal dimensions and information theoretic methods based on entropy analysis [4]. More recently, asymmetric multivariate analysis has facilitated the detection of directional interdependences from time series. Within the framework of ordinal signal analysis, symbolic transfer entropy (STE) was introduced to distinguish driving and responding subsystems in complex non-linear dynamics and to detect asymmetry in their mutual interaction [5]. STE combines advantages of a stringent concept to infer the direction of interactions with robustness and performance of non-linear symbolic analysis. In contrast to the univariate EEG permutation entropy (PE) [6], which has been suggested as reliable non parametric measure of anaesthetic depth [7], STE may more specifically indicate effects of anaesthetics on the systemic information processing level of the brain. In the present investigation, the ability of STE to quantify cortical processing in EEG during consciousness, propofol sedation and unconsciousness was evaluated.

Methods

Approved by the local ethics committee, 15 male volunteers (age 21-32 years) were enrolled into the study. After a resting period, volunteers were instructed to relax and close their eyes while 64-channel EEG recordings were performed under three conditions: After 15 minutes baseline (BL condition) recordings, propofol was infused until loss of consciousness (LOC) using a target controlled infusion (TCI) pump (Open TCI, Braun Medical, Melsungen, Germany). TCI concentrations were maintained stable for 15 minutes (LOC condition). After that, a phase of sedation was maintained during another 15 minutes at 50% of the initial LOC concentration (0.5LOC condition). Standard monitoring parameters (electrocardiogram (ECG), blood pressure, respiratory frequency, pulse oxymetry) were continuously measured with a Datex anaesthesia monitor (Datex-Ohmeda Division Instrumentation Corp., Helsinki, Finland) and recorded together with TCI concentrations. EEG recordings were performed using a 64-channel electrode cap with equidistant electrodes (Easycap, Herrsching, Germany) and two 32-channel EEG amplifiers (Brain Products, Gilching, Germany). Basic artefact rejection (EEG with amplitudes exceeding 250μV), average reference and independent component analysis for blind source separation of non cortical signal components were performed.

In the present study power spectral density in θ- (4-8Hz), α- (8-12Hz) and β-band (12-30Hz), Higuchi's fractal dimension (HD) [4], PE (dimension m = 5) [6] and STE [5] were analysed on all EEG channels at the end of the three conditions BL, 0.5LOC and LOC (signals of 10s length, zero phase digital filtered with 0.5-30Hz bandwidth, 200Hz sampling frequency). STE indicates information flow from system Y (time series y of length N) to system X (time series x of length N) through

$$\mathrm{STE}_{Y\to X} = \sum p(\hat{x}_i, \hat{x}_{i-\delta}, \hat{y}_{i-\delta}) \log_2 \left(\frac{p(\hat{x}_i | \hat{x}_{i-\delta}, \hat{y}_{i-\delta})}{p(\hat{x}_i | x_{i-\delta})} \right). \quad (1)$$

Therefore, amplitude orders $\hat{x}_i, \hat{y}_i$ of sequences $x_i = \{x(i), x(i+l), \ldots, x(i+(m-1)l\}$ and y_i along x, y ($i \in \{1, \ldots, N-(m-1)l\}$) are analyzed with respect to embedding parameters m (dimension) and l (time lag). $p(A|B)$ is the conditional probability that A occurs under condition B, $p(A,B)$ is the joint probability of A and B. The directionality index denoted by STE quantifies the preferred direction of flow between systems X and Y, i.e.

$$\mathrm{STE} = \mathrm{STE}_{X\to Y} - \mathrm{STE}_{Y\to X}. \qquad (2)$$

STE is expected to attain positive values for unidirectional coupling with X as the driver and negative values for Y driving X. Assuming $\mathrm{STE}_{X\to Y}, \mathrm{STE}_{Y\to X} > 0$, a value STE = 0 indicates balanced bidirectional coupling. STE was computed in all EEG channel pair combinations using a dimension m = 5 and a transfer delay δ = 35-50 ms mainly reflecting cortico-cortical information transfer in the EEG β-band [1].

Discrimination of Pθ, Pα, Pβ, HD, PE and STE between BL, 0.5LOC (consciousness) and LOC (unconsciousness) was evaluated using the area under the receiver characteristic curve (AUC) and 95% percentile bootstrap confidence intervals (CI) at a corrected threshold of $p < 0.05$ Therefore, parameters were averaged in frontal, parietal, temporal and occipital EEG electrodes.

Results

Fig. 1 shows value distribution of Pθ, Pα, Pβ, HD, PE and STE at (A) BL, (B) 0.5LOC and (C) LOC. Only results of frontal (Pθ, Pα, Pβ, HD, PE) and frontal-parietal (STE) EEG leading to highest AUC is reported. Power spectral density Pθ, Pα, Pβ did not indicate loss of consciousness ($p > 0.05$). In contrast, HD, PE and STE provided significant separation of consciousness and unconsciousness as summarized in Tab. 1.

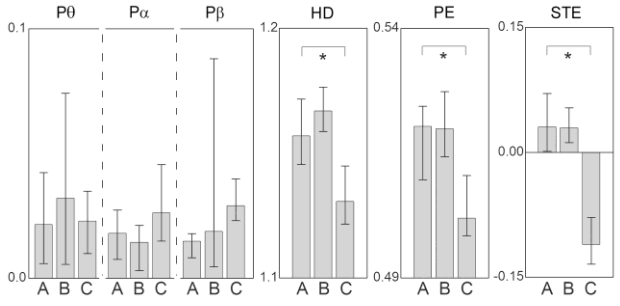

Figure 1: Median and 50% interquartile range of frontal EEG parameters Pθ, Pα, Pβ, HD, PE and frontal-parietal STE during (A) BL, (B) 0.5LOC and (C) LOC. *: Significant separation of consciousness (BL, 0.5LOC) and LOC.

In particular, during unconsciousness HD indicated a decrease of "dimensionality" in EEG, and PE indicated a decrease of "information content". Based on frontal-parietal EEG, STE showed a reliable separation of consciousness and unconsciousness, indicating a shift from predominantly fronto-parietal feedback (consciousness: STE > 0) to parieto-frontal feed forward "information processing" during LOC (STE < 0). This was induced by a decreased feedback ($\mathrm{STE}_{X\to Y}$) during LOC ($p < 0.05$).

Table 1: AUC including 95% CI at corrected threshold $p < 0.05$ of HD, PE and STE for separation of consciousness (BL, 0.5LOC) and LOC.

EEG parameter		AUC (CI)
HD	(frontal EEG)	↓ 0.89 (0.68-1.00)
PE	(frontal EEG)	↓ 0.90 (0.69-1.00)
STE	(frontal-parietal EEG)	↓ 0.99 (0.92-1.00)

Discussion

While EEG spectral analyses only showed weak effects of propofol, nonlinear analyses may provide additional information related to the dynamics of the brain. The observed decrease of HD and PE in frontal electrodes of the EEG could indicate a decline of higher-level cortical information processing during unconsciousness [1]. To further address whether consciousness is related to the brains ability to process information between cortical areas, EEG STE was found to be an adequate measure. STE indicated that long-range frontoparietal communication pathways (corresponding to default and attention control networks in fMRI) may be particularly affected. In contrast to unconsciousness, during propofol sedation the information exchange seemed to be largely preserved. This supports the hypothesis that the transition from consciousness to unconsciousness emerges from an on-off phenomenon [1] and is consistent with the reported persistence of the default mode network during sedation [2]. As a mechanism based measure that reliably differentiates consciousness from unconsciousness in frontal-parietal EEG, STE represents a promising approach for future techniques in EEG monitoring the "depth of anaesthesia".

Bibliography

[1] Alkire, M.T., Hudetz, A.G. et al.: Consciousness and anesthesia, *Science*, vol. 322, pp. 876-880, Nov. 2008

[2] Boveroux, P., Vanhaudenhuyse, A. et al.: Breakdown of within- and between-network resting state functional magnetic resonance imaging connectivity during propofol-induced loss of consciousness, *Anesthesiology*, vol. 113, pp. 1038-1053, Nov. 2010

[3] Ku, S.W., Lee, U. et al.: Preferential inhibition of frontal-to-parietal feedback connectivity is a neurophysiologic correlate of general anesthesia in surgical patients, *PLoS One*, vol. 6, no. 10, p. e25155, 2011

[4] Esteller, R., Vachtsevanos, G. et al.: A comparison of waveform fractal dimension, *IEEE Trans. Circuits and Systems*, vol. 48, no. 2, pp. 177-183, Feb. 2001

[5] Staniek, M., Lehnertz, K.: Symbolic transfer entropy, *Phys Rev Lett*, vol. 100, p. 158101, Apr. 2008

[6] Bandt. C., Pompe, B.: Permutation entropy: a natural complexity measure for time series, *Phys Rev Lett*, vol. 88, p. 174102, Apr. 2002

[7] Jordan, D., Stockmanns, G. et al.: Electroencephalographic order pattern analysis for the separation of consciousness and unconsciousness, *Anesthesiology*, vol. 109, pp. 1014-1022, Dec. 2008

Biomed Tech 2013; 58 (Suppl. 1) © 2013 by Walter de Gruyter · Berlin · Boston. DOI 10.1515/bmt-2013-4187

Analysis of dynamic respiratory mechanics profits from breathing-phase selective filtering

Sara Lozano-Zahonero, Sarah Buehler, Stefan Schumann, Josef Guttmann

Department of Anesthesiology, Division for Experimental Anesthesiology,

University Medical Center of Freiburg, Germany

sara.lozano@uniklinik-freiburg.de

Abstract: *Cardio-pulmonary coupling induces cardiogenic oscillations to the respiratory signals, which appear most prominently in the expiration. We hypothesized that the analysis of respiratory system mechanics profits from the breathing phase-selective filtering of expiratory data. Using the gliding-SLICE method, intratidal dynamic respiratory system mechanics were analyzed without and with low-pass filtering (cut-off-frequency f=4 Hz) of expiratory or inspiratory data separately. The quality of data analysis was derived quantitatively from the coefficient of determination (R^2). The selective filtering of expiration data eliminates negative side-effects of cardiogenic oscillations thus leading to a significant improvement of the analysis of dynamic respiratory system mechanics.*

Keywords: *controlled mechanical ventilation, dynamic respiratory mechanics, cardiogenic oscillations*

Introduction

Analysis of individual respiratory mechanics is used to guide the ventilator setting under conditions of lung protective mechanical ventilation in intensive care medicine [1]. In the last years the focus on the analysis in respiratory mechanics concentrates on dynamic conditions [2], which mean that the analysis is performed during uninterrupted mechanical ventilation with the inspiratory and expiratory airflow rate being different from zero [3].

During inspiration the ventilator provides the mechanical energy for respiratory gas transport into the lungs. The mechanical energy stored in the elastic tissue elements of the respiratory system drives the passive expiration which is characterized by exponential flow decay. Thus, after an initial expiratory peak flow the flow rate is very low during expiration. At low flow rates the transfer of mechanical energy from the beating heart to the lungs known as mechanical cardio-pulmonary coupling becomes visible as cardiogenic oscillations (COS) superimposed on the respiratory signals pressure and flow.

We hypothesised that filtering of the respiratory data obtained from the expiration phase would improve the analysis of intratidal respiratory system mechanics. Hence, the purpose of this study was to introduce the method of breathing-phase selective filtering and to test this approach by means of retrospective analysis of respiratory data from mechanically ventilated patients.

Methods

Patient data

We retrospectively analyzed data from a multicenter-study (28 patients with injured lungs, under volume-controlled ventilation) and from two additional studies (3 lung healthy patients and 3 with injured lungs, under pressure-controlled ventilation). For each patient, data streams were recorded at different positive end-expiratory pressure levels.

Analysis of dynamic lung mechanics

The volume-dependent respiratory system compliance was calculated using the gliding-SLICE method [4]. The gliding-SLICE method is based on multiple linear regression analysis (MLRA) to determine compliance Crsi, resistance Rrsi and the dynamic pressure base P0i for each slice by a least-squares fit of the equation of motion (see Eq. 1) to the pressure, flow and volume data of the respective slice i :

$$p = \frac{1}{C_{rsi}} \cdot V + R_{rsi} \cdot \dot{V} + P0_i \qquad (1)$$

Quality test of the lung mechanics analysis

The quality of the lung mechanics analysis, i.e., the "goodness" of the gliding-SLICE method was examined by calculating the coefficient of determination, R^2, for each slice.

Signal filtering

Expiratory and inspiratory periods were filtered separately in order to test for the effect of breathing-phase selective signal filtering. Airway pressure, volume and flow rate signals were filtered for a breathing-phase when the R^2 value was below 0.995.

We took advantage of the differences in the frequency content between cardiogenic oscillations and breathing signals. Therefore we used a low-pass filter with a cut-off frequency of 4 Hz.

Validation of filtering

The gliding-SLICE method was applied to the filtered signals of airway pressure, flow and volume to re-determine the values for compliance and resistance. Furthermore, the "goodness" of fit was analyzed after filter-

ing to verify if these re-determined parameters better adapted to the model (equation of motion). The quality of fit according to the R^2-values was classified as "high" for R^2 above 0.995, "medium" for R^2 between 0.995 and 0.990 and as "low" for R^2 below 0.990.

Results

For 69% of the data streams from patients under volume-controlled ventilation, the fit quality was already "high" before filtering and remained "high" after filtering. In 28% of the cases the fit quality improved from "medium" and "low" to "high" after the application of the low-pass filter. In 3% of the cases the quality of fit remained constant before and after the application of the filter. Low R^2-values were found accumulated in the lowest volume ranges. Particularly at the end of expiration, volume and pressure values underlied considerable disturbances which introduced an accumulation of high frequency signals.

Fig. 1 gives a synoptic view over the quality of lung mechanics analysis without filtering (Fig. 1a) and after breathing-phase selective filtering (Fig. 1b) for the 25 patients included in the multicenter-study.

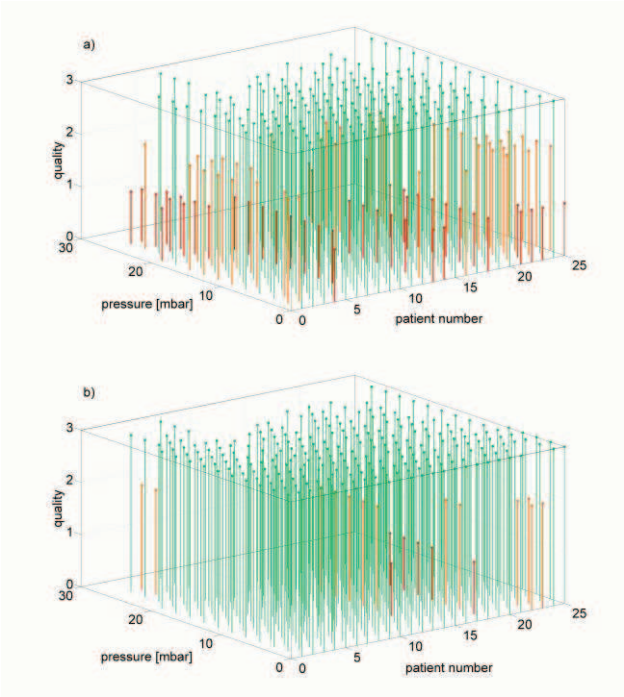

Figure 1: without filtering (a) and after breathing-phase selective filtering (b) for 25 patients from the multicenter-study. Both 3D-diagrams show 270 data points, each relating to the quality (z-axis) of the gliding-SLICE lung mechanics analysis for each patient (x-axis) and PEEP level between 0 and 28 mbar (y-axis). On the z-axis the quality of fit is displayed in 3 categories according to the absolute value for R^2: "1" for low quality; red ($R^2 \leq 0.990$); "2" for medium quality; blue ($0.990 < R^2 \leq 0.995$); and "3" for high quality; green ($R^2 > 0.995$).

The quality of fit, represented by R^2, never became worse with filtering. On the contrary, the R^2-value of every single slice within every single breath increased after the application of the low-pass filter.

Discussion

In this study we present a method for breathing-phase selective filtering of respiratory data obtained from patients under controlled mechanical ventilation. As the main result of our study we found a significant improvement of the analysis of dynamic respiratory system mechanics on a breath-by-breath basis when expiratory but not when inspiratory data were filtered.

Fluctuations in the expiratory phase can be seen where the airflow rate decays exponentially from an initial expiratory peak flow towards zero flow. As a possible explanation we identified COS reflecting the mechanical cardiopulmonary coupling, i.e., the transfer of mechanical energy from the beating heart to the lungs [5].

In conclusion, we were able to demonstrate that cardiogenic oscillations interfere with the lung mechanics analysis during the expiration phase. Breathing-phase selective filtering of respiratory data limited to the expiration could significantly improve the quality of the breath-by-breath analysis of dynamic intratidal lung mechanics.

Acknowledgement

The authors gratefully acknowledge the permission of this retrospective study by the principle investigators of the multicenter-study, Professors Ralf Kuhlen, Berlin, Christian Putensen, Bonn, Michael Sydow, Dortmund.

Bibliography

[1] Gattinoni L., Eleonora C., Caironi P.: Monitoring of pulmonary mechanics in acute respiratory distress syndrome to titrate therapy. *Curr Opin Crit Care* 11(3): 252-258, 2005

[2] Stenqvist O.: Practical assessment of respiratory mechanics. *Br J Anaesth* v.91(1): 92-105, 2003

[3] Mols G., Priebe H.-J., Guttmann J.: Alveolar recruitment in acute lung injury. *Br J Anaesth* 96(2): 156-166, 2006

[4] Schumann S., Burcza B., Haberthür C., Lichtwarck-Aschoff M., Guttmann J.: Estimating intratidal nonlinearity of respiratory system mechanics: a model study using the enhanced gliding-SLICE method. *Physiol Meas* 30(12): 1341-1356, 2009

[5] Lichtwarck-Aschoff M., Suki B., Hedlund A., Sjöstrand U.H., Markström A., Kawati R., Hedenstierna G., Guttmann J.: Decreasing size of cardiogenic oscillations reflects decreasing compliance of the respiratory system during long-term ventilation. *J Appl Physiol* 96(3): 879-884, 2004

Biomed Tech 2013; 58 (Suppl. 1) © 2013 by Walter de Gruyter · Berlin · Boston. DOI 10.1515/bmt-2013-4188

DETERMINING BLOOD PRESSURE CHANGES AND VASCULAR STIFFNESS STATE USING OPTICAL PULSE PRESSURE ANALYSIS

Y. Zhao[1], W.H. Kullmann[1]

[1]Institute of Medical Engineering, University of Applied Sciences Würzburg-Schweinfurt, Germany

Ying.Zhao@fhws.de

Abstract: *Blood pressure, blood vessel elasticity and pulse wave velocity are closely related in the cardiovascular system. In this study an optical pulse detection method is discussed to easily assess online continuous blood pressure changes and determine the vascular stiffness according to the concept of global pulse wave velocity (gPWV). Experiments were carried out under the condition of active physical exercises. The optical pulse wave signal at the index finger and ECG signal were recorded noninvasively and continuously. As a reference blood pressure was manually measured intermittently using a cuff at the arm. The results of pulse wave analysis reveal that the change of the calculated gPWV shows good correlation with the simultaneously measured blood pressure changes. The static value of the gPWV represents the state of elasticity of blood vessels.*

Keywords: *Blood Pressure, Pulse Wave, Pulse Wave Velocity, Vessel Elasticity*

Introduction

It is well known that increased vascular stiffness will result in increasing the human blood pressure (BP), and increased vascular stiffness will lead to faster pulse wave velocity (PWV), too. Continuous monitoring of blood pressure changes and detection of vascular stiffness are of great importance not only in clinical monitoring, but also in daily-tracking of ill or old persons at home. Because the PWV serves as a key indicator of both the arterial stiffness state and systolic blood pressure a good approach to estimate blood pressure changes and vascular status indirectly and continuously is the determination of the pulse wave velocity. Continuous detection of pulse wave velocity is currently determined either by using the pulse transit time between the simultaneously recorded ECG signal and corresponding peripheral pulse wave [1] or the pressure wave propagation time between the two positions along the extension of main arteries [2]. The common characteristic feature of these methods is that at least two different vital signals at two spatially separated detector positions are required. One crucial problem is the estimation of the correct distance. Here, a simple optical detection method using only the pulse wave signal at one peripheral detection position is analyzed in order to estimate the changes of blood pressure and the elastic state of blood vessels.

Methods

The method is based on the concept of global pulse wave velocity (gPWV) and the decomposition of the pulse wave into two components of Gaussian shape: the antegrade and retrograde contribution of the total pulse wave contour (cf. Figure 1) [3] [4].

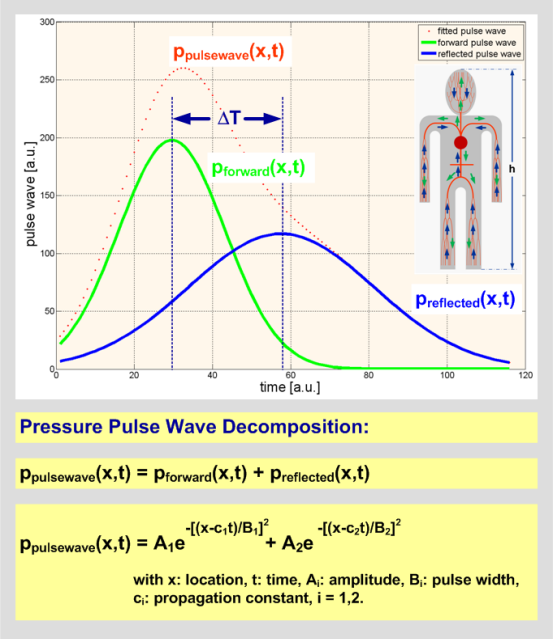

Figure 1: Decomposition of the pulse wave contour

The global pulse wave velocity (gPWV) and the global pulse transit time (gPTT) are defined as

$$gPWV = \frac{\Delta x}{\Delta T} = \frac{c_h h}{\Delta T} \quad (1)$$

$$gPTT = \Delta T \quad (2)$$

with Δx: overall travel distance, ΔT: mean travelling time, c_h: empirical length correction factor (c_h = 0.88), h: body height.

In order to confirm the feasibility of the method, a data set consisting of index finger pulse wave, ECG, and blood pressure was detected as function of time. Seven healthy volunteers (male and female) initially carried out exercises on a bicycle-ergospirometer (nSpire Health ZAN 600 USB CPX) with increasing power from 70 W to 200 W. Immediately after physical duty the volunteers' ECG-signal and pulse wave were recorded over a time period of 10 minutes using a cardiovascular detector system with synchronized ECG- and optical pulse detection developed by ourselves (sampling rate: 200 Hz, 10 bit A/D resolution, 0.2 Hz high pass filter). The systolic blood pressure was detected simultaneously

with an osciallatory cuff-based clinincal blood pressure detection system (Philips IntelliVue MP30).

On basis of the collected ECG- and optical pulse wave data different physiological parameters were calculated:

- global pulse wave velocity (gPWV) and global pulse transit time (gPTT) from the detected pulse wave contours,
- pulse transit time (PTT) between R-peak of ECG and pulse wave arrival at index finger.

Results

In order to test numerical accuracy and to reduce occasional effects the gPWV is calculated as an average value of several single pulses. Table 1 summarizes the correlation between global pulse wave velocity, calculated as an average of 6 to 60 single pulses, and systolic blood pressure. The cuff-based blood pressure detection is of time averaging character, too. The averaging over an increasing number of single pulse waves distinctly improves the correlation between global pulse wave velocity and blood pressure.

Table 1: Correlation between global pulse wave velocity (gPWV) and blood pressure (BP) for subject 1.

Number of pulses	Correlation gPWV-BP
60	0.9669
50	0.9650
40	0.9549
30	0.9428
20	0.9331
10	0.9203
6	0.9236

Figure 2 shows the temporal behavior of global pulse wave velocity (gPWV), calculated as an average over 30 consecutive pulse waves, and systolic blood pressure (SBP). It is evident, that changes in gPWV and SBP show a similar temporal behavior.

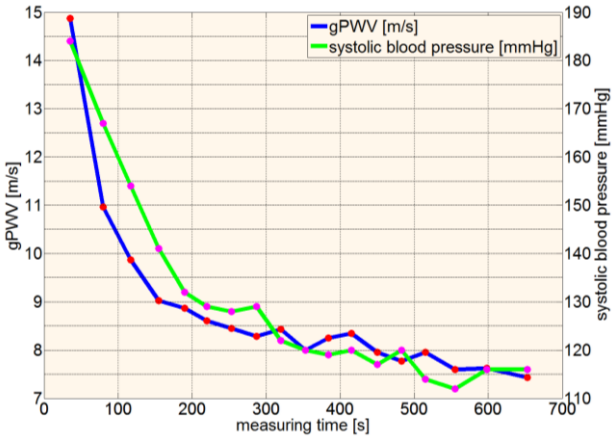

Figure 2: Calculated gPWV (averaged over 30 pulse waves) and detected systolic blood pressure SBP of subject 1.

Figure 3 represents the temporal behavior of the normalized calculated global pulse transit time (gPTT) and normalized detected pulse transit time (PTT), calculated as an average over 30 pulse waves of subject 1.

Figure 3: Normalized gPTT and normalized PTT (averaged over 30 pulse waves) of subject 1.

Under static condition (subject at rest) the gPWV represents the elastic state of the blood vessel [1][2], while gPWV measured under dynamic conditions is a surrogate of blood pressure changes.

Discussion

Global pulse wave velocity (gPWV) correlates well with systolic blood pressure (SBP), even though the correlation shows interindividual variation. The detection of gPWV can be used for continuous systolic blood pressure monitoring after an initial calibration. It is possible to monitor changes of systolic blood pressure with optical detection of the pulse wave at one peripheral detector position. Combined with the results of previous experiments [3] [4], gPWV at rest can be used to assess vessel elasticity.
Additional experiments have to be carried out in order to improve the reliability of the method.

Acknowledgement

Financial support from the Bavarian Ministry of Science, Research and the Arts, Munich, is gratefully acknowledged.

Bibliography

[1] W. Chen, T. Koboyashi, S. Ichikawa et al., *Continuous estimation of systolic blood pressure using the pulse arrival time and intermittent calibration,* Med. Biol. Eng., vol. 38 (5), pp. 569-574, 2000

[2] S. Laurent, J. Cockcroft, L. Van Bortel et al., *Expert consensus document on arterial stiffness: methological issues and clinical applications,* Eur. Heart J., vol. 27, pp. 2588-2605 (2006)

[3] Y. Zhao, W.H. Kullmann, *Arterial Stiffness Analysis based on Gaussian Pressure Pulse Wave Decomposition,* Biomed Tech 2011; 56 (Suppl. 1) P103, Walter de Gruyter: Berlin, Boston 2011

[4] Y. Zhao, W.H. Kullmann, *Applanation Tonometry for Determining Arterial Stiffness*, Biomed Tech 2012; 57 (Suppl.1) 669-672, Walter de Gruyter: Berlin, Boston 2012.

Biomed Tech 2013; 58 (Suppl. 1) © 2013 by Walter de Gruyter · Berlin · Boston. DOI 10.1515/bmt-2013-4189

INTERRELATION OF CARDIOVASCULAR DYSFUNCTION AND PUPILLARY FLUCTUATIONS IN PATIENTS WITH MAJOR DEPRESSION

Schumann A[1], Kralisch C[1], Bär KJ[1]

[1]Pain & Autonomics – Integrative Research (PAIR), University Hospital Jena, Germany

Andy.Schumann@med.uni-jena.de

Abstract: *Autonomic dysregulation in patients suffering from major depression is expressed in cardiovascular regulation as well as in the pupillary light reflex. We used spectral analysis and unrest indices to uncover indications of autonomic imbalance in resting pupillographic recordings. Significantly increased unrest and mean pupil diameters were observed in depressed patients. Pupillometric parameters correlated to symptom severity suggesting clinical relevance.*

Keywords: *autonomic regulation, heart rate, pupil diameter, major depression*

Introduction

Besides cardiovascular dysregulation, pupil sizes of patients suffering from major depression (MD) were found to reflect autonomic imbalance [1]. Pupil size is modulated by sympathetic and parasympathetic impacts. The objective of this study was to find indications of autonomic dysfunction in resting pupillographic recordings and their relation to cardiovascular function.

Methods

Cardiovascular and pupillographic recordings of 23 MD-patients and 23 matched controls were conducted using the MP150 polygraph (BIOPAC Systems Inc, Goleta, CA, USA). During the 20 minutes of measurement the room was absolutely quiet and fully shaded. To guarantee constant illumination level we used an indirect light source. An ellipse filling the whole 22 inch monitor was presented to enable focus movements within the acquisition window. Assuming participants to calm down at the beginning of the recording the first five minutes were not analyzed.

ECG and blood pressure were band-pass filtered between 0.05 to 35 Hz and digitized at 1000 Hz. Pupil size was assessed every 4 seconds by the infrared camera system RED 250 (SensoMotoric Inc., Boston, MA). Interruptions of pupillographic acquisition were substituted by interpolating adjacent data points. Eye blinks expressed as sudden drops of pupil diameter were eliminated using wavelet analysis. Affected segments were detected after signal decomposition using Daubechies wavelet of 10^{th} order and replaced by linear interpolation.

To analyse sympathetic and parasympathetic influence on pupil diameter fluctuation we exploited the different reaction times. The rapid signal conduction of parasympathetic pathways was demonstrated in pupil diameter modulation enabling the discriminative interpretation of the pupillary light reflex [2]. Vagal heat rate variability estimation is also based on the slow sympathetic reaction. Regarding the pupillary light response reaction times of pupil size similar to cardiac modulation can be assumed. We defined intervals for low (LF: 0.01-0.25 Hz) and high (HF: 0.25-0.5 Hz) frequency components representing the two autonomic branches. Their ratio was calculated to estimate balance.

Analyzing pupil size fluctuation we eliminated temporal mean. The Welch spectrum was estimated using a Blackman window lasting 128 s with 95 % overlap. Pupillary unrest index (PUI) was calculated based on the algorithm introduced by Lüdtke et al. [3]. Briefly, deviation of mean values of 80 s segments is computed. Additionally RMSSD and baroreflex sensitivity by sequence method were calculated estimating cardiovascular autonomic regulation in time domain.

Statistical analysis was conducted by a MANOVA of pupillary and cardiovascular parameters. If results were not normal distributed natural logarithmic transformation was performed. Spearman correlation was used to estimate linear relation of assessed parameters and to symptom severity assessed by Beck's Depression Inventory (BDI).

Results

Cardiovascular indices confirmed our assumption of autonomic imbalance suggesting diminished vagal activity. RMSSD and baroreflex sensitivity were reduced in MD patients (see Tab. 1).

Patients had larger pupil sizes with higher unrest indices. Low frequency component and overall Spectral power for $0.01\ \text{Hz} \leq f \leq 0.5\ \text{Hz}$ was increased in patients. In contrast high frequency power and LF/HF ratio were not significantly higher. Mean diameter and unrest index of the left pupil were significantly correlated to symptom severity assessed by BDI. Spectral pupillometric parameters were not correlated with cardiovascular autonomic indices but with global calculation of pupillary unrest.

Table 1: MANOVA of cardiovascular and pupillographic parameters (RMSSD: root mean square of successive heart beat intervals, BRS: baroreflex sensitivity, PUI: pupillary unrest index, DIA: mean pupil diameter, LF/HF: ratio of low and high frequency power of pupil size fluctuations, subscripts r and l stand for right and left pupil, HR: heart rate)

Parameter	Controls	Depressed	Significance
Heart rate [min^{-1}]	65.5	75,8	$p<0.01$
RMSSD [ms]	51.8	37,0	$p<0.05$
BRS [ms/mmHg]	22.0	13.0	$p<0.01$

Parameter	Controls	Depressed	Significance
PUI_l [mm]	0.093	0.140	$p<0.01$
PUI_r [mm]	0.097	0.139	$p<0.05$
DIA_l [mm]	3.82	4.26	$p<0.05$
DIA_r [mm]	3.65	4.20	$p<0.05$
LF [ms²]	38.01	76.33	$p<0.05$
HF [ms²]	12.97	24.67	n.s.
LF/HF [%]	3.92	3.32	n.s.

Discussion

An elevated sympathetic activity of patients with major depression was shown in cardiovascular parameters. In pupillometric data we also found significant differences. An increased mean pupil diameter was already reported in studies analyzing pupillary light reflex and is generally related to sympathetic predominance.

Pupillary unrest is commonly related to sleepiness [3]. Spectral power of pupil size fluctuations was increased in patients and highly correlated to PUI. This indicates an augmented daytime sleepiness in MD patients that is related to their symptom severity. An elevated low frequency power suggests that especially sympathetic influence contributes to increased pupil fluctuations. High frequency power does not reflect parasympathetic attenuation.

Pupillary fluctuations by central autonomic regulation are not as intensively investigated as at the cardiovascular level. Maybe influences like cognitive load or sleepiness complicate estimation of autonomic impact. However pupillographic indices correlating with symptom severity but not with cardiovascular autonomic markers demonstrate that pupillometry can give important information additionally to standard analysis.

Bibliography

[1] K.-J. Bär, W. Greiner, T. Jochum, M. Friedrich, G. Wagner, and H. Sauer, “The influence of major depression and its treatment on heart rate variability and pupillary light reflex parameters.,” *Journal of affective disorders*, vol. 82, no. 2, pp. 245–52, Oct. 2004.

[2] K. Yamaji, Y. Hiratai, and S. Usui, “The pupil as a possible monitor of the autonomic nervous system,” *Proceedings of the 19th International conference, Biology Society, 1997*, vol. 2777, no. C, pp. 2777–2781, 1997.

[3] H. Lüdtke, B. Wilhelm, M. Adler, F. Schaeffel, and H. Wilhelm, “Mathematical procedures in data recording and processing of pupillary fatigue waves.,” *Vision research*, vol. 38, no. 19, pp. 2889–96, Oct. 1998.

Biomed Tech 2013; 58 (Suppl. 1) © 2013 by Walter de Gruyter · Berlin · Boston. DOI 10.1515/bmt-2013-4190

A NOVEL METHOD FOR MOTION ARTIFACT REMOVAL IN WEARABLE PPG SENSORS BASED ON BLIND SOURCE SEPARATION

Maik Pflugradt[1], Marcus Rose[1], Reinhold Orglmeister[1],

[1]Electronics and medical signal processing, TU Berlin, Germany

Maik.Pflugradt@tu-berlin.de

Abstract: *The recent development of healthcare systems has provided a significant contribution to ambulatory patient monitoring. In that context, signal quality and disturbances induced by noise or motion artifacts play an important role in the field of signal processing tasks. Especially the Photoplethysmogram (PPG) is very liable to movement artifacts which severely hamper the extraction of vital parameters like the heart rate or oxygen saturation. To record patient movements, an innovative sensor system is proposed, which acquires accelerometer data next to the PPG. As in Adaptive Noise Cancelers, we propose to use the acceleration as reference to recover corrupted PPGs by means of the Blind Source Separation. Sophisticated methods of ICA have been used, resulting in a novel approach for artifact suppression in the PPG that has been tested on laboratory datasets.*

Keywords: *Blind Source Separation, Motion Artifacts, Body Sensor Network, ANC, ICA*

Introduction

Transmissive PPG systems basically consist of a finger clip which contains at least a red and infrared LED, emitting light through the finger to a photodetector [1]. Additionally equipping this finger clip with an accelerometer is a neat way to acquire a movement reference signal which has already been proposed by different groups in the literature [2] [3].

Prior to any signal processing tasks and their subsequent evaluation, considerable effort is put in preprocessing procedures, aiming at the removal of unwanted signal disturbances. As is well known, common filtering techniques like lowpass and highpass filters fail in reconstruction tasks when the components of signal and noise overlap in the frequency domain or the noise has a non-stationary nature [4]. The Adaptive Noise Cancelation (ANC) as shown in Figure 1, constitutes a thoroughly tested approach in PPG preprocessing, to cancel out unwanted signal components, that correlate with the reference signal which itself is provided by the accelerometer [2] [5].

These ANC implementations seem to achieve reasonable results in terms of increased signal-to-noise-ratios (SNR) of the reconstructed signal. In real applications however, these algorithms still experience difficulties in their tasks of reliable artifact suppression.

Alternatively, the more sophisticated method of Blind Source Separation has been proposed as a powerful approach to noise reduction by means of separating the independent components of the acquired signals [4] [6].

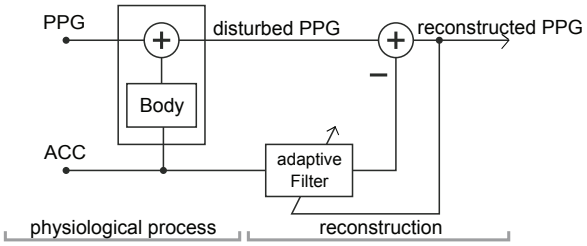

Figure 1: ANC with acceleration reference [5]

Methods

Independent Component Analysis

Basically, the ICA approaches try to find an estimated solution of the generative linear model

$$\mathbf{x} = \mathbf{A}\mathbf{s} \tag{1}$$

where the observation vector $\mathbf{x}$ is described by an instantaneous mixture of the statistically independent sources $\mathbf{s}$ [7]. The goal of ICA is to find the original sources by estimating the inverse of the mixing matrix $\mathbf{A}$. Stetson assessed the performance of different ICA methods on synthetically mixed pulse oximetry signals [8]. In the tests conducted in the scope of our study, these instantaneous models did not yield satisfying results.

Volmer [6] experienced similar problems and in turn suggested to resort to the convolutive mixing model which is consecutively solved by the SOBI algorithm [9]. Using only the red and infrared channel as input for this ICA model, Volmer was able to provide a robust method for oxygen saturation measurement [6]. Using this approach for pulse wave reconstruction in the time domain does not provide very satisfying results though. Therefore, we propose to feed the ACC signals to the convolutive mixing model.

Experimental Setup

In the scope of this study, two transmissive pulse-oximetry sensors have been used, which are part of a Body-Sensor-Network (BSN) [3]. The sensor basically embodies an MSP430F1611 microcontroller, equipped with a CC2500 Low-Power 2.4 GHz RF Transceiver for synchronization and communication issues and an SD Card for mass data storage. As initially mentioned, a 3-Axis ADXL330 Accelerometer is built directly into the finger clip, serving as a well located source for movement acquisition.

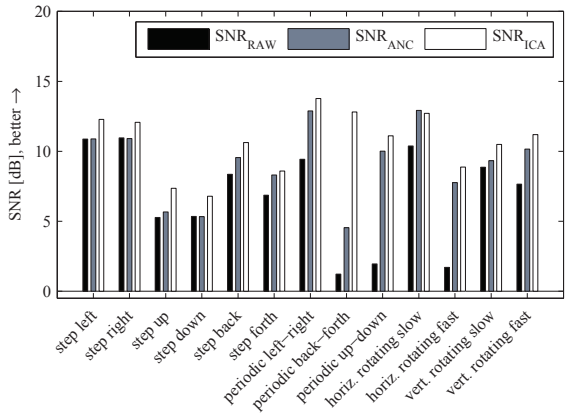

Figure 2: SNR results of raw PPG, ANC PPG and ICA PPG

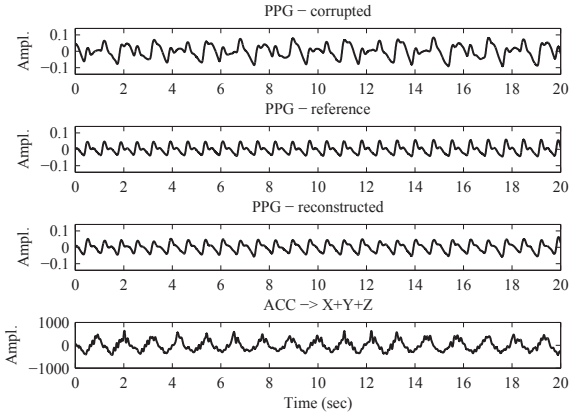

Figure 3: Noise Cancelation of corrupted PPG signal

As described in the previous chapter, the principal objective of this study is to present a convolutive ICA framework to clean the PPG signals from motion artifacts. Therefore, multiple measurements using two transmissive pulse oximeters of 120 seconds duration have been conducted, that contained various movement patterns to induce different kinds of motion artifacts. During each measurement, the right hand was exercising in the experiment, whereas the left remained in a fixed position to provide a nearly undisturbed reference PPG. The PPG signal and the ACC signals have been sampled at 200 Hz.

Results

In order to provide an objective assessment of the achieved results, the SNR values of the estimated PPG signals with regard to the respective reference signals have been calculated. The ACC reference input is calculated by the sum of the ACC signals' x-, y- and z-component. Figure 2 shows the SNR values of the raw signal (black), the SNR of the ANC PPG output (grey) and the SNR of the estimated PPG by the proposed ICA method (white) for the different movements. As can be seen, the proposed ICA method outperforms the ANC approach in terms of increased SNR values. A visual impression of the noise cancelation is given in Figure 3, showing the reconstruction of the PPG signal which has been disturbed by periodic back and forth movements during the experiment.

Discussion

In this work, a novel method for artifact removal of transmissive PPG signals has been proposed. It was shown that the performance of this new approach yields better results than the methods proposed by using classical ANC algorithms. This results in more robustness of physiological applications like pulse rate detection. It should be mentioned, that compared to the ANC method the convolutive ICA approach demands higher computational load which might require more powerful architectures for mobile applications as were presented in [10].

Bibliography

[1] J. G. Webster, *Design of Pulse Oximeters*. 270, Madison Avenue: TaylorFrancis Group, New York, 1997.

[2] A. R. Relente and L. G. Sison, "Characterization and adaptive filtering of motion artifacts in pulse oximetry using accelerometers," in *Proc. Conf. EMBS/BMES*, vol. 2, pp. 1769–1770, October 2002.

[3] A. Volmer and R. Orglmeister, "Wireless body sensor network for low-power motion-tolerant synchronized vital sign measurement," in *30th Ann. Int. Conf. IEEE EMBS*, pp. 3422–3425, August 2008.

[4] K. T. Sweeney, T. E. Ward, and S. F. McLoone, "Artifact removal in physiological signals – practices and possibilities," *IEEE Trans. on Inf. In Techn. In Biomed.*, vol. 16, pp. 488–500, August 2012.

[5] A. Volmer, S. Feese, and R. Orglmeister, "Kompensation von bewegungsartefakten in langzeit-ppg-signalen mittels adaptiver filterung," in *Aut. techn. Verfahren für die Med., AUTOMED*, pp. 9–10, 2009.

[6] A. Volmer, *Unterdrückung von Bewegungsartefakten beim Langzeitmonitoring zur Anwendung in Personal-Healthcare-Systemen*. PhD thesis, TU Berlin, 2010.

[7] A. Hyvärinen, J. Karhunen, and E. Oja, *Independent Component Analysis*. 605, Third Avenue: John Wiley and Sons, New York, 2001.

[8] P. F. Stetson, "Independent component analysis of pulse oximetry signals," in *Proc. 26th Ann. Int. Conf. IEEEE EMBS*, pp. 231–234, September 2004.

[9] A. Belouchrani, K. Abed-Meraim, J. F. Cardoso, and E. Moulines, "A blind source separation technique using second order statistics," *IEEE Trans. Signal Processing*, vol. 45, pp. 434–444, September 1997.

[10] M. Pflugradt, N. Hoffmeyr, and R. Orglmeister, "Multi-channel biosignal processing on an omap3530 system," in *EDERC 2012 Europ. DSP Education and Research Conf.*, pp. 124–128, September 2012.

Biomed Tech 2013; 58 (Suppl. 1) © 2013 by Walter de Gruyter · Berlin · Boston. DOI 10.1515/bmt-2013-4191

SIGVIEWER AND SIGNALSERVER – OPEN SOURCE SOFTWARE PROJECTS FOR BIOSIGNAL ANALYSIS

Clemens Brunner, Christian Breitwieser and Gernot R. Müller-Putz

Institute for Knowledge Discovery, Graz University of Technology, Austria

clemens.brunner@tugraz.at

Abstract: *We have developed two open source biosignal processing applications used at both ends of the signal processing chain, namely the signal acquisition server SignalServer and the signal visualization and analysis application SigViewer. Both programs are cross-platform (that is, they run under Windows, Mac OS X, and Linux operating systems), free open source software, and licensed under the GNU General Public License (GPL). SignalServer records raw data from various data acquisition devices and sends the data over the network in a standardized format. SigViewer reads many different biosignal formats and visualizes the contained multi-channel time series data. In addition, SigViewer supports annotations via custom event markers.*

Keywords: *Biosignal analysis, signal acquisition, software, open source, GPL*

Introduction

Open source software has numerous advantages over proprietary applications, especially in the area of scientific research and development. For example, researchers can change and adapt the source code to fit their specific requirements. Existing software components can be reused, and bugs can be fixed in the source code by every user. Depending on the specific license used in a project, it is often required to make any changes to the source code available to the public again, using the same license as in the original program. Such licenses are called copyleft licences. The most prominent example for a copyleft license is the GNU General Public License (GPL).

We have developed two biosignal processing applications used at both ends of the signal processing workflow, namely the signal acquisition server SignalServer and the signal visualization and analysis application SigViewer. Both programs are cross-platform (that is, they run under Windows, Mac OS X, and Linux operating systems), free open source software, and licensed under the GNU GPL[1].

SignalServer

SignalServer (tools4bci.sourceforge.net/signalserver.html) is a program to record data from various sources such as biosignal amplifiers, data acquisition cards, joysticks, and mice [1]. A frequently updated list of supported devices, which includes devices such as g.USBamp, g.Mobilab, g.BSamp (g.tec medical engineering GmbH, Austria), and BrainVision BrainAmp (Brain Products GmbH, Germany), can be found on the project website. SignalServer provides an abstraction layer between hardware devices and programs receiving the recorded data. To this end, data is transmitted in a standardized format over the network via TCP/IP or UDP.

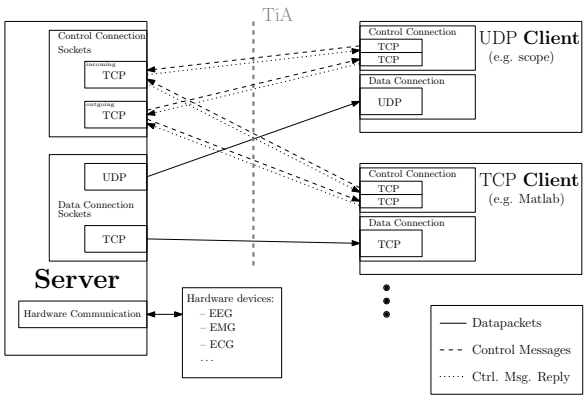

Figure 1: Concept of TiA communication between SignalServer (left) and clients (right).

SignalServer works (as the name suggests) as a server, and one or more clients can connect to this server to receive data. Communication between client and server adheres to the protocol defined in the "TOBI interface A" (TiA)[2], as provided by the TiA library (tools4bci.sourceforge.net/tia.html) [2]. Client and server communicate over a TCP/IP control connection, which uses plain text and XML messages inspired by HTTP. Data is sent over a another dedicated TCP/IP or UDP connection. Figure 1 illustrates the communication between SignalServer and clients.

The program is written in the standard C++ programming language and makes use of the Boost libraries[3]. Therefore, SignalServer runs under Windows, Mac OS X, and Linux platforms. However, since currently many hardware manufacturers provide only Windows drivers for their devices, SignalServer does not support data acquisition from some devices under non-Windows operating systems.

Extensive performance and stability tests have already been carried out [1]. The results showed that SignalServer has a low CPU load (depending on the signals, between 0–13 %),

[1] Note that SigServer is actually dual-licensed under the GPL and a commercial license.

[2] arxiv.org/abs/1103.4717

[3] www.boost.org

low memory footprint (again depending on the signals between 500 kB and 12 MB), and is stable over extended periods of time. The mean processing time is in the range of µs, and the typical network delay is around 0.1 ms.

Recently, SignalServer was extended to transmit only specific user-defined channels and/or downsample raw data to reduce network traffic and/or CPU load on the client side. Furthermore, SignalServer can save its data streams directly to GDF[4].

SigViewer

SigViewer (sigviewer.sourceforge.net) visualizes biosignal data streams such as EEG, EMG, EOG, ECG, and so on [3]. The application can load most biosignal formats provided by a library of the BioSig project [4], including .GDF, .EDF, .BDF, .CNT, .DAT (BCI2000), and .EEG (Brain Products GmbH, Germany). In addition to displaying data, SigViewer supports creating and saving annotations of arbitrary data chunks. These annotations can be used to mark segments in the data, for example to highlight artifacts in the EEG. Subsequent data analysis can then make use of these markers and exclude these segments from further processing.

In addition to visualizing data streams and annotations (see Figure 2 for a screenshot of the main window), SigViewer can also display associated meta information stored with the data files. Furthermore, SigViewer can compute and display the power spectrum and the mean time course averaged over selected epochs. The latter feature essentially isolates event-related potentials (ERPs).

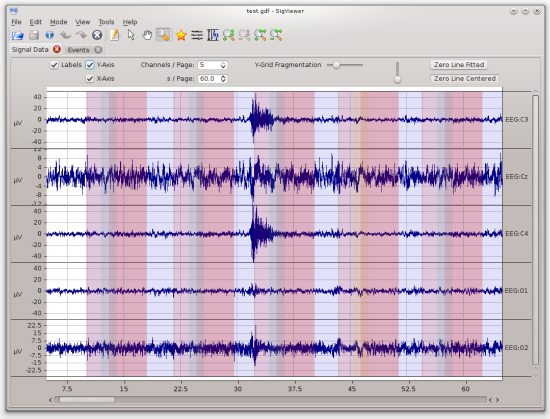

Figure 2: SigViewer's main window (running under Linux) showing five EEG channels with colored annotations and visualization options (above signals).

SigViewer is written in C++ and uses the cross-platform Qt 4 libraries[5]. Therefore, just like SignalServer, SigViewer also supports the three major operating systems mentioned above.

[4] arxiv.org/abs/cs.DB/0608052

[5] qt.digia.com

Discussion

Both applications, SignalServer and SigViewer, can be used in the signal processing workflow typical for biosignal processing, which consists of signal acquisition, signal processing, and signal visualization parts. While SignalServer unifies data streams from various harware devices by using TiA, SigViewer visualizes recorded data offline and offers numerous tools for signal analysis.

Both software projects are free and open source, and both programs are cross-platform. SignalServer is dual-licensed, so if the copyleft license cannot be used, a proprietary license is also available. Future work on SignalServer will include the integration of new hardware devices and the support of other interfaces used for (hybrid) brain-computer interfaces (BCIs) [2], such as event markers used in BCI experiments. These events, along with other metadata, can be stored directly in a GDF file, for example.

The list of devices supported by SignalServer will be continuously updated in the future. Other possible extensions include improved interoperability with other software platforms and support for other file formats for storing incoming data streams. SigViewer will receive new functionality as requested by the community. Possible major extensions include filtering of signals (high or low pass filters), computation of ERDS maps, and improved editing of metadata and event information.

Acknowledgement

This work was partly supported by the European ICT Project FP7-224631 (TOBI – Tools for Brain-Computer Interaction).

Bibliography

[1] C. Breitwieser, I. Daly, C. Neuper, and G. R. Müller-Putz, "Proposing a standardized protocol for raw biosignal transmission," *IEEE Transactions on Biomedical Engineering*, vol. 59, no. 3, pp. 852–859, 2012.

[2] G. R. Müller-Putz, C. Breitwieser, F. Cincotti, R. Leeb, M. Schreuder, F. Leotta, M. Tavella, L. Bianchi, A. Kreillinger, A. Ramsay, M. Rohm, M. Sagebaum, L. Tonin, C. Neuper, and J. del R. Millán, "Tools for brain-computer interaction: a general concept for a hybrid BCI," *Frontiers in Neuroinformatics*, vol. 5, p. 30, 2011.

[3] C. Brunner, A. Schlögl, and G. Pfurtscheller, "SigViewer – an open source viewing and scoring program for biomedical signals," in *Proceedings of the Fourth International Brain-Computer Interface Workshop and Training Course*, (Graz, Austria), pp. 396–400, 2008.

[4] A. Schlögl and C. Brunner, "BioSig: a free and open source software library for BCI research," *Computer*, vol. 41, pp. 44–50, Oct. 2008.

Biomed Tech 2013; 58 (Suppl. 1) © 2013 by Walter de Gruyter · Berlin · Boston. DOI 10.1515/bmt-2013-4192

Analytic Signal Based Detection of Extracellular Action Potentials

Doerr C.[1], Schanze T.[1]

[1] FB KMUB, Technische Hochschule Mittelhessen, Germany

Christopher.Doerr@KMUB.THM.de

Abstract: *A method for calculating the instantaneous energy of extracellularly recorded action potentials using the analytic signal has been developed and tested. The energy is computed from the recorded signal with Hilbert filter based multi-resolution energy filters with optimized signal to noise ratio. The computed instantaneous energy is used for threshold based detection of action potentials in the signals.*

Keywords: *Extracellular recordings, action potentials, spike detection, analytic signal, Hilbert filter*

Introduction

To get an insight in the neuronal processing of information in the brain, extracellular multi-neuron recordings with multiple electrodes, like tetrodes or heptodes, are commonly used. These recordings contain action potentials (spikes) from different neurons at various distances and, unfortunately, artefacts and noise.
Spike sorting is used to first separate spikes from noise and second to classify spikes into different clusters that correspond to different neurons. The extraction of spikes from raw signals is called spike detection.
A common spike detection approach consists of the computation of a signal representation that enhances the signal to noise ratio, like the instantaneous power or energy of the signal. Then a thresholding is applied and peaks above threshold are detected and marked as spikes. The next step is the alignment of the detected spikes for subsequent clustering analysis.
A commonly used method to detect the instantaneous energy of a signal is the Teager-energy-operator (TEO) or, modified for spike detection, the multi-resolution-TEO (MTEO) [1, 3].
However, Vakmann showed that especially for wide-band and noisy signals the computation of the analytic signal with the Hilbert transformation is more robust than using TEO [2]. In addition, since the TEO has been developed for harmonic oscillators, it is unable to compute the energy for some important classes of signals, e.g. the exponential function. Tests of the TEO for spike detection showed that many negative energy values occurred, which have to be eliminated by a low pass filter. This leads to a worsening of the, theoretically good, temporal resolution and, in combination with thresholding, a decrease of performance when overlapping or adjacent spikes are present. The spectral resolution is, due to the short operator duration, poor.
Our focus lies on the improvement of the initial spike detection algorithm for a heptode spike sorting program.

Methods

We adopted the spike detection algorithm from Franke et al. [3], tested and improved its performance. This spike detection algorithm is based on the MTEO.
We developed a multi-resolution energy filter (MEF) by adopting the multiresolution approach of the MTEO and replacing the TEO by a Hilbert filter approach.

The analytic signal: The analytic signal is defined as [2]

$$\psi(t) = u(t) + j\,v(t) = A(t)\,e^{j\phi(t)}, \qquad (1)$$

where $v(t) = H[u(t)]$ is the Hilbert transformed of $u(t)$, the recorded signal. The instantaneous energy is calculated with

$$E_{\psi}(t) = |\psi(t)|^2 = u(t)^2 + v(t)^2. \qquad (2)$$

The instantaneous amplitude of the analytic signal represents the envelope of the signal.
One important property of the analytic signal is that its spectrum is zero for negative frequencies. Thus a straightforward method to compute the analytic signal is to set Fourier-components with negative frequencies to zero and to multiply other components by two. This is the multiplication of the signal's Fourier spectrum with two times the unit-step function [4]. To compute the analytic signal in the time domain a FIR-filter can be constructed by using the inverse Fourier transformation of the unit step function [5].

Hilbert bandpass filter: To improve the analytic signal based discrimination of spikes and noise, the signal is filtered by a Hilbert bandpass filter. This filter consists in the frequency domain of a $\sin^2$ tapered rectangular window. By multiplying it with two times the unit-step function, a Hilbert bandpass filter results.
By means of tunable center frequency and quality factor, the spectro-temporal properties of the Hilbert bandpass filter can be adjusted to signal's characteristics.

Multiresolution energy filter: The detection and decomposing/separation of adjacent and overlapping spikes can be improved, when the filter responses are as short as possible. This is best achieved by using short Hilbert bandpass filters that are not affected by adjacent spikes.
To obtain optimally short filters for spikes of different duration, we constructed a multiresolution energy filter.
However, extracellulary recorded spikes are in most cases biphasic. It is well known that the duration of the spikes is related to their spectral properties. Longer lasting spikes have more low frequency components while short lasting spikes have more high frequency components. We use these facts, by covering the overall bandwidth with over-

lapping filters of adequate small bandwidths in combination with optimal lasting impulse responses. This ensures that virtually only adequate spectro-temporal match of spike and filter properties yield optimal spike detection properties.
All filters have the same quality factor Q that is computed from the count of filters and the overall bandwidth.
Signal's energy is calculated from filter responses according to equation (2) and the maximum of the filter responses is selected by a winner-take-all process for subsequent threshold based detection.

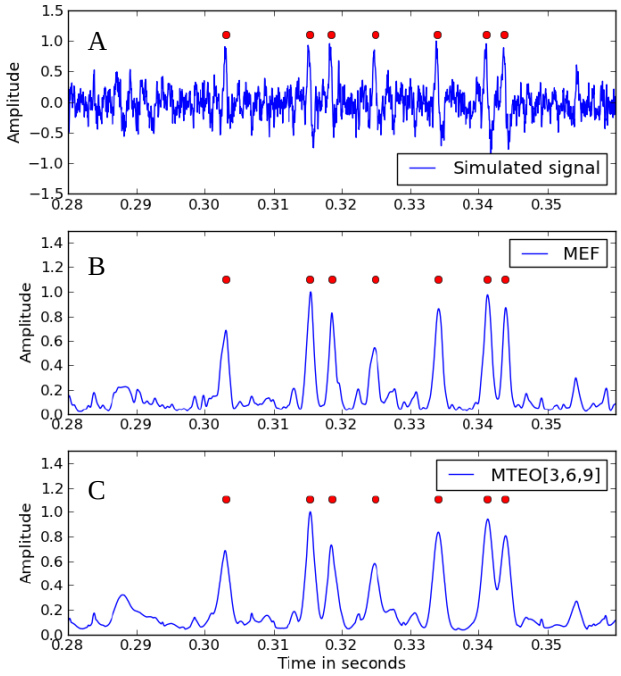

Figure 1: A) Segment from a simulated extracellular recording. B) MEF-responses with optimized parameters and C) MTEO-responses with k-values of 3, 6 and 9. Red dots indicate true spikes locations. At 0.34 s, the respond of MEF to adjacent spikes is, with respect to temporal resolution, clearly superior to the response of the MTEO.

Signal simulation: The simulated tetrode-signals for testing the performance of the spike detection algorithm consists of biphasic spikes of different length and simulated noise.
The duration of spikes ranges from 0.8 ms to 2.8 ms. Signals with spikes of just one duration were simulated and, especially, signals with a mixture of spikes of different durations. There were no overlapping but adjacent spikes in the signal.
Amplitude distribution and spectrum of the Gaussian white noise has been modified to be similar to noise present in extracellular recordings. The spikes have been modelled with two Gaussian curves.

Performance testing: The performance of spike detection has been analyzed via receiver operating characteristic (ROC) and quantified by measuring the area-under-the-curve (AUC) of the ROC-curve.

Table 1: Values of the measured AUC of MEF with optimized parameters and the MTEO with k-values of 3, 6 and 9. Signal 4 contains a mixture of spikes of different durations from 0.8 to 2.8 ms.

Signal ID	Duration of spikes in signal in ms	AUC for MEF	AUC for MTEO
1	0.8	0.94	0.91
2	1.8	0.95	0.92
3	2.8	0.90	0.90
4	0.8 to 2.8	0.90	0.88

Results

Our preliminary results show, that the performance of the novel spike detection algorithm is equal or even better than the performance of the MTEO spike detector, each with optimal parameter sets (Table 1).
The temporal response resolution of our MEF is better than that of the MTEO detector (Fig. 1). Notably, the detection of adjacent or overlapping spikes is easier and more robust compared to the MTEO detector.
However, both filters, MTEO and MEF, tend to detect shorter spikes better than longer-lasting spikes. This may be due to trade-offs between parameter settings, signal properties and detection performance.

Discussion and Conclusion

We developed and tested a new spike detection algorithm based on the analytic signal that is superior to the MTEO spike detector. However, additional testing of its performance with simulated and real signals containing overlapping spikes, tests concerning the robustness under several signal conditions and automatic parameterization will be addressed in future work.

Bibliography

[1] Choi, J.H., Jung, H.K., Kim, T.: A New Action Potential Detector Using the MTEO and Its Effects on Spike Sorting Systems at Low Signal-to-Noise Ratios, *IEEE Trans. Biomed. Eng.*, 53 (4), pp. 738-746, 2006
[2] Vakman, D.: On the analytic signal, the Teager-Kaiser energy algorithm, and other methods for defining amplitude and frequency, *IEEE Trans. Signal Process.*, 44 (4), pp. 791–797, 1996.
[3] F. Franke, M. Natora, C. Boucsein, M. Munk, K. Obermayer: An online spike detection and spike classification algorithm capable of instantaneous resolution of overlapping spikes, *J. Comput. Neurosci.*, 29 (1-2), 127-148, 2009.
[4] Bruns, Andreas: Fourier-, Hilbert- and wavelet-based signal analysis: are they really different approaches?, *J. Neurosci. Methods*, 137 (2), pp. 321–332, 2004.
[5] Reilly, A.; Frazer, G.; Boashash, B.: Analytic signal generation-tips and traps, *IEEE Trans. Signal Process.*, 42 (11), pp. 3241–3245, 1994.

Acknowledgements

This work is funded by BMWi ZIM KF2268909AK2.

Biomed Tech 2013; 58 (Suppl. 1) © 2013 by Walter de Gruyter · Berlin · Boston. DOI 10.1515/bmt-2013-4193

SUBVIRAL PARTICLE TRACKING

Christian Kienzle[1], Gordian Schudt[2], Stephan Becker[2], Thomas Schanze[1]

[1]KMUB, Technische Hochschule Mittelhessen, Germany
[2]Institute for Virology, Philipps-Universität Marburg, Germany

christian.kienzle@kmub.thm.de

Abstract: *Fluorescence microscopy is a common technique to investigate biological processes at a cellular level. In order to analyze the patterns of movement of subviral particles in cells, fluorescent proteins have been embedded in viral protein complexes. Fluorescence microscopy image sequences often contain many different particles, making the analysis a very time-consuming process. Therefore we started the development of an automated tracking of subviral particles present in fluorescence microscopy image sequences.*

Keywords: *Particle tracking, fluorescence microscopy, subviral particle, cell, image processing.*

Introduction

Microscopy is a common technique to investigate biological processes at a cellular level. By the means of fluorescence microscopy it is possible to visualize fluorescent proteins and more complex cellular structures containing these proteins. To achieve this, we inserted genetic sequences of fluorescent proteins into viral DNA. This approach allowed us to visualize the intracellular movements of the fluorescent marked subviral particles. The resulting image sequences can be interpreted by specialists, who are able to distinguish these particles from regular cellular components. As there can be a lot of different particles in just one observed cell, it is in general not possible to manually track all of them. Thus it is of major interest to develop digital image processing algorithms that allow an automated tracking of each particle.

Methods

The automatic tracking of subviral particles pictured by means of fluorescence microscopy sequences requires several steps. However, even manual tracking of subviral particles is often only possible for some images. Particles get blurry or even invisible from one image to the next as they move through different layers of the cell or due to crossing some other fluorescence marked areas. This problem might be solved by using information from image sequences. An initial guess of particle's shape or velocity can be used to estimate the position of the particle by interpolation. A straightforward first step to make automatic tracking possible is to extract characteristics of particle movements and to use the estimated parameters for a subsequent analysis.

The next step is to identify subviral particles given the characersitics of their respective image representations. This improves the detection of a particle and, in addition, its identification. Many different mathematical methods can be used to extract features from images. However, there is no perfect method, since all methods have advantages and disadvantages. Thus, we started to test some prospecting methods in order to develop an accurate and robust subviral particle tracking algorithm.

The pixel intensity distribution of each particle can be approximated by a two dimensional Gaussian distribution. Using this ansatz a correlation with a Gaussian kernel can be used to enhance the contrast of the particles, to separate them from the noisy background and to adjust the kernel's parameters.
Thus the quality of subsequent analyses can be increased by fitting a rotated two dimensional Gaussian distribution function to each of the detected particles. A good method to extract size and alignment or rotation of the particles, corresponding to size and alignment of the 2D Gaussian function, is principal component analysis (PCA). In further steps the PCA can also be used to extract optical features of the particles by eigenvalue and eigenvector based intensity distribution analysis. Using this information and the previously gained knowledge about the characteristics of the movements of the particles, as an input for a currently developed algorithm, allows the identification of the particles in subsequent images. Here we report on initial results concerning trajectories and velocities of subviral particles that we obtained by manual tracking.

Results

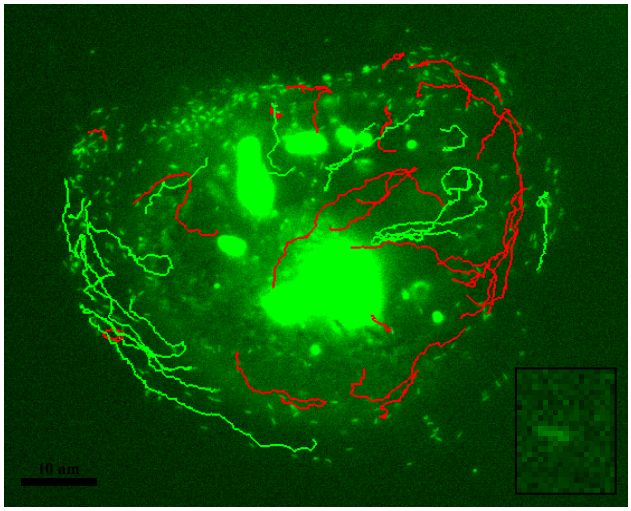

Figure 1: Tracks of subviral particles (red: moving to the cell's center, green: moving to the cell membrane); rectangle: enlarged single particle

Figure 1 shows green and red colored trajectories of subviral particles in a renal cell captured by fluorescence microscopy. The trajectories have been plotted over the first image of the image sequence. The particles have been tracked manually in order to generate initial and reliable information about the particles, e.g. position and velocity.
A problem concerning simple manual tracking is, that the position of the particles is limited to pixel size of the camera system. This leads with respect to the pixel size of the particles to uncertainties which we started to remove algorithmically by using PCA.
Figure 2 shows the frequency distribution of the velocity of subviral particles for a sequence of 250 images obtained by our PCA based analysis. Similar results were obtained for another sequence.

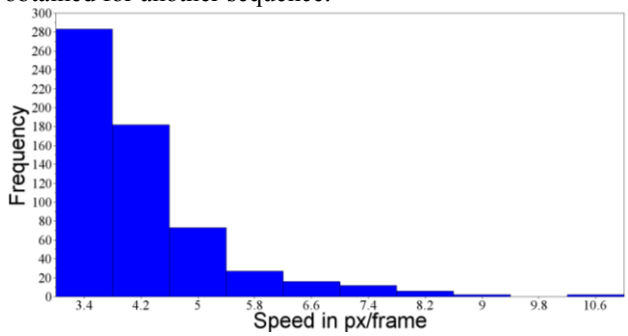

Figure 2: Histogram of intracellular velocities of subviral particles.

Discussion

We are interested in biological processes at the subviral level and showed that fluorescence microscopy and image processing can provide interesting parameters. However, there are considerable variations between image sequences and subsequent images of an image sequence. Some are related to the movement optically marked subviral particles, but some are unwanted noise or artifacts, that might be removed algortihmically. Thus we started to develop an automated and robust algorithm for subviral particle tracking. Unfortunately, the fluorescence of the subvrial particles is often weak. In addition, there are some unedifying general constraints in the settings for the image acquisition, e.g. a sufficiently high signal-to-noise ratio requires often a long exposure time, which is, on the other hand, disadvantageous with respect to temporal resolution. It is well known that a low temporal resolution leads to blurring and pseudo-jumps of fast moving objects. If, anyhow, the image quality is good, there are still some challenges that hamper the identification of subviral particles. The optical crossing of different particles or their movements over regions with high fluorescence levels, outshining the light up of the particles, make their tracking very difficult. Our first results indicate, that some of these challenges can be mastered algorithmically.

Acknowledgements

We thank Dr. Olga Dolnik for providing image sequences and expert knowledge and Christopher Dörr for helpful discussions.

Bibliography

[1] Dolnik, O., Kolesnikova, L. und Becker, S. 2008. *Filoviruses: Interactions with the host cell. Cellular and Molecular Life Sciences.* 2008, Bd. 65, 5, S. 756-776.
[2] Borst, A. 2007. *Correlation versus gradient type motion detectors: the pros and cons. Philosophical Transactions of the Royal Society B: Biological Sciences.* 2007, Bd. 362, 1479, S. 369-374.
[3] Miura, Kota. *Tracking Movement in Cell Biology.* Bd. 95, S. 267-295.
[4] Yilmaz, Alper, Javed, Omar und Shah, Mubarak. 2006. *Object tracking.* ACM Computing Surveys. 2006, Bd. 38, 4, S. 13-es.